Galaxy Formation in the Lambda-Cold Dark Matter Cosmology

GONZALEZ-GUTIERREZ, JUAN,ESTEBAN

How to cite:

GONZALEZ-GUTIERREZ, JUAN,ESTEBAN (2010) *Galaxy Formation in the Lambda-Cold Dark Matter Cosmology*, Durham theses, Durham University. Available at Durham E-Theses Online: http://etheses.dur.ac.uk/377/

Galaxy Formation in the Lambda-Cold Dark Matter Cosmology

Juan Esteban González Gutiérrez

Abstract

In this thesis I explore the effects of the various physical processes behind galaxy formation and evolution in hierarchical cosmologies by using semi-analytical modelling. I use the Durham semi-analytical model `GALFORM`. I first test the `GALFORM` model predictions using observations from the Sloan Digital Sky Survey (SDSS). I use two different variants of the model, Baugh et al (2005), which assumes a top-heavy initial mass function (IMF) in starbursts and superwind feedback, and Bower et al (2006), which incorporates AGN feedback with a standard IMF. I compare the luminosity function, colours, sizes and morphology distributions of present-day galaxies in the models and with the SDSS. The Bower et al model better reproduces the shape of the luminosity function, the morphology-luminosity relation and the colour bimodality observed in the SDSS data. The Baugh et al model is much more successful at predicting galaxy sizes for late-type galaxies. Both models have problems with the sizes of early-type galaxies, which are predicted to be too large for low luminosities and too small for high luminosities compared to SDSS. I tested the impact on the model predictions of varying the prescriptions for supernova feedback, disk instabilities and galaxy mergers. In the second part of the thesis I explore the connection between two high redshift star-forming galaxy populations and present-day galaxies and their contribution to the star formation history. I built galaxy merger trees and followed the evolution and properties of submillimetre galaxies (SMGs) and Lyman-break galaxies (LBGs) using the Baugh et al (2005) model. The model predicts that the descendants of SMGs ($S_\nu > 5$ mJy) have a median stellar mass of $\sim 10^{11} h^{-1} M_\odot$, and that more than 70% of these descendants are bulge-dominated. More than 50% of present-day galaxies with stellar masses larger than $7 \times 10^{11} h^{-1} M_\odot$ are predicted to be descendants of such SMGs. Somewhat controversially, the stellar mass produced in the submillimetre phase contributes only 0.2% of the total present-day stellar mass, and 2% of the stellar mass of SMG descendants. The descendants of $z = 3$ LBGs are predicted to have a median stellar mass equal to that of the Milky Way ($M = 4 \times 10^{10} h^{-1} M_\odot$), while the descendants of $z = 6$ LBGs are predicted to have a larger median stellar mass ($M = 10^{11} h^{-1} M_\odot$). The model predicts that only one in every 16 and one in every 50

Milky Way mass galaxies have a Lyman-break galaxy progenitor at $z = 3$ and $z = 6$ respectively.

Galaxy Formation in the Lambda-Cold Dark Matter Cosmology

by Juan Esteban González Gutiérrez

A thesis submitted to the University of Durham
in accordance with the regulations for
admittance to the Degree of Doctor of Philosophy.

Department of Physics
University of Durham
2010

Contents

List of Figures

Declaration

The work described in this thesis was undertaken between 2006 and 2009 while the author was a research student under the supervision of Professor Carlos Frenk, Dr. Cedric Lacey & Professor Carlton Baugh in the Department of Physics at the University of Durham. This work has not been submitted for any other degree at the University of Durham or any other university.

Chapter 3 of this thesis has been published in the form of a paper,

- González, J. E., Lacey, C. G., Baugh, C. M., Frenk, C. S., Benson, A. J.,
  "Testing model predictions of the cold dark matter cosmology for the sizes, colours, morphologies and luminosities of galaxies with the SDSS",
  2009, MNRAS, 397, 1254.

Chapters 4 and 5 will be submitted as papers for publications in MNRAS shortly after submission of this thesis.

Acknowledgements

There are several people who have helped me to get to this excitement moment of finishing my PhD. Firstly, I would like to thank my supervisors, Dr. Cedric Lacey, Prof. Carlton Baugh and Prof. Carlos Frenk, who have guided, taught and encouraged me, with an amazing patience in my whole journey in the ICC. The weekly meetings became a moment to learn and enjoy. They have been an inspiration and example for me since the very beginning before starting my PhD, when I had the opportunity to visit the ICC thanks to the ALFA network.

I had the opportunity to share offices with many people who made this experience more enjoyable, Tim Rawle, David Radburn-Smith, John Helly, Mark Swinbank, Kristen Coppin, Owen Parry, Ben Lowing and Stephen Hamer. Outside my office, I have enjoyed entertaining moments and excellent astrophysics discussion with friendly faces, among these Alvaro Orsi, David Murphy, Yanchuan Cai, Andrew Cooper, Nikos Fanidakis and Elise Jennings.

I had the luck of having only minor computational problems, in all of which I had the help of an excellent human being, Lydia Heck. I also had the luck to met Lindsay Borrero, without her advice and friendship this work would have been more difficult.

Above and beyond all, my family have always been my main support in every good and complicated moment in my life. I just thank them for always having the right words to say. Specially thanks to Skype for making easier the communication with people in Chile. We were even able to celebrate together the qualification of Chile to the 2010 World Cup South Africa. Go Chile!

Finally, my beloved Lucy. Her company and support made this experience a joyful adventure.

This thesis was supported by a fellowship funded by the European Commission's Framework Programme 6, through the Marie Curie Early Stage Training project MEST-CT-2005-021074

Chapter 1

Introduction

1.1 Introduction

It is fascinating to look at the sky on a clear night. After enjoying the splendour of the night sky, it is natural to start to think about how the objects we see were made.

The evolution of ideas about the Universe started with simple questions: What are these objects? How far are they from us? Then, after realising that we live in a planet which is part of the Solar System, and that this is part of the hundreds of billions of stars that form the Milky Way, we may ask: How big is the Milky Way? Are there any other galaxies? How far they are from us?

In the past few decades, the discovery of new populations of galaxies seen at redshifts corresponding to when the Universe was very young, prompt us to ask how the Milky Way and the galaxies that we see at the present-day are connected with these early galaxies. How do primordial density fluctuations lead to structures like the Milky Way? What are the physical processes behind galaxy evolution? And finally, how can we test them?

What we have learnt so far from theory and observations allows us to develop models for galaxy formation that yield ever more accurate predictions for a wide range of galaxy properties.

In Section 1.2 of this introductory chapter, we[1] give a brief background to modern astronomy and to the main elements of the Cold Dark Matter (CDM) paradigm for structure formation. In Section 1.3, we summarise the techniques that have been introduced to model the formation and evolution of galaxies. In Section 1.4 we present the general motivation for this work and outline a brief description of the chapters of this thesis.

---

[1] Throughout this thesis I will use the conventional ‘we’ to refer to the first person.

1.2 Modern Astronomy

1.2.1 Historical Background

In the early 1920s, two of the main contributors to modern astronomy, Harlow Shapley and Edwin Hubble, were at Mount Wilson, California at the same time. By 1920, Shapley had set a size for the Milky Way. Using bright stars called Cepheid variables as standardised light sources, he measured the galaxy as being an astonishing 300,000 light-years across.

In 1923, spotting a Cepheid variable star in the Andromeda nebula (the name given at the time to the Andromeda Galaxy), Hubble used Shapley's technique to show that the nebula was nearly a million light-years away, far beyond the bounds of the Milky Way.

In these few years, it was proved conclusively that some known nebulae were much too distant to be part of the Milky Way and were, in fact, entirely separate galaxies outside our own.

In 1929, Hubble announced the discovery of a linear relationship between the distance to galaxies and their recessional velocities obtained from their redshifts (Hubble, 1929). This relationship is exactly what would be expected in a uniformly expanding universe.

1.2.2 The Big Bang

According to current theories of cosmology, the early Universe was extremely hot and dense, and almost entirely homogeneous. However, since the Universe as we know it today is far from uniform on small scales, tiny density fluctuations must have been present. As the Universe expanded, in accordance with the laws of General Relativity, these fluctuations grew through gravitational instability and eventually collapsed to form galaxies and clusters of galaxies.

This theory, known as the Hot Big Bang model, provides the context for modern theories of galaxy formation. In these theories, the mass density of the Universe is dominated by invisible, non-baryonic "dark matter", which collapses to create gravitational potential wells in which gas may collect and condense to form stars and galaxies.

Support for this picture came with the discovery of the cosmic microwave background radiation (CMB) by Penzias and Wilson in 1965. Much of this background radiation lies roughly in the wavelength range from fractions of millimeters to tens of centimeters and it is almost entirely isotropic, suggesting that it may uniformly fill the Universe. Observations made with the Cosmic Microwave Background Explorer (COBE) satellite, launched in 1989, have shown that the CMB spectrum is effectively that of a black body with a temperature of 2.7 K (Mather et al., 1994). COBE mapped the entire sky with a spatial resolution of 7-10 degrees and found only very small fluctuations in temperature, of the order of one part in 10^5 (Bennett et al., 1996).

It is difficult to see how such a radiation field could arise in the Universe as it is today. Instead, the CMB is thought to have originated just after the Big Bang. As the Universe expanded, both the plasma and the radiation filling it grew cooler. When the Universe cooled enough, stable atoms could form. These atoms could no longer absorb the thermal radiation, and the Universe became transparent. From this point onwards, photons were no longer able to interact with the baryons and the radiation was released. The expansion of the Universe has since reduced the temperature of the radiation spectrum, but its black body shape has been preserved. Hence the detection of the CMB is a strong indication that the Universe was once much hotter and denser than it is now, in agreement with the Big Bang theory.

1.2.3 Inflation

Despite the observations described above, which are in support of the idea of a Big Bang, some problems remain. One of these is the horizon problem. The microwave background shows that the temperature of this radiation in completely different directions differs by only one part in 10^5 making the Universe extremely isotropic on large scales. However, in the standard Big Bang theory these photons would have been emitted from regions too widely separated to be in causal contact at the time of recombination. These regions could therefore never have been in thermal equilibrium.

A second problem is the flatness problem. In the standard Big Bang model, the density of the Universe rapidly evolves away from the critical density required to eventually halt the expansion of the Universe. Observations indicate that the current density is of the order of the critical density, which would require extremely fine tuning in the early Universe.

A possible solution for these problems was proposed by Guth (1981). He proposed a period of rapid, exponential expansion very early in the history of the Universe. This solves the horizon problem by expanding initially causally connected regions to sizes greater than the present horizon. During inflation, the density of the Universe is driven towards the critical density, so that a flat universe is expected.

Inflation also conveniently provides a mechanism to generate the primordial density fluctuations which are needed if structure is to form in the Universe. These fluctuations originate from quantum fluctuations of the same scalar field which provides the vacuum energy to drive the rapid expansion.

1.2.4 Dark Matter

With new observations in the 1930s extending to galaxy clusters, it soon became apparent that significant amounts of mass appeared to be missed when counting the luminous objects and considering the dynamics of the cluster galaxies. The first such estimates were made by Zwicky (1933) and Smith (1936). The observed velocity dispersions of galaxies in clusters indicated total cluster masses an order of magnitude greater than the mass of the visible galaxies. Later, X-ray observations revealed the presence of a hot, diffuse intracluster medium contributing a quantity of mass similar to that of the luminous galaxies. However, the majority of the mass in galaxy clusters was still left unaccounted for in these calculations.

In the 1970s, evidence for the existence of dark matter in smaller systems was found when the rotation speed of spiral galaxies were measured to remain constant out to larger radii than would be expected if the visible stars and gas constituted the entire mass of the galaxy (e.g. Faber and Gallagher, 1979). Since nucleosynthesis places a strong constraint on the mean density of baryonic material in the Universe and this is around an order of magnitude lower than the mass density inferred from studies of cluster dynamics and galaxy rotation curves, the majority of the missing dark matter must therefore be non-baryonic.

Non-baryonic dark matter is classified in terms of the typical velocity dispersion of the particles. There are two principle hypotheses about the nature of nonbaryonic dark matter, called hot dark matter (HDM) and cold dark matter (CDM). HDM is composed of particles that have zero or near-zero mass (the neutrinos are a prime example). The Special Theory of Relativity requires that massless particles move at the speed of light and that nearly massless particles move at nearly the speed of light. Thus, such very low mass particles must move at very high velocities and thus form (by the kinetic theory of gases) very hot gases. Fast moving particles cannot clump together to form structures on small scales (galaxies). To explain small scale structure in the Universe it is necessary to invoke a form of cold dark matter. CDM is composed of objects sufficiently massive that they move at sub-relativistic velocities. In models where the mass density is dominated by CDM small scale density perturbations collapse first. Larger objects are then built up by the merging of smaller objects. This is called hierarchical structure formation.

1.2.5 Large Scale Structure Formation

In the early Universe, primordial density perturbations were amplified by gravitational instability. The presence of structure in the local Universe suggests that the primordial perturbations must have existed, and inflation provides a possible mechanism to generate them. The subsequent evolution of these perturbations depends strongly on the nature of the dark matter which contributes the majority of the mass density of the Universe. In Fig.1.1 we show the evolution of the fluctuations of the dark matter, baryonic matter and radiation in a CDM universe. Dark matter plays a key role in structure formation because it feels only the force of gravity. Dark matter begins to collapse well before baryonic matter, which is impeded by radiation pressure. Without dark matter, the epoch of galaxy formation would occur substantially later in the universe than is observed.

As mentioned in previous section, in the CDM picture, low mass objects form first and grow through mergers to form more massive objects. Davis et al. (1985) used N-body techniques to simulate this process, and found that a model with a low density parameter, $\Omega = 0.2$, appeared to best match the observed galaxy distribution if galaxies traced the underlying dark matter distribution. However, they noted that this might not be the only solution, and found that a "biased" model with $\Omega = 1$, in which galaxies were assumed to be associated with peaks in the initial density distribution, was also consistent with observations.

There is a growing weight of evidence in support of the hierarchical paradigm for structure formation (Springel et al., 2006). The principal process responsible for the growth of structure, gravitational instability, has been modelled extensively using large numerical simulations (e.g. Springel et al., 2005, 2008). The cold dark matter model gives an impressive fit to measurements of temperature fluctuations in the cosmic microwave background radiation (Hinshaw et al., 2009). When combined with other data, such as measurements of local large scale structure in the galaxy distribution or the Hubble diagram of type Ia supernovae, there is a dramatic shrinkage in the available range of cosmological parameter space (Percival et al., 2002; Sánchez et al., 2006, 2009; Komatsu et al., 2009).

1.3 Galaxy Formation Theories

In order to test current ideas about galaxy formation against observations, well developed theoretical tools are needed which ideally can follow many complex processes concurrently.

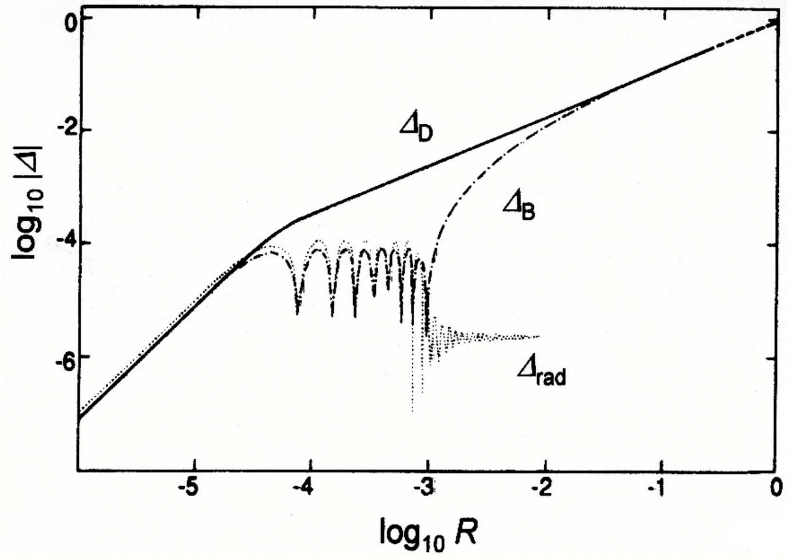

Figure 1.1: Evolution of the fluctuations of the dark matter (Δ_D, continous line), baryonic matter (Δ_B, dash-dotted line) and radiation (Δ_{rad}, dotted line) in a CDM universe as a function of the expansion factor (R). Before entering the horizon, dark matter and baryon-photon fluid perturbations grow as R^2. Between the horizon and decoupling, the dark matter perturbation grows logarithmically and the baryon-photon fluid oscillates rapidly with a decreasing profile. After decoupling, dark matter growth accelerates and the baryonic matter grows rapidly to match the dominant matter perturbation, in matter domination.

The baryonic material which makes up the galaxies we observe in the Universe today behaves quite differently from the dark matter. While on very large scales the distribution of baryons is likely to follow that of the dark matter, on smaller scales hydrodynamic processes such as shock heating and radiative cooling, which the dark matter does not experience, will become important.

1.3.1 First Attempts

Rees and Ostriker (1977), Binney (1977) and Silk (1977) first recognised that radiative cooling would have important consequences for galaxy formation. On small halo scales, and in the absence of any form of heating, gas in a virialised dark matter halo will quickly radiate away its thermal energy. This results in a loss of pressure support, and the gas will collapse to the centre of the halo.

White and Rees (1978) suggested a model in which galaxies formed in this way at the centres of hierarchically assembled dark matter halos. A dark matter halo is a self gravitating structure consisting of dark matter within which the baryonic mass is believed to evolve. It was realised that dissipation would allow the galaxies to become sufficiently concentrated to survive mergers between halos, thereby accounting for the observed groups and clusters of galaxies. By considering the rate at which gas would be able to cool in a dark matter halo and speculating about the effects of feedback from supernovae, White and Rees (1978) were able to obtain a galaxy luminosity function with approximately the correct shape.

Cole (1991) developed a Monte-Carlo model, based on extensions to Press-Schechter theory (Press and Schechter, 1974) developed by Bond et al. (1991) and Bower (1991), to investigate the radiative cooling of gas in dark matter halos. It was found that some form of heating, perhaps by supernovae, was required to prevent the cooling of a large fraction of the gas in small haloes at high redshift. White and Frenk (1991) considered a similar model to Cole (1991) but also included simple models of chemical enrichment and used synthetic stellar spectra to turn the star formation histories of their galaxies into luminosities. White and Frenk (1991) obtained similar results to Cole (1991), and were also able to show that mergers between galaxies were necessary to avoid an overabundance of faint objects. At the same time, Lacey and Silk (1991) adopted a slightly different approach, associating galaxies with peaks in the linear density field and assuming that star formation was induced by tidal interactions. This model also included the effects of radiative cooling and energy injection by supernovae.

An alternative approach to the problem of galaxy formation was also developed around this time. In direct simulations, the gravitational and hydrodynamical equations in the expanding universe are solved explicitly, using one or more of a variety of numerical techniques (e.g. Katz et al. 1992; Frenk et al. 1996, 1999; Katz et al. 1996; Navarro and Steinmetz 1997; Pearce et al. 1999).

1.3.2 Semi-analytic and Hydrodynamics Techniques

Models which use a combination of numerical and analytic methods to calculate the evolution of the galaxy population from a set of initial conditions have come to be known as “semi-analytic” models (see Baugh 2006 for a review).These models choose to treat the baryonic physics in a somewhat more idealised way than is done in gas dynamic simulations. Physical processes are described using rules, some of which contain parameters whose values are set by comparing the model predictions with selected observations or, where possible, with the results of simulations.

More sophisticated semi-analytic models were developed which included additional physical processes. For example, the models of Kauffmann et al. (1993) and Cole et al. (1994) predicted galaxy luminosities using stellar population synthesis techniques and included estimates of the rate of galaxy-galaxy mergers, and the models of Kauffmann (1996) and Cole et al. (2000) included more detailed treatments of metal enrichment.

While early models considered only the formation of galactic disks, the models of Kauffmann et al. (1993) and Baugh et al. (1996) were able to predict a mix of galaxy morphologies by assuming that major mergers disrupted disks and resulted in the formation of an elliptical galaxy. The accretion of additional gas could later lead to the formation of a new disk around the bulge component.

Other developments have included the effects of mergers between satellite galaxies (Somerville and Primack, 1999) and modelling of the effects of dust extinction on galaxy colours and luminosities (Lacey and Cole, 1993; Kauffmann et al., 1999b; Cole et al., 2000). Kauffmann and Haehnelt (2000) used semi-analytic techniques to model quasar activity due to the growth of black holes at the centres of galaxies. Semi-analytic models have also been used to investigate variations in clustering properties with luminosity, morphology and redshift (Kauffmann et al., 1997, 1999a; Baugh et al., 1999), the properties of Lyman break galaxies (Baugh et al., 1998; Governato et al., 1998; Somerville et al., 2001) and the evolution of cluster galaxies (e.g. Kauffmann and Charlot, 1998).

In their most sophisticated form, these models can make predictions for the luminosity, colour, scale-length and morphology of galaxies in a wide range of environments (e.g. Baugh et al., 2005; Bower et al., 2006; Croton et al., 2006; Cattaneo et al., 2006; Monaco et al., 2007; Lagos et al., 2008).

A different approach to galaxy formation modelling is hydrodynamical simulation. The most popular technique is known as Smooth Particle Hydrodynamics, or SPH, which was first described by Lucy (1977) and Gingold and Monaghan (1977).

Gas dynamic simulations typically follow galaxy formation in great detail for an individual dark matter halo (e.g. Governato et al., 2004; Okamoto et al., 2005; Governato et al., 2007) or within some small volume (e.g. Nagamine et al., 2004; Scannapieco et al., 2006; Croft et al., 2008). These simulations have been able to produce galaxies which resemble those observed, but are so computationally intensive that it is difficult to simulate a large enough number of galaxies to derive statistical properties (such as the luminosity function), or to explore the effect of varying physical processes such as star formation and feedback prescriptions.

Hydrodynamical simulations have the advantage of following the evolution of the baryonic and dark matter content of the Universe in complete generality, but have limited spatial and mass resolution. Currently, larger simulations have been developed. The Galaxies-Intergalactic Medium Interaction Calculation (GIMIC; Crain et al. 2009), follows the evolution of five roughly spherical regions of radius $\approx 20h^{-1}$Mpc using gas dynamics within the dark matter, extracted from the Millennium Simulation. The Over-Whelmingly Large Simulations project (OWLS; Schaye et al. 2009) is a collection of roughly 50 Nbody/gasdynamical cosmological simulations of representative volumes (25 to $100h^{-1}$Mpc). The intention of the various OWLS runs is to explore the effects on the simulated galaxy population of varying numerical resolution and star formation, cooling and feedback recipes.

Eventually gas simulations break down in the sense that they have to rely on semi-analytic style recipes to follow some processes (such as feedback). Semi-analytic models are much less computationally intensive, and this allows a more thorough investigation of the effect of varying model parameters. It also means that mass resolution is generally not a problem. However, these models usually involve a number of rather uncertain assumptions, such as spherical symmetry.

1.4 Motivation for this Work

In the last decade, the spectacular progress made in constraining the background cosmology has allowed the focus to shift from reducing the range of the cosmological parameter space to trying to understand the evolution of the baryonic component of the Universe (Baugh, 2006).

Over the same period of time there has been a tremendous increase in the quantity and range of observational data on galaxies at different redshifts. Observations at high redshift have uncovered populations of massive, actively star forming galaxies which were already in place when the Universe was a small fraction of its current age (e.g. Smail et al., 1997; Steidel et al., 1999a; Blain et al., 2002; Giavalisco, 2002). Huge surveys of the local Universe made possible by advances in multifibre spectrographs allow the galaxy distribution to be dissected in numerous ways (e.g. Colless et al., 2003; Adelman-McCarthy et al., 2008). It is now possible to make robust measurements of the distribution of various intrinsic galaxy properties, such as luminosity, colour, morphology and size.

As the range of data the models are compared against increases, the parameter space of the physical processes described in the semi-analytical model is reduced (if no new physical processes are added to the models).

Two key properties of semi-analytical models are their computational speed and modular nature. The impact of different processes on the nature of the galaxy population can rapidly be assessed by running models with different parameter choices. This makes the models ideal tools with which to interpret observational data. Any discrepancy uncovered between the model predictions and observations can help to identify physical ingredients which may either require better modelling or which may be missing altogether from the calculation. One clear example of how observations drive the development of the models is given by the recent efforts to reproduce the location and sharpness of the break in the galaxy luminosity function. With the current best fitting cosmological parameters, galaxy formation models struggled to avoid producing too many bright galaxies (Benson et al., 2003). One solution to this problem was suggested by observations showing the apparent absence of cooling flows at the centres of rich clusters (e.g. Peterson et al. 2003) which motivated the idea of taking into account the energy released by active galactic nuclei (AGN). This acts as a feedback process that heats the gas in massive haloes. The incorporation of this feedback mechanism suppresses the formation of galaxies in massive haloes, such that the right number of bright galaxies can be produced, and, furthermore, these galaxies have red colours to match those observed (Bower et al., 2006; Croton et al., 2006; Lagos et al., 2008).

A powerful feature of semi-analytical models is the ability to connect high redshift galaxies to their present-day descendants. This feature can be used to understand the relation of high redshift galaxy populations to present-day galaxies and the importance of different episodes in the history of galaxies in terms of building up the present-day galaxy mass.

In Chapter 2 we describe the Durham `GALFORM` semi-analytic model, which is extensively used in this thesis. We describe the physical processes included in the model and outline the differences between two versions of this model used in this thesis, the Baugh et al. (2005) model and the Bower et al. (2006) model.

In Chapter 3 we compare the predictions of the `GALFORM` model (using both the Baugh et al. and the Bower et al. versions) for the luminosities, morphologies, colours and scale-lengths of local galaxies, with observations from the Sloan Digital Sky Survey (SDSS). We also investigate the effect of varying some of the physical processes included in the model to try to understand the differences between the two models and with the SDSS data.

In the second part of the thesis we use `GALFORM` to investigate the nature of two high redshift galaxy populations. Galaxies selected by their emission at far infrared wavelengths, submillimetre galaxies (SMGs) or by their rest frame UV flux, Lyman-break galaxies (LBGs), have opened a window on the process of galaxy formation in the early Universe. The usefulness of these samples as indicators of the star formation rate and the connection between them remains controversial. The model is ideally suited to determining precisely what fraction of the cosmic star formation history has been uncovered by either one of these tracers. We explain the significance of a present-day galaxy having either a SMG or a LBG progenitor. SMGs are studied in Chapter 4 and LBGs in Chapter 5.

Finally, in Chapter 6 we present a brief summary of the main conclusions of this thesis and give some possible areas for future research.

Chapter 2

The `GALFORM` *Semi-Analytical Model*

2.1 Introduction

We use the `GALFORM` semi-analytical model to model the formation and evolution of galaxies. The model was introduced by Cole et al. (2000) and developed in a series of subsequent papers (Benson et al., 2003; Baugh et al., 2005; Bower et al., 2006).

2.1.1 Physical processes considered in `GALFORM`

The model tracks the evolution of baryons in the cosmological setting of a cold dark matter universe. The physical processes modelled include (the number in brackets indicates the section where the process is described):

i) the hierarchical assembly of dark matter haloes [Section 2.2],

ii) the shock heating and virialization of gas inside the gravitational potential wells of dark matter haloes [Section 2.2],

iii) the radiative cooling of the gas to form a galactic disk [Section 2.3],

iv) star formation in the cool gas [Section 2.3],

v) the heating and expulsion of cold gas through feedback processes such as stellar winds, AGN and supernovae [Section 2.3],

vi) chemical evolution of gas and stars [Section 2.3],

vii) mergers between galaxies within a common dark halo as the result of dynamical friction [Section 2.4],

viii) the evolution of the stellar populations using population synthesis models [Section 2.5],

ix) the extinction and reprocessing of starlight by dust [Section 2.5].

Here, we summarise the physics included in `GALFORM` and concentrate on the processes which are the most relevant to the thesis. The formalism described in this chapter is based on Cole et al. (2000). We start by describing how the dark matter halos histories are built in Section 2.2. In Section 2.3 we describe how the gas cools to form disk stars. Section 2.4 describes galaxy mergers and how spheroids are built. Finally in Section 2.5 we describe the elements used to compute luminosities of the galaxies.

In this thesis we use two published models run using the `GALFORM` semi-analytical model, the Baugh et al. (2005) model (hereafter Baugh2005) and the Bower et al. (2006) model (hereafter Bower2006). When it is relevant we explain the different approaches taken by the Baugh2005 and by the Bower2006 models. At the end of this Chapter we summarise the difference between these two models.

2.2 Formation of Dark Matter Halos

Since baryonic matter accounts for only a fraction of the total mass (around 17% from WMAP, Hinshaw et al. 2009), the gravity of the dark matter plays an important role in the galaxy formation process. The first element in the `GALFORM` model is to determine the formation histories of dark matter halos and their internal structure (angular momenta and density profiles).

2.2.1 Dark Matter Halo Merger Trees

There are two possible approaches to setting up a merger tree for dark matter halos in the `GALFORM` model. The first one uses a Monte-Carlo technique to generate merger histories for dark matter haloes, which is based on the extended Press-Schechter theory (Bond et al., 1991; Lacey and Cole, 1993). Halo trees in the Baugh2005 model are generated with this technique. The second one is to obtain merger trees directly by following the evolution of dark matter halos in collisionless cosmological N-body simulations. In the Bower2006 model, the merger histories are extracted from the Millennium Simulation (Springel et al. 2005) .

2.2.1.1 Extended Press-Schechter Theory

The Press-Schechter mass function (Press and Schechter, 1974) is used to determine the number of halos to be simulated as a function of mass. Halo trees are then generated starting from the final time and moving back in time using a Monte-Carlo algorithm based on extensions to the Press-Schechter theory proposed by Bond et al. (1991) and Bower (1991). At step back in time, a halo splits into two progenitors, chosen according to the probability of having a progenitor of a given mass. The fraction of mass $f_{12}(M_1, M_2)\mathrm{d}M_1$ in halos of mass M_2 at time t_2 which at the earlier time t_1 was contained in halos in the mass range between M_1 and $M_1 + dM_1$ is given by:

$$\begin{aligned} f_{12}(M_1, M_2)\mathrm{d}M_1 &= \frac{1}{\sqrt{2\pi}} \frac{(\delta_{\mathrm{c}1} - \delta_{\mathrm{c}2})}{(\sigma_1^2 - \sigma_2^2)^{3/2}} \\ &\times \exp\left(-\frac{(\delta_{\mathrm{c}1} - \delta_{\mathrm{c}2})^2}{2(\sigma_1^2 - \sigma_2^2)}\right) \frac{\mathrm{d}\sigma_1^2}{\mathrm{d}M_1}\mathrm{d}M_1. \end{aligned} \tag{2.1}$$

where σ_1 and σ_2 are the rms density fluctuations in spheres of mass M_1 and M_2 and $\delta_{\mathrm{c}1}$ and $\delta_{\mathrm{c}2}$ are the critical linear theory overdensity for collapse at times t_1 and t_2 respectively. Taking the limit of the equation as $t_1 \to t_2$, one obtains the equation:

$$\left.\frac{\mathrm{d}f_{12}}{\mathrm{d}t_1}\right|_{t_1=t_2} \mathrm{d}M_1\mathrm{d}t_1 = \frac{1}{\sqrt{2\pi}} \frac{1}{(\sigma_1^2 - \sigma_2^2)^{3/2}} \frac{\mathrm{d}\delta_{\mathrm{c}1}}{dt_1} \frac{\mathrm{d}\sigma_1^2}{dM_1}\mathrm{d}M_1\mathrm{d}t_1. \tag{2.2}$$

This is the average mass fraction of a halo of mass M_2 at time t_2 which was in halos of mass M_1 at the earlier time t_1. Thus, the mean number of progenitors of mass M_1 that a halo of mass M_2 has when one takes a step dt_1 back in time is given by

$$\frac{\mathrm{d}N}{\mathrm{d}M_1} = \frac{\mathrm{d}f_{12}}{\mathrm{d}t_1} \frac{M_2}{M_1} \mathrm{d}t_1 \qquad (M_1 < M_2). \tag{2.3}$$

This expression gives the average number of progenitors as a function of the fragment mass, M_1. Binary merger trees are built by taking the final halo and dividing its merger history into a series of time steps.

If we impose a mass resolution limit on the merger tree, M_{res}, then the mean number of progenitor halos with masses M_1, in the range $M_{\mathrm{res}} < M_1 < M_2/2$ is

$$P = \int_{M_{\mathrm{res}}}^{M_2/2} \frac{dN}{dM_1} dM_1, \tag{2.4}$$

and the fraction of the original halo mass in progenitors below M_{res} (unresolved halos) is

$$F = \int_0^{M_{\mathrm{res}}} \frac{dN}{dM_1} \frac{M_1}{M_2} dM_1. \tag{2.5}$$

If the timesteps are sufficiently small, so that $P \ll 1$, P may be interpreted as the probability that the halo has two progenitors. To determine whether the halo has one of two progenitors a random number, R, is drawn in the range 0 to 1. If $R > P$ then the main halo has only one progenitor at this time-step. However, the original mass is reduced to $M_2(1-F)$ to account for the loss of masss to progenitors below $M_{\rm res}$. If $P > R$ then a random value of M_1 in the range $M_{\rm res} < M_1 < M_2/2$ is generated consistent with the distribution given by equation 2.3, and two progenitors of masses M_1 and $M_2(1-F)-M_1$ are created. The same procedure is repeated on each fragment at successive time-steps going back in time, and thus a merger tree is built up.

The required inputs that must be specified in order to generate the merger tree are the density fluctuation power spectrum, which gives the function $\sigma(M)$, and the cosmological parameters, Ω_0 and Λ_0, which enter through the dependence of $\delta_c(t)$ on the cosmological model. Additionally, the minimum halo mass to be considered, $M_{\rm res}$, must be chosen.

In this way a binary merger tree can be created with a very fine time resolution. Later, an equivalent merger tree can be set up using a predefined grid of time steps (with coarser time resolution). In such a merger tree, a halo at a given time can have more than two progenitors. The loss of information involved is not significant since, in reality, mergers are not instantaneous events and the predefined grid of time steps are typically much smaller than the dynamical timescales of the merging halos.

The mass function of the dark matter generated by the above Monte Carlo technique is not in perfect agreement with those built from N-body simulations. This disagreement becomes significant when a large time interval is considered back from the start of the tree, which can be important when studying the evolution of high redshift populations. In chapters 4 and 5 we use a modified version of the Monte Carlo merger trees, which better reproduces dark matter halo merger trees extracted from the Millennium Simulation (Parkinson et al., 2008).

2.2.1.2 Trees From N-body simulations

A dark matter N-body simulation follows the evolution of massive discrete particles under the influence of gravity. Each particle represents a mass of dark matter, set by the problem being studied and the computational resources. The equations of motion for each particle depend on solving the gravitational field due to all the other particles, finding the change in particle positions and velocities over some small time step, moving and accelerating the particles and finally calculating the gravitational field in the new distribution to start a new iteration.

The Millennium Simulation follows $N = 2160^3$ particles from redshift z = 127 to the present-day in a cubic region of $500h^{-1}$Mpc on a side. At each of over 60 output times, a catalogue of friends-of-friends (Davis et al. 1985) groups was constructed and the descendants of each group found at the subsequent timestep (see Harker et al. 2006 for a description of the tree construction for the simulation). The resolution in the N-body simulation is determined by the smallest halo that can be reliably identified. The mass resolution of the Millennium trees is $1.72 \times 10^{10} h^{-1} M_{\odot}$, which corresponds to 20 particles and is a factor of three worse than that typically used in the Monte-Carlo trees. Note, although not used here, the Millennium II Simulation is now available with 100 times better mass resolution (in a volume $\approx$ 100 times smaller).

2.2.1.3 After Merger Trees are Built

Galaxies are assumed to form inside dark matter halos, and their subsequent evolution is controlled by the merging histories of the halos containing them.

From the earliest time considered, each halo is assumed to retain its properties (such as its mass, mean density and angular momentum) throughout its lifetime. A halo survives until mergers make it part of a halo with mass greater than $f_{\rm form}$ times its original mass. The properties of this new halo are then computed accordingly (see below). `GALFORM` adopts a value of $f_{\rm form} = 2$.

2.2.2 Halo Properties

A model of the internal structure of the halos is needed in order to calculate the properties of the galaxies contained within it. This must specify the halo density profile required to calculate the sizes and rotation speeds of the galaxies.

2.2.2.1 Halo density Profile

Once the dark matter halo has virialised, each halo in the merger tree is assumed to be spherically symmetric, with a density profile given by the NFW model (Navarro et al., 1995):

$$\rho(r) = \frac{\Delta_{\rm vir}\rho_{\rm crit}}{f(a_{\rm NFW})} \frac{1}{r/r_{\rm vir}\,(r/r_{\rm vir} + a_{\rm NFW})^2} \quad (r \leq r_{\rm vir}), \tag{2.6}$$

with $f(a_{\rm NFW}) = \ln(1 + 1/a_{\rm NFW}) - 1/(1 + a_{\rm NFW})$. The profile is truncated at the virial radius, $r_{\rm vir}$. The virial radius is taken to be the radius at which the mean interior density equals $\Delta_{\rm vir}$ times the critical density, $\rho_{\rm crit} = 3H^2/(8\pi G)$. Here the virial overdensity, $\Delta_{\rm vir}$, is computed using the expressions given by Lacey and Cole (1993) and Eke et al. (1996), for open and flat universes respectively. The free parameter, $a_{\rm NFW}$, which is a scalelength measured in units of the virial radius, is set using the analytic model for the relation between $a_{\rm NFW}$ and halo mass presented by Navarro et al. (1997).

2.2.2.2 Spin Distribution

As a dark matter halo collapses it will experience tidal torques from the gravitational field caused by other structures nearby. These torques will cause the halo to spin (it will gain some angular momentum). The amount of angular momentum gained by a halo in this way is conventionally described by the dimensionless spin parameter $\lambda_{\rm H}$, defined as

$$\lambda_{\rm H} = \frac{J_{\rm H}|E_{\rm H}|^{1/2}}{{\rm G}M_{\rm H}^{5/2}}, \tag{2.7}$$

where $M_{\rm H}$, $J_{\rm H}$ and $E_{\rm H}$ are the total mass, angular momentum and energy of the halo respectively. The spin parameter is assigned at random from a log-normal distribution consistent with the N-body simulation results of Cole and Lacey (1996)

$$P(\lambda_{\rm H})d\lambda_{\rm H} = \frac{1}{\sqrt{2\pi}\sigma_\lambda}\exp\left(-\frac{(\ln\lambda - \ln\lambda_{\rm med})^2}{2\sigma_\lambda^2}\right)\frac{d\lambda_{\rm H}}{\lambda_{\rm H}}, \tag{2.8}$$

with $\lambda_{\rm med} = 0.039$ and $\sigma_\lambda = 0.53$. Each newly formed halo in a halo merger tree is assigned a new spin parameter drawn from the distribution at random, independently of the previous value of the spin parameter.

2.3 Gas Cooling, Star Formation and Disk Formation

In this section we describe the processes of gas cooling which can produce the stars that form the disk of the galaxy, and the reheating of this gas by feedback mechanisms.

2.3.1 Gas Cooling

Although the dark matter is thought to be the gravitationally dominant component of the Universe, it is the baryons (which form the visible parts of galaxies) which are of greatest importance in studies of galaxy formation. Gas which cools inside a dark matter halo is assumed to form a disk at the centre of the halo, supported by the angular momentum acquired through tidal torques during the formation of the halo. The `GALFORM` model differentiates between "cold" gas, which is gas which has been incorporated into galaxies, and "hot" gas which is the diffuse gas which is not part of galaxies, and which is spread throughout the dark matter halo. As the halo collapses, the associated gas will shock and so be heated to approximately the virial temperature of the halo,

$$T_{\rm vir} = \frac{1}{2}\frac{\mu m_{\rm H}}{k_B}V_{\rm H}^2, \tag{2.9}$$

where k_B is the Boltzmann constant, $m_{\rm H}$ is the mass of the hydrogen atom, μ the mean molecular mass and $V_{\rm H}$ is the circular velocity of the halo. These assumptions are motivated by hydrodynamical simulations including those of Navarro et al.(1995), Eke et al. (1998) and Frenk et al. (1999). The gas is assumed to be distributed with a spherically symmetric density profile with a core of radius $r_{\rm core}$:

$$\rho_{\rm gas}(r) \propto 1/(r^2 + r_{\rm core}^2). \tag{2.10}$$

Once the halo has formed the hot gas will begin to cool. The cooling time, defined as the ratio of the thermal energy density to the cooling rate per unit volume, $\rho_{\rm gas}^2\Lambda(T_{\rm gas}, Z_{\rm gas})$, is

$$\tau_{\rm cool}(r) = \frac{3}{2}\frac{\mu m_{\rm H} k T_{\rm gas}}{\rho_{\rm gas}(r)\Lambda(T_{\rm gas}, Z_{\rm gas})}, \tag{2.11}$$

were $\rho_{\rm gas}(r)$ is the density of the gas at radius r, $T_{\rm gas}$ is the temperature and $Z_{\rm gas}$ the metallicity. The amount of gas that has cooled by time t after the halo has formed is estimated by defining a cooling radius, $r_{\rm cool}(t)$, at which $\tau_{\rm cool} = t$.

The time taken for this material to be accreted onto the disk is the free-fall time in the halo. We define a free-fall radius $r_{\rm ff}(t)$ beyond which, at time t, material has not yet had sufficient time to fall onto the central disk. Thus, the mass of gas accreted during a time step is found by calculating $r_{\rm min}(t) = \min[r_{\rm cool}, r_{\rm ff}]$ at the beginning and end of the time step. Any hot gas in the spherical shell between the two values of $r_{\rm min}$ is cooled and added to the disk in that time step.

2.3.2 Disk Scale-Lengths

The size of a galactic disk is determined by the conservation of the angular momentum of the gas cooling from the halo and the application of centrifugal equilibrium. The disk is assumed to have an exponential surface density profile with half-mass radius $r_{\rm disk}$. The half-mass radius of the disk is related to the exponential scale-length, $h_{\rm D}$ by $r_{\rm disk} = 1.68h_{\rm D}$. The scale-length of the disk is dependent on the angular momentum of the gas which cools.

2.3.3 Star Formation in Disks

Star formation converts cold gas into luminous stars. It also affects the physical state of the surrounding gas, since supernovae (SNe) and young stars inject energy and metals back into the interstellar medium (ISM). The removal of material from the disks acts as a feedback process which regulates the star formation rate.

Star formation is assumed to take place in galactic disks at a rate proportional to the mass of cold gas present, $M_{\rm cold}$. The star formation rate is therefore given by:

$$\psi = M_{\rm cold}/\tau_\star \tag{2.12}$$

where $\tau_\star$ is the star formation timescale. τ_* is parametrised differently in Baugh2005 and Bower 2006 models. In both cases, the star formation timescale is allowed to depend upon some power, $\alpha_\star$, of the circular velocity of the disk, $V_{\rm disk}$, and is multiplied by an efficiency factor. In the Baugh2005 model this factor is assumed to be independent of redshift, hence the star formation timescale is given by:

$$\tau_\star = \tau_{\star 0}\,(V_{\rm disk}/200\,{\rm kms}^{-1})^{\alpha_\star}. \tag{2.13}$$

where $\tau_{\star 0}$ is a parameter set to $\tau_{\star 0} = 8$ Gyr. In the case of the Bower2006 model, the efficiency factor scales with the dynamical time of the galaxy $[\tau_{\rm dyn}]$, measured at the half-mass radius of the disk, and therefore the star formation timescale is given by:

$$\tau_\star = \epsilon_\star^{-1}\tau_{\rm dyn}\,(V_{\rm disk}/200\,{\rm kms}^{-1})^{\alpha_\star}., \tag{2.14}$$

where $\epsilon_\star^{-1}$ is a dimensionless parameter set to $\epsilon_\star = 0.0029$. The value of $\alpha_\star$ adopted in the Baugh2005 model is $\alpha_\star = -3$ and in the Bower2006 model is $\alpha_\star = -1.5$.

2.3.4 Feedback

The model assumes that energy input from supernovae causes gas to be ejected from galaxies at a rate:

$$\dot{M}_{\rm eject} = \beta(V_{\rm disk})\psi = [\beta_{\rm reh}(V_{\rm disk}) + \beta_{\rm rsw}(V_{\rm disk})]\psi. \tag{2.15}$$

The gas ejected has two components, the standard supernovae feeback $\beta_{\rm reh}(V_{\rm disk})\psi$ where gas is returned to the galaxy halo and the superwind feeback $\beta_{\rm rsw}(V_{\rm disk})\psi$ where gas is ejected out of the halo.

2.3.4.1 Standard Supernovae Feedback

In the standard supernovae feedback, the gas is reheated and ejected into the galactic halo, from where it is allowed to cool again, at a rate given by $\beta_{\rm reh}(V_{\rm disk})\psi$, with $\beta_{\rm reh}$,

$$\beta_{\rm reh}(V_{\rm disk}) = (V_{\rm hot}/V_{\rm disk})^{\alpha_{\rm hot}}, \tag{2.16}$$

where $V_{\rm disk}$ is the circular velocity at the disk half-mass radius, and $V_{\rm hot}$ and $\alpha_{\rm hot}$ are parameters.

The SN feedback is stronger in the Bower2006 model ($V_{\rm hot} = 485$ km s^{-1} and $\alpha_{\rm hot} = 3.2$) compared with the Baugh2005 model ($V_{\rm hot} = 300$ km s^{-1} and $\alpha_{\rm hot} = 2$).

2.3.4.2 Superwind and AGN Feedback

To regulate the formation of very massive galaxies in the `GALFORM` model, the Baugh2005 and the Bower2006 models have adopted different mechanisms.

In the Baugh2005 model, an additional channel for gas heated by supernovae is invoked, called superwind feedback. In addition to the standard SNe feedback model described, some gas is assumed to be expelled completely from the halo due to heating by supernovae. The amount of mass ejected by superwinds, is parametrized by $\beta_{\rm rsw}(V_{\rm disk})$,

$$\beta_{\rm rsw}(V_{\rm disk}) = f_{\rm sw}{\rm min}[1, (V_{\rm disk}/V_{\rm sw})^{-2}]. \tag{2.17}$$

The Baugh2005 model adopts parameters values $f_{\rm sw} = 2$ and $V_{\rm sw} = 200$ km s^{-1}. The superwind is most effective in removing gas from low circular velocity haloes, with the mass of gas ejected falling with increasing circular velocity. The gas expelled in the superwind is not allowed to recool, even in more massive haloes at later times in the merger history. This has the effect of reducing the cooling rate in massive haloes since these haloes have less than the universal fraction of baryons. Such winds have been observed in massive galaxies, with the inferred mass ejection rates found to be comparable to the star formation rate (e.g. Heckman et al. 1990; Pettini et al. 2001; Wilman et al. 2005).

In the Bower2006 model, an AGN feedback model is implemented which regulates the cooling rate, effectively switching off the supply of cold gas for star formation in quasi-static hot gas haloes. If the cooling time of the gas at the cooling radius, $t_{\rm cool}(r_{\rm cool})$, exceeds a value proportional to the free-fall time at this radius, $t_{\rm ff}(r_{\rm cool})$:

$$t_{\rm cool}(r_{\rm cool}) > \alpha_{\rm cool}t_{\rm ff}(r_{\rm cool}), \tag{2.18}$$

and the AGN power, $\epsilon_{\rm SMBH}L_{\rm Edd}$, is greater than the cooling luminosity, $L_{\rm cool}$,:

$$L_{\rm cool} < \epsilon_{\rm SMBH}L_{\rm Edd}, \tag{2.19}$$

then the cooling flow is quenched by the energy injected into the hot halo by the central AGN. In the AGN power, $L_{\rm Edd}$ is the Eddington luminosity and $\epsilon_{\rm SMBH}$ is a parameter set to $\epsilon_{\rm SMBH} = 0.5$. The Bower2006 model adopts $\alpha_{\rm cool} = 0.58$.

The growth of the black hole is followed using the model described by Malbon et al. (2007).

2.3.5 Chemical Enrichment

The `GALFORM` model follows the star formation process taking into account the metals exchanged between the stars and the hot and cold gas phases. Fig.2.1 depicts the various channels by which mass and metals are transferred between the three phases. The model adopts an instantaneous recycling approximation to model the enrichment of the gas. The change in mass and metallicity of the gas is given by the following equations:

$$\begin{aligned}
\dot{M}_\star &= (1-R)\psi & (2.20)\\
\dot{M}_{\rm hot} &= -\dot{M}_{\rm cool} + \beta\psi & (2.21)\\
\dot{M}_{\rm cold} &= \dot{M}_{\rm cool} - (1-R+\beta)\psi & (2.22)\\
\dot{M}^Z_\star &= (1-R)Z_{\rm cold}\psi & (2.23)\\
\dot{M}^Z_{\rm hot} &= -\dot{M}_{\rm cool}Z_{\rm hot} + (pe + \beta Z_{\rm cold})\psi & (2.24)\\
\dot{M}^Z_{\rm cold} &= \dot{M}_{\rm cool}Z_{\rm hot} & \\
&+ (p(1-e) - (1+\beta-R)Z_{\rm cold})\psi, & (2.25)
\end{aligned}$$

Here, the metallicity of the cold/hot gas is:

$$Z_{\rm cold/hot} = \frac{M^Z_{\rm cold/hot}}{M_{\rm cold/hot}}, \tag{2.26}$$

where M^Z is the mass in metals, R is the recycled fraction (defined as the mass of gas returned to the ISM per unit mass of stars formed), p is the yield (which is the mass of metals returned to the ISM per unit mass of stars formed) and e, the fraction of newly produced metals ejected directly from the stellar disk to the hot gas phase. R and p are set once the initial mass function is chosen. The cooling rate, $\dot{M}_{\rm cool}$, and the hot gas metallicity, $Z_{\rm hot}$, are assumed to be constant over a given timestep of the merger tree.

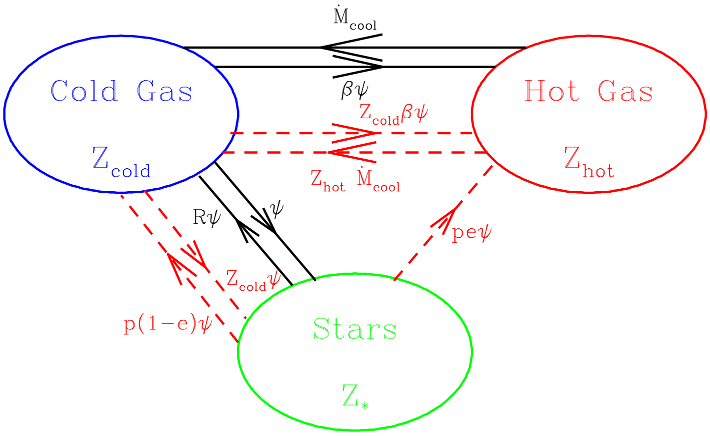

Figure 2.1: Schematic representation of the transfer of mass and metasl between stars, the hot gas and cold gas phase during a single timestep. The solid lines indicate the routes and rates by which mass is transferred between the three reservoirs, while the dashed lines refer only to the exchange of metals. The instantaneous rate of star formation is ψ and the cooling rate is $\dot{M}_{\rm cool}$. The metallicities of the cold gas, stars and hot halo gas are $Z_{\rm cold}$, Z_* and $Z_{\rm hot}$ respectively. The yield of the assumed initial mass function is p and the parameters β and e describe the effect of SN feedback and the direct ejection of SN metals into the hot halo gas. Taken from Cole et al. (2000).

2.3.6 Gas Return After Reheating

The fate of gas reheated by supernovae is different in the two models. In the Baugh2005 model, as discussed above, there are two possible fates for the gas heated by supernovae: ejection from the disk to be reincorporated into the hot halo and ejection from the halo altogether, with no possibility of recooling at a later time. In the case of the first of these channels, the gas is added back into the hot halo when a new halo forms. This happens when the original halo has doubled in mass since its formation time. In the Bower2006 model, this timescale is instead taken to be some multiple of the dynamical time of the halo. Thus, gas can be reheated by supernovae, be added back into hot halo and cool again on a shorter timescale in the Bower2006 model than in the Baugh2005 model.

2.4 Galaxy Mergers and Spheroid Formation

2.4.1 Galaxy Merging

When dark matter halos merge, any galaxies they contain do not immediately merge. Instead, the galaxy in the most massive halo is assumed to become the central galaxy in the new halo while the other galaxies become satellites. Once the satellite galaxies enter the larger halo, it will begin to experience the effects of dynamical friction, whereby its orbital energy is transferred to the dark matter of the larger halo through dynamical friction. Eventually a satellite will merge with the central galaxy if the timescale for the orbit to decay is shorter than the halo lifetime.

Lacey and Cole (1993) estimated the time for an orbit to dacay in an isothermal halo, based on the standard Chandrasekhar (1943) formula for the dynamical friction. Their formula is used to obtain the merger timescale for the satellite galaxy:

$$\tau_{\rm mrg} = f_{\rm df}\,\Theta_{\rm orbit}\,t_{\rm dyn}\,\frac{0.3722}{\ln(\Lambda_{\rm Coulomb})}\frac{M_{\rm H}}{M_{\rm sat}}, \tag{2.27}$$

where $M_{\rm H}$ is the mass of the halo, $M_{\rm sat}$ is the mass of the satellite galaxy (including the mass of the dark matter halo in which it formed), $\tau_{\rm dyn} \equiv \pi r_{\rm vir}/V_{\rm H}$ is the dynamical time of the halo and $f_{\rm df}$ is an adjustable parameter which allows for uncertainties due to the approximations made in this model. The Coulomb logarithm, $\ln(\Lambda_{\rm Coulomb})$ is taken to be equal to $\ln(M_{\rm H}/M_{\rm sat})$. Cole et al. (2000) choose to set $f_{\rm df} = 1$, but note that a slightly higher value may be appropriate if the halo of the satellite galaxy is quickly stripped away. The factor $\Theta_{\rm orbit}$ contains the dependence of the timescale on the orbit of the satellite galaxy

$$\Theta_{\rm orbit} = [J/J_{\rm c}(E)]^{0.78}[r_{\rm c}(E)/r_{\rm vir}]^2, \tag{2.28}$$

where E and J are the initial energy and angular momentum of the orbit, and $r_{\rm c}$ and $J_{\rm c}$ are the radius and angular momentum of a circular orbit with the same energy.

When a new halo forms, each of the satellite galaxies that it contains is assigned a random value of $\Theta_{\rm orbit}$ drawn from a log-normal distribution based on the simulations of Tormen (1997). Satellites then merge with the central galaxy if the merger timescale $\tau_{\rm mrg}$ is smaller than the halo lifetime. If a satellite does not merge during the lifetime of the halo its merger timescale is recalculated when the new halo forms.

2.4.2 Galaxy Merging Process

Spheroids result from galaxy mergers, and in the case of the Bower2006 model also from dynamical instabilities of disks (discussed in Section 2.4.3). The size of the spheroid produced by these events is calculated by considering virial equilibrium and energy conservation. We assume that the projected density profile is well described by a de Vaucouleurs $r^{1/4}$ law (e.g. Binney & Tremaine 1987). The effective radius, $r_{\rm e}$, of the $r^{1/4}$ law, i.e. the radius that contains half the mass in projection, is related to the half-mass radius in three dimensions, $r_{\rm bulge}$, by $r_{\rm bulge} = 1.35 r_{\rm e}$.

Two types of merger are distinguished, major mergers and minor mergers, according to the ratio of the mass of the smaller galaxy to the larger galaxy M_2/M_1. If the ratio is $M_2/M_1 \geq f_{\rm ellip}$, then a major merger is assumed to have taken place. In this case, both stellar disks are transformed into spheroid stars and added to any pre-existing bulge. Any cold gas present takes part in a starburst. If the ratio is $M_2/M_1 \leq f_{\rm ellip}$ then a minor merger is assumed to take place and the stars of the smaller galaxy are added to the bulge of the central galaxy, which keeps its stellar disk. If $f_{\rm ellip} > M_2/M_1 \geq f_{\rm burst}$ and the central galaxy is gas rich, then the minor merger may also be accompanied by a burst. The parameter $f_{\rm ellip} = 0.3$ in both models; $f_{\rm burst} = 0.05$ in Baugh2005 and $f_{\rm burst} = 0.1$ in Bower2006. Disks are considered gas rich if 10% of the total disk mass in stars and cold gas is in the form of cold gas in Bower2006; this threshold is set higher, 75%, in Baugh2005.

2.4.3 Disk Instabilities

The Bower2006 model also allows a spheroid formation as a result of the dynamical instabilities of disks. Strongly self-gravitating disks are considered to be unstable to small perturbations, such as encounters with minor satellites or dark matter substructures. Such events can lead to the formation of a bar and eventually the disk is transformed into a bulge. The onset of instability is governed by the ratio

$$\epsilon = \frac{V_{\rm disk}}{(GM_{\rm disk}/r_{\rm disk})^{1/2}}. \tag{2.29}$$

Disks for which $\epsilon < \epsilon_{\rm disk}$, are considered to be unstable; in Bower2006, the threshold for unstable disks is set at $\epsilon_{\rm disk} = 0.8$. Any cold gas present when the disk becomes unstable is assumed to participate in a starburst. As with starbursts triggered by galaxy mergers, a small fraction of the gas involved in the burst is accreted onto the central black hole.

2.4.4 Spheroid Scale-Lengths

In a merger, the two galaxies are assumed to spiral together until their separation equals the sum of their half-mass radii, which is the moment when they are considered to have merged. We estimate the radius of the merger remnant using energy conservation. Assuming virial equilibrium, the total internal energy $E_{\rm int}$ of each galaxy (both for the merging components and the remnant of the merger) is related to its gravitational self-binding energy $U_{\rm int}$ by $E_{\rm int} = -\frac{1}{2}U_{\rm int}$, and so can be written as

$$E_{\rm int} = -\frac{\bar{c}}{2}\frac{GM^2}{r}, \tag{2.30}$$

where M and r are the mass and half-mass radius respectively and $\bar{c}$ is a form factor which depends on the distribution of mass in the galaxy. For a de Vaucouleurs profile, $\bar{c} = 0.45$, while for an exponential disk, $\bar{c} = 0.49$. For simplicity, in the model we assume $\bar{c} = 0.5$ for all galaxies.

The orbital energy of a pair of galaxies at the moment of merging is given by

$$E_{\rm orbit} = -\frac{f_{\rm orbit}}{2}\frac{GM_1M_2}{r_1 + r_2}, \tag{2.31}$$

where M_1 and M_2 are the masses of the merging galaxies, r_1 and r_2 are their half-mass radii, and $f_{\rm orbit}$ is a parameter which depends on the orbital parameters of the galaxy pair. A fiducial value of $f_{\rm orbit} = 1$ is adopted which corresponds to two point mass galaxies in a circular orbit with separation $r_1 + r_2$. The galaxy masses M_1 and M_2 include the total stellar and cold gas masses and also some part of the dark matter halo. We assume that the mass of dark matter which participates in the galaxy merger in this way is a multiple $f_{\rm dark}$ of the dark halo mass $M_{i,\rm dark}$ within the galaxy half-mass radius. We adopt a fiducial value $f_{\rm dark} = 2$. We thus have:

$$M_i = M_{i,\rm stellar+gas} + f_{\rm dark} M_{i,\rm dark}. \tag{2.32}$$

Later on we will investigate the effect of varying $f_{\rm orbit}$ and the dark matter mass contribution $f_{\rm dark}$ (see Chapter 3).

Assuming that each merging galaxy is in virial equilibrium, then their total energy equals one half of their internal energy. The conservation of energy means that:

$$E_{\rm int,new} = E_{\rm int,1} + E_{\rm int,2} + E_{\rm orbit}, \tag{2.33}$$

and replacing $E_{\rm int}$ with Eq. 2.30 and $E_{\rm orbit}$ with Eq. 2.31 leads to

$$\frac{(M_1 + M_2)^2}{r_{\rm new}} = \frac{M_1^2}{r_1} + \frac{M_2^2}{r_2} + \frac{f_{\rm orbit}}{\bar{c}} \frac{M_1 M_2}{r_1 + r_2}, \tag{2.34}$$

where $r_{\rm new}$ is the half-mass radius of the remnant immediately after the merger. These equations lead to the result that, in a merger of two identical galaxies, the half-mass radius of the new galaxy increases by a factor of 4/3 which agrees reasonably well with the factor of 1.42 found in simulations of equal mass galaxy mergers by Barnes (1992).

In the case of a bulge produced by a disk instability (which is only considered in the Bower2006 model), the considerations that lead to the remnant size are similar to those applied to a bulge produced by mergers, leading to:

$$\begin{aligned} \frac{\bar{c}_{\rm B}(M_{\rm disk} + M_{\rm bulge})^2}{r_{\rm new}} &= \frac{\bar{c}_{\rm B} M_{\rm bulge}^2}{r_{\rm bulge}} + \frac{\bar{c}_{\rm D} M_{\rm disk}^2}{r_{\rm disk}} \\ &+ f_{\rm int} \frac{M_1 M_2}{r_1 + r_2}, \end{aligned} \tag{2.35}$$

where $M_{\rm bulge}$, $r_{\rm bulge}$ and $M_{\rm disk}$, $r_{\rm disk}$ refer to the masses and half-mass radii of the bulge (if any) and disk respectively. As mentioned above, the form factors $\bar{c}_{\rm B} = 0.49$ and $\bar{c}_{\rm D} = 0.45$ for a bulge and disk respectively. The last term in Eq. 2.36 represents the gravitational interaction energy of the disk and bulge, which can be approximated for a range of $r_{\rm bulge}/r_{\rm disk}$ by $f_{\rm int} = 2$.

2.5 Galaxy Luminosities

The properties predicted by the model described so far include the mass and size evolution of each galaxy and its star formation history. To be able to compare the model predictions with observational data, luminosities must be computed as well. This calculation must include the properties of the stars that are formed and the effects of the dust within each galaxy.

2.5.1 Stellar population synthesis

Stellar population synthesis enables us to calculate the observable properties of a composite stellar population, given an assumption about the stellar IMF and the star formation history.

In this technique, the spectral energy distribution (SED) per unit mass of stars, $l_\lambda(t, Z)$, is computed for a single stellar population which all have the same age, t, and metallicity, Z. The SEDs of single stellar populations have been computed by Bruzual A. and Charlot (1993). These single stellar populations can be combined, suitably weighted by the star formation rate, to give the total SED, $L_\lambda(t)$, of a galaxy:

$$L_\lambda(t) = \int_0^t l_\lambda(t - t', Z(t'))\ \psi(t')\ \mathrm{d}t', \tag{2.36}$$

where $Z(t')$ is the metallicity of the stars forming at time t', and $\psi(t')$ is the star formation rate at that time. In the case of a galaxy which formed by merging, the model also sums the contributions to L_λ from the different progenitor galaxies, each with their own star formation and chemical enrichment history.

2.5.2 Initial Mass Function (IMF)

In the fiducial `GALFORM` model of Cole et al. (2000) it is assumed that the IMF is universal in time and space. The standard solar neighbourhood IMF proposed by Kennicutt (1983) is adopted, where the number of stars of a given mass produced is given by $\mathrm{d}N/\mathrm{d}\ln m \propto m^{-x}$, with $x = 0.4$ for $m < 1M_\odot$ and $x = 1.5$ for $m > 1M_\odot$.

The Bower2006 model adopts the Kennicutt (1983) IMF for all modes of star formation. In the Baugh2005 model, emphasis was put on matching the abundance of high redshift dusty starforming galaxies. It was found necessary to adopt a top-heavy IMF for bursts triggered by galaxy mergers. The use of a top-heavy IMF, where the number of stars of a given mass is a power-law with $x = 0$, has two effects in the model: i) it increases the total UV radiation from the young stars formed and ii) it increases the amount of metals and dust (from Type II supernovae) that absorb this radiation. The increased UV luminosity and production of dust for a top-heavy IMF results in a boost of luminosity in the submillimetre range. This results in a better match to the observed number of submillimetre galaxies.

The yield of metals and the fraction of gas recycled per unit mass of stars formed are chosen to be consistent with the form of the IMF. The values are higher for bursts ($p_{\rm burst} = 0.15$, $R_{\rm burst} = 0.91$) than they are for quiescent star formation ($p_{\rm quiescent} = 0.023$, $R_{\rm quiescent} = 0.41$). A larger yield makes a larger contribution from Type II supernovae dust.

A variation of the IMF has been suggested to explain the observed star formation history. Fardal et al. (2007) found a discrepancy in the ratio of the total extragalactic background radiation to the observed stellar density today, if a standard IMF is assumed everywhere. To reconcile these two tests of the star formation history, the authors found that a more top-heavy IMF is needed (increasing the proportion of stars formed with $1.5M_{\odot} < m < 4M_{\odot}$). These authors remark that alternative solutions in which non-stellar sources make large contributions to the background light appear unlikely to resolve the discrepancy. Another suggestion of variation in the IMF comes from the work of van Dokkum (2008). This author compared the luminosity evolution of massive cluster galaxies (at $0.02 \le z \le 0.83$) with their colour evolution. He found that the evolution of the rest-frame $U-V$ colour is not consistent with the previously determined evolution of the rest-frame M/L_B ratio for a standard IMF. He showed that using a different IMF with a flatter slope compared with a standard IMF can help to solve the discrepancy. See also Lacey et al. (2008) for other observational evidence in favour of a top heavy IMF.

2.5.3 Reprocessing of Stellar Radiation by Dust

Absorption and reemission of stellar radiation by dust has a significant effect on the optical luminosities and colour of galaxies. It also has an effect on the far-UV luminosities and in the IR/sub-mm emissions which are particularly important for star forming galaxies at high redshift (In chapters 4 and 5 we study the properties of submillimetre and Lyman-break populations).

Baugh et al. (2005) calculated the reprocessing of stellar radiation by dust using the `GRASIL` code (Silva et al., 1998; Granato et al., 2000), which calculates the distribution of dust grain temperatures within each galaxy based on a radiative transfer calculation and a detailed grain model. However, a drawback of the `GRASIL` code is that it takes several minutes of CPU to run a single galaxy, and so it is very time-consuming to run it on large samples of galaxies. For this thesis, we need to run the `GALFORM` model to follow the evolution (including the sub-mm emission) of large samples of galaxies over many timesteps, in order to be able select submillimetre (Chapter 4) and Lyman-break (Chapter 5) galaxies at any cosmic time, and it was not computationally feasible to do this using the `GRASIL` code directly.

We have therefore developed a simplified model of dust emission which approximately reproduces the results from the `GRASIL` code at long wavelengths. As in `GRASIL`, we assume that the dust is in two phases, molecular clouds and a diffuse medium, with stars forming inside the molecular clouds and then escaping into the diffuse medium on a timescale of a few Myr. We use an approximate radiative transfer calculation (different from the one in `GRASIL` itself) to compute how much stellar radiation is absorbed in each dust component. The most important difference with `GRASIL` is that in our simplified model we assume the dust temperature within each of the dust phases is uniform (so there are only two dust temperatures in a galaxy). In contrast, in `GRASIL` each size and composition of dust grain has its own temperature, which depends on position within the galaxy (which determines the intensity of the stellar radiation field which heats it, via the radiative transfer calculation). Furthermore, `GRASIL` includes the effect of fluctuating grain temperatures for small grains and PAH molecules. Thus in a full `GRASIL` calculation, there is a whole distribution of dust temperatures within each galaxy. A final approximation we make in our simplified dust model is to represent the dust emissivity by a power law in wavelength. These differences between our two-temperature model and `GRASIL` are crucial when calculating the dust emission at mid-IR wavelengths (which is dominated by emission from small grains and PAH molecules, and by warm dust in star-forming clouds), but have much less effect at the wavelengths of interest in this thesis.

2.6 Summary of the differences between Baugh et al. (2005) and Bower et al. (2006) models

In this thesis, we use two published galaxy formation models run using the `GALFORM` semi-analytical model. The Baugh et al. (2005) model invokes a “superwind” channel for supernova feedback, which ejects gas from low and intermediate mass haloes. This model also assumes that stars are produced with a normal solar neighbourhood initial mass function (IMF) in quiescent disks but with a top-heavy IMF during merger-driven starbursts. The Baugh2005 model is able to reproduce the counts and redshift distribution of sub-millimetre selected galaxies, along with the abundance of Lyman-break galaxies and

Lyman-α emitters (Le Delliou et al., 2005, 2006; Orsi et al., 2008). It also reproduces the present-day optical and near- and far-infrared luminosity functions, and the gas fractions and metallicities of present-day galaxies. The Bower et al. (2006) model incorporates AGN feedback, with the energy released by the accretion of mass onto the central supermassive black hole in halos with quasistatic hot gas atmospheres being responsible for stifling the cooling rate (see also Croton et al. 2006). The Bower2006 model gives a good match to the evolution of the K-band luminosity function and the inferred stellar mass function.

The Baugh2005 and Bower2006 models represent alternative models of galaxy formation. The parameters which specify the models were set by the requirement that their predictions should reproduce a subset of the available observations of local galaxies together with certain observations of high redshift galaxies. Different solutions were found due to the use of different physical ingredients, as set out below, and because different emphasis was placed on reproducing particular observations. We refer the reader to the original papers for a full description of each model; the Baugh2005 model is also described in detail in Lacey et al. (2008).

We now summarise the main differences between the two models. We use the Bower2006 model in Chapter 3 and the Baugh2005 model in Chapters 3, 4 and 5.

- *Cosmology.* The Baugh2005 model adopts a ΛCDM cosmology with a present-day matter density parameter, $\Omega_{\rm m}$=0.3, a cosmological constant, Ω_{λ}=0.7, a baryon density, $\Omega_{\rm b} = 0.04$ and a power spectrum normalisation given by $\sigma_8 = 0.93$. The Bower2006 model uses the cosmological model assumed in the Millennium simulation (Springel et al. 2005), where $\Omega_{\rm m}$=0.25, Ω_{λ}=0.75, $\Omega_{\rm b} = 0.045$ and $\sigma_8 = 0.9$, which are in somewhat better agreement with the constraints from the anisotropies in the cosmic microwave background and galaxy clustering on large scales (e.g. Sánchez et al. 2006).

- *Halo merger trees.* The Baugh2005 model uses a Monte-Carlo technique to generate merger histories for dark matter haloes. In the Bower2006 model, the merger histories are extracted from the Millennium simulation. The mass resolution of the simulation trees is $1.72 \times 10^{10} h^{-1} M_{\odot}$, which is a factor of three worse than the standard value used in the Monte-Carlo trees. By comparing the output of models using Monte-Carlo and N-body merger trees, Helly et al. (2003) found very similar predictions for bright galaxies, with differences only becoming apparent below some faint magnitude, the value of which depends on the mass resolution of the N-body trees. The resolution of the Millennium simulation yields a robust prediction for the luminosity function to around three magnitudes fainter than $L_\star$, which is more than adequate for the comparisons presented in chapter 3.

- *Quiescent star formation timescale.* In the Baugh2005 model, the efficiency factor of the star formation timescale is assumed to be independent of redshift, whereas in the case of the Bower2006 model, this factor scales with the dynamical time of the galaxy [$\tau_{\rm dyn}$]. Since the typical dynamical time gets shorter with increasing redshift, the star formation timescale in the Bower2006 model is shorter at high redshift than it would be in the equivalent disk in the Baugh2005 model. This has implications for the amount of star formation in merger-triggered starbursts (or following a disk becoming dynamically unstable in the Bower2006 model - see later). In the Bower2006 model, disks at high redshift tend to be gas poor, with the gas being turned into stars on a short timescale after cooling, whereas in the Baugh2005 model, high redshift disks are gas rich.

- *Initial mass function (IMF) for star formation.* The Bower2006 model uses the Kennicutt (1983) IMF. The Baugh2005 model also adopts this IMF in quiescent star formation in galactic disks. However, in starbursts triggered by galaxy mergers, a top-heavy IMF is assumed.

- *Supernova (SN) feedback.* The SN feedback is stronger in the Bower2006 model. The parameters from the Eq. 2.15 are $V_{\rm hot} = 485$ km s^{-1} and $\alpha_{\rm hot} = 3.2$ in the Bower2006 model and $V_{\rm hot} = 300$ km s^{-1} and $\alpha_{\rm hot} = 2$ in the Baugh2005 model.

- *AGN vs superwind feedback.* Perhaps the most significant difference between models is the manner in which the formation of very massive galaxies is suppressed. In the Baugh2005 model, a superwind feedback is used, where some gas is assumed to be expelled completely from the halo due to heating by supernovae. In the Bower2006 model an AGN feedback model is implemented which regulates the cooling rate, effectively switching off the supply of cold gas for star formation in quasi-static hot gas haloes.

- *Disk instabilities.* In the Baugh2005 model the only process that leads to the formation of bulge stars is a galaxy merger. In the Bower2006 model, a bulge can also be produced by disk instabilities. This is an important channel for the growth of low and intermediate mass black holes in this model.

- *Treatment of reheated cold gas.* In the Bower2006 model, there is a gradual reincorporation of the gas reheated by supernovae, on a shorter timescale compared to the Baugh2005 model.

Chapter 3

Testing `GALFORM` *Predictions for the Sizes, Colours, Morphologies and Luminosities of Galaxies Using the SDSS*

3.1 Introduction

In recent years, large surveys of the local Universe made possible by advances in multifibre spectrographs have allowed the galaxy distribution to be dissected in numerous ways (e.g. Colless et al., 2003; Adelman-McCarthy et al., 2008). The huge size and uniformity of the Sloan Digital Sky Survey (SDSS) makes possible an exacting test of current models of galaxy formation. Robust measurements of the distribution of various intrinsic galaxy properties, such as luminosity, colour, morphology and size can be done using this survey (e.g. Blanton et al. 2003; Shen et al. 2003; Baldry et al. 2004; Blanton et al. 2005a). The trends uncovered in this local survey are influenced by a wide range of physical effects, such as star formation, supernova and AGN feedback, the cooling of gas and galaxy mergers, and hence provide a strict test of galaxy formation models.

In this chapter we test the `GALFORM` model in the versions of Baugh et al. (2005) and Bower et al. (2006) against statistics measured from the SDSS. The `GALFORM` model is described in Chapter 2, and a summary of the differences between Baugh et al. and Bower et al. can be found in Section 2.6.

In Section 3.2 we describe how some additional galaxy properties are computed from the `GALFORM` model output; these properties are needed to accurately compare the model predictions directly with observations of SDSS galaxies. Section 3.3 contains the comparisons between model predictions and SDSS data for the luminosity function, the distribution of morphological types, the colour distribution and the size distribution. In Section 3.4 we show the impact on the predictions of changing the strengths of various processes in the model. In Section 3.5 we present our conclusions. In the Appendix B of this thesis we discuss how certain photometric properties of galaxies have changed between SDSS data releases and compare different indicators of galaxy morphological type. Finally, we note that magnitudes are quoted on the AB system assuming a Hubble parameter of $h = H_0/100$ km s^{-1} Mpc^{-1}; the cosmological parameters adopted depend slightly on the choice of semi-analytic model as explained in Section 2.6.

3.2 Derived Galaxy Properties

In this section we describe how standard `GALFORM` outputs, such as disk and bulge total luminosities and half-mass radii are transformed into quantities which are measured for SDSS galaxies. This allows a direct comparison between the model predictions and the observations. We outline the calculation of Petrosian magnitudes (Section 3.2.1), the concentration index (Morgan 1958; Section 3.2.2) and the Sérsic index (Sérsic 1968; Section 3.2.3). The latter two quantities are used as proxies for morphological type in analyses of SDSS data. We also illustrate how the Petrosian magnitude, concentration index and Sérsic index depend on the bulge-to-total luminosity ratio and on the ratio of the disk and bulge radii.

3.2.1 Petrosian Magnitude

As a measure of galaxy flux, the SDSS team uses a modified definition of the Petrosian (1976) magnitude. The Petrosian radius $r_{\rm Pet}$ is defined as the radius for which the following condition holds:

$$\frac{\int_{0.8r_{\rm Pet}}^{1.25r_{\rm Pet}} {\rm d}r 2\pi r I(r)/[\pi(1.25^2 - 0.8^2)r_{\rm Pet}^2]}{\int_0^{r_{\rm Pet}} {\rm d}r 2\pi r I(r)/[\pi r_{\rm Pet}^2]} = 0.2, \tag{3.1}$$

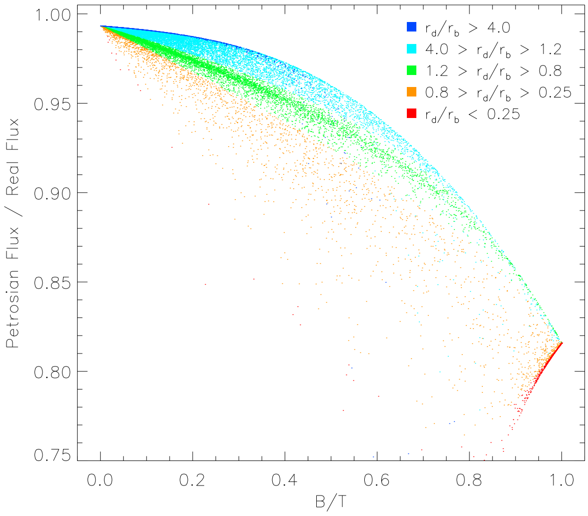

Figure 3.1: The ratio of Petrosian flux to total flux for a sample of **GALFORM** galaxies with the same selection as the SDSS, plotted as a function of the bulge to total luminosity ratio (B/T), measured in the $r-$band taking into account dust extinction. Points are colour-coded according to the ratio of disk to bulge scale-lengths, as indicated by the legend.

where $I(r)$ is the surface brightness profile. Defined in this way, $r_{\rm Pet}$ is the radius where the local surface brightness averaged within a circular annulus centred on the Petrosian radius is 0.2 times the mean surface brightness interior to that radius. The Petrosian flux defined by the SDSS is then obtained within a circular aperture of radius $2r_{\rm Pet}$. In the SDSS, the aperture used in all five bands is set by the profile of the galaxy in the r-band. $I(r)$ is the azimuthally-averaged surface brightness measured in a series of annuli. In the case of **GALFORM** model galaxies, we calculate the disk and bulge sizes, and adopt an exponential profile for the disk with $I(r) \propto \exp(-1.68(r/r_{\rm D}))$, where $r_{\rm D}$ is the disk half-light radius, and a de Vaucouleurs profile for the bulge (assumed to be spherical), with $I(r) \propto \exp(-7.67(r/r_{\rm B})^{1/4})$, where $r_{\rm B}$ is the bulge half-light radius in projection (see Cole et al. 2000). The total surface brightness profile for a galaxy is given by the sum of the disk and bulge profiles. The disk and bulge magnitudes include dust extinction. A random inclination angle is assigned to the galactic disk for calculating the dust extinction. The Petrosian flux within a circular aperture of $2r_{\rm Pet}$ recovers a fraction of the total light of the galaxy which depends on its luminosity profile and hence its morphology. For a pure disk with an exponential profile, the Petrosian flux recovers in

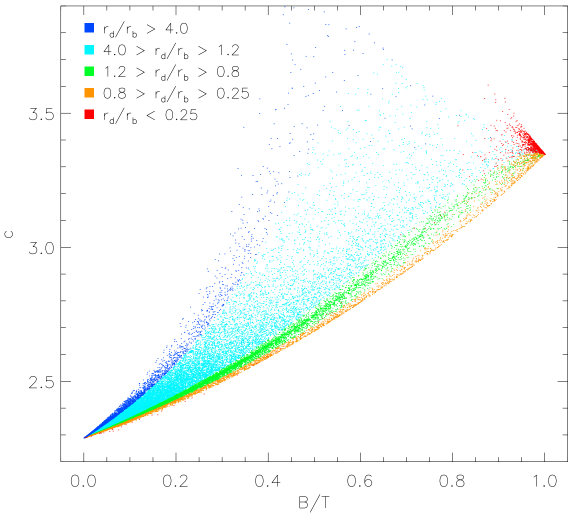

Figure 3.2: The concentration index, c, plotted as a function of the bulge-to-total luminosity (B/T) in the $r-$band for the Baugh2005 model galaxies. The ratio of disk to bulge scale-lengths is indicated by the colour of the symbol as shown by the key.

excess of 99% of the total flux. On the other hand, for a pure bulge with a de Vaucouleurs profile, the percentage of the total light recovered by the Petrosian magnitude is closer to 80%. Fig. 3.1 shows the ratio of Petrosian flux to total flux for model galaxies as a function the bulge-to-total luminosity ratio in the r-band. The limiting cases described above are apparent in the plot, which also shows the fraction of light recovered by the Petrosian definition for composite disk plus bulge systems, and for different ratios of the disk and bulge scale-lengths. Only model galaxies brighter than $M_r - 5\log h = -16$ are included in this plot.

3.2.2 Concentration Index

The concentration index can be straightforwardly derived once the Petrosian flux and radius have been calculated. The concentration index is defined as $c = R_{90}/R_{50}$, where R_{90} and R_{50} correspond to the radii enclosing 90% and 50% of the Petrosian flux respectively in the r-band. Hence, the luminosity is dominated by the bulge for high concentration galaxies and is dominated by the disk for low concentration galaxies. In Fig. 3.2 we plot the bulge-to-total luminosity versus the concentration index for model galaxies in the r-band brighter than $M_r - 5\log h = -16$. We can see that pure disks have $c = 2.3$, pure bulges have $c = 3.3$, and intermediate values of concentration index correspond to

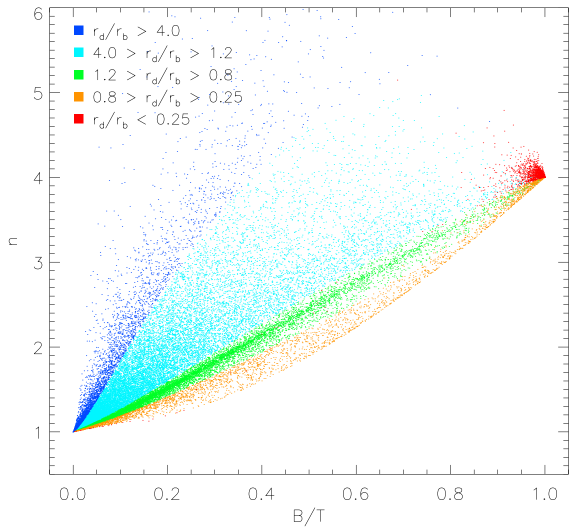

Figure 3.3: The Sérsic index n plotted against the bulge-to-total luminosity ratio (B/T) for the Baugh2005 model galaxies. The ratio of disk to bulge scale-lengths is indicated by the colour of the symbol, as shown by the key.

galaxies with different combinations of $r_{\rm disk}/r_{\rm bulge}$ and B/T. Most galaxies lie in a narrow locus of B/T versus c, but different combinations of disk and bulge scale-lengths and B/T produce the scatter shown. Observationally, the Petrosian concentration index is affected by seeing (Blanton et al., 2003). The same galaxy can show different concentrations under different seeing conditions.

3.2.3 Sérsic Index

The Sérsic index describes the shape of a fit made to the surface brightness profile of a galaxy without prior knowledge of the scale-lengths of the disk and bulge components. The radial dependence of the profile is given by (Sérsic 1968):

$$I(r) = I_0 \exp[-(r/r_0)^{1/n}]. \tag{3.2}$$

Here I_0 is the central surface brightness, r_0 is the Sérsic scale radius and n is the Sérsic index. The Sérsic index has been shown to correlate with morphological type (e.g. Trujillo, Graham & Caon 2001). We can see that if $n = 1$ we recover an exponential profile (used for pure disk galaxies) and if $n = 4$ we recover a de Vaucouleurs profile, used to describe pure bulge galaxies. The Sérsic index has been calculated in the New York University

Value Added Catalogue (NYU-VAGC; Blanton et al. 2005b). Here, we do not attempt to reproduce exactly the procedure that Blanton et al. used to obtain the parameters in Eq. 3.2 (which takes into account seeing and pixelization). Since we know the full surface brightness profile of the model galaxies out to any radius, we want the Sérsic profile that best reproduces the composite disk plus bulge profile. In order to determine the parameters of the Sérsic profile, I_0, r_0 and n, we minimize a χ^2 function which depends on the difference between the Sérsic profile and the sum of the disk and bulge surface brightness profiles, given the scale-lengths and luminosity ratio of these components:

$$\chi^2 = \sum_i [\log I_{\rm disk+bulge}(r_i) - \log I_{\rm Sérsic}(r_i, r_0, n)]^2 W_i. \tag{3.3}$$

The total luminosity of the fitted Sérsic profile is constrained to be equal to that in the true disk + bulge profile. Here r_i is a series of rings between $r = 0$ to $r = R_{90,D+B}$, the radius enclosing the 90% of the disk plus bulge profile flux, and the weight W_i is given by the luminosity in the ring containing r_i. Since the steepness of the Sérsic profile is more evident at the centre of the galaxy, we assign half of the bins to the region within the bulge size $r_{\rm bulge}$ (so as long as $r_{\rm bulge} < R_{90,D+B}$). As a test to check the consistency of changing from a disk+bulge profile to the Sérsic profile, we have compared R_{50} (the radius enclosing 50% of the total luminosity) obtained from the two descriptions of the surface density profile and find very similar results.

If it is assumed that the distribution of light in real galaxies is accurately described by the Sérsic profile, then quantities derived from fitting a Sérsic profile have some advantages over the corresponding Petrosian quantities. (i) The total flux integrated over the fitted Sérsic profile would equal the true total flux, unlike the Petrosian flux, which underestimates the true total value, especially for bulge-dominated galaxies, as shown in Fig. 3.1. (ii) The effects of seeing can be included in the Sérsic profile fitting, so that quantities obtained from the fit (total flux, scale size r_0 and Sérsic index n) are in principle corrected for seeing effects, unlike the corresponding Petrosian quantities. However, since the Petrosian quantities are the standard ones used by the SDSS community, in the rest of this chapter we work with Petrosian magnitude and radius, unless otherwise stated.

Fig. 3.3 shows the correlation between Sérsic index and the bulge-to-total luminosity ratio in the r-band. There is a considerable scatter between these two proxies or indicators of morphology, driven by the ratio of the scale-lengths of the disk and bulge components. For example, galaxies with a Sérsic index of $n = 4$, usually interpreted as a pure bulge light profile, can have essentially any value of bulge-to-luminosity ratio from $B/T = 0.1$–1. A key feature of this plot is the distribution of disk to bulge size ratios generated by `GALFORM`. It is possible to populate other parts of the n - B/T plane in the cases of extremely large or small values of the ratio of disk to bulge radii. Without the guidance of a physical model, if a grid of $r_{\mathrm{d}}/r_{\mathrm{b}}$ was used instead, the distribution of points would be even broader than shown in Fig. 3.3. Note that only model galaxies brighter than $M_r - 5\log h = -16$ are included in this plot. A similar scatter is seen between these two quantities for real galaxies, as shown by Fig. B.4 in the Appendix.

3.3 Results

The primary observational data set we compare the model predictions against is the New York University Value Added Catalogue (NYU-VAGC), which gives additional properties to those found in the SDSS database for a subset of DR4 galaxies (Blanton et al., 2005b). The NYU catalogue covers an area of 4783 deg^2 and contains 49968 galaxies with redshifts. The sample is complete to $r_{\mathrm{Pet}} = 17.77$ over the redshift interval $0.0033 < z < 0.05$, and has a median redshift of $z = 0.036$. The relatively low median redshift compared with the full spectroscopic sample is designed to provide a sample of large galaxy images, suitable for measurements of galaxy morphology. Examples of the extra properties listed for galaxies, beyond the information available in the SDSS database, include the rest-frame (AB) absolute magnitude, the Sérsic index and the value of V_{max} (i.e. the maximum volume within which a galaxy could have been observed whilst satisfying the sample selection; this quantity is used to weight each galaxy in statistical analyses). We run `GALFORM` with an output redshift of $z = 0.036$ to match the median of the NYU-VAGC and derive properties from the output which can be compared directly against the observations, as described in Section 3.2. In Section 3.3.1, we compare the model and observed luminosity functions, in Section 3.3.2 we show the distribution of morphological types versus luminosity, in Sectoin 3.3.3 we examine the colour distributions and explore this further as a function of morphology in Section 3.3.4. Finally in Section 3.4 we test the size predictions against observations and assess the sensitivity of the model output to the strength of various processes.

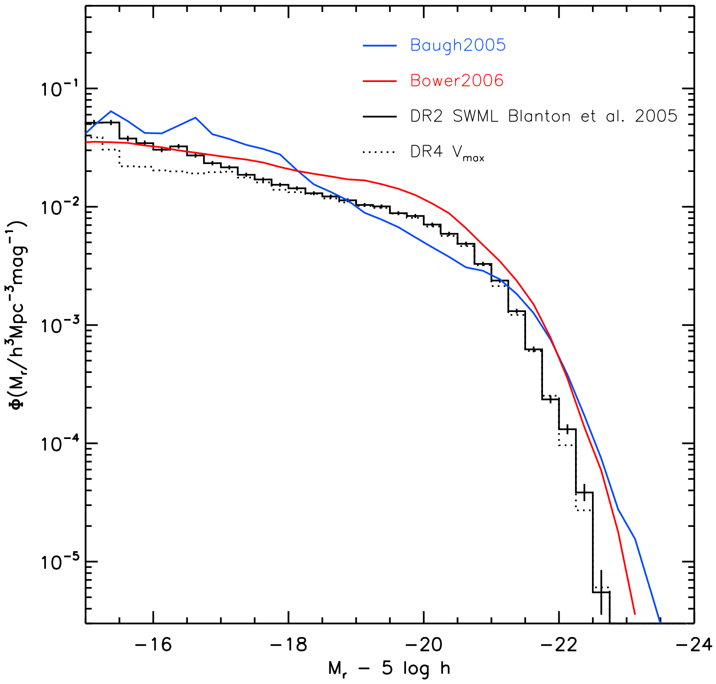

Figure 3.4: The $r-$band luminosity function predicted by the Bower2006 (red) and Baugh2005 (blue) models. For comparison, we also plot the SDSS luminosity function estimated using the SWML estimator by Blanton et al (2005) from DR2 (solid histogram) and our result using the $1/V_{\rm max}$ estimator from DR4 (dotted histogram).

3.3.1 Luminosity Function: All Galaxies and by Colour

The local luminosity function plays a key role in constraining the parameters which specify a galaxy formation model. The comparison between the predicted and observed luminosity functions is hence a fundamental test of any model. The original papers describing the Baugh2005 and Bower2006 models showed the comparison of the model predictions with the observed local luminosity function in the optical and near-infrared. However a comparison with SDSS data was not made in those papers. Fig. 3.4 shows the luminosity function in the Petrosian r-band predicted by the Baugh2005 and Bower2006 models, compared with our estimate of the luminosity function from SDSS DR4 made using the values of $V_{\rm max}$ from the NYU-VAGC catalogue. We also overplot the luminosity function estimated from the SDSS DR2 by Blanton et al. (2005a) using the stepwise maximum likelihood (SWML) method. The SWML and $1/V_{\rm max}$ estimates are in very good agreement, particularly for magnitudes brighter than $M_r - 5\log h = -17$. At fainter magnitudes,

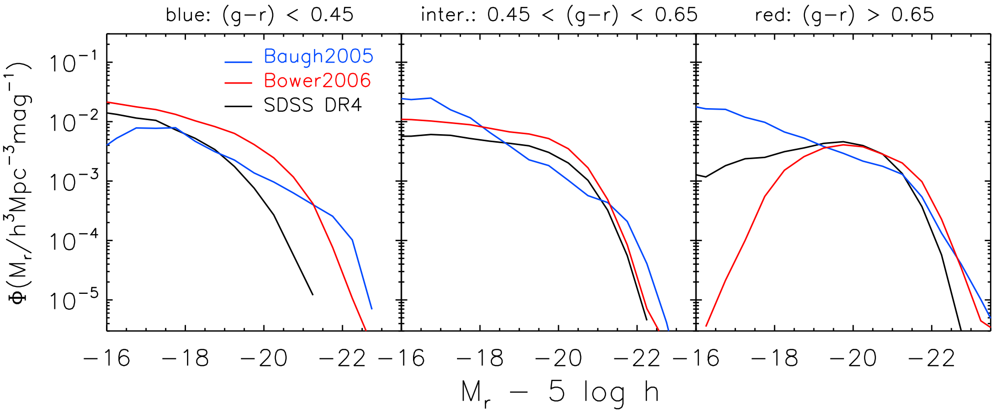

Figure 3.5: The colour-dependent luminosity function, for three populations of galaxies defined by the $g-r$ colour as shown by the label on top of each panel. The black lines show the luminosity function estimated from DR4 and the red (Bower2006) and blue (Baugh2005) lines show the model predictions (see the legend in the left panel).

the $1/V_{\max}$ estimator could be affected by very local large scale structure (Blanton et al., 2005a).

Both models overpredict the abundance of bright galaxies. The Bower2006 model produces a somewhat better match to the shape of the SDSS luminosity function. This offset in the $r-$band luminosity function has also been noted by Cai et al. (2009), who made the model galaxies in the Bower2006 model fainter by 0.15 magnitudes before using this model to make mock galaxy surveys. It is worth noting that the Bower2006 model gives an excellent match to both the b_{J}-band luminosity function estimated from the 2dF galaxy redshift survey (Norberg et al. 2002) and to the K-band luminosity function (e.g. Cole et al. 2001; Kochanek et al. 2001) without the need to shift the model magnitudes by hand.

We can study the impact on the luminosity function of different physical processes in more detail by using colour to separate galaxies into different samples. For the SDSS data we can compute the luminosity function of colour sub-samples using the $1/V_{\max}$ estimator, bearing in mind that fainter than $M_r - 5\log h = -17$ this method gives an unreliable estimate of the luminosity function due to local large-scale structure. We use the rest-frame Petrosian $g-r$ colour to split galaxies into blue ($g-r < 0.45$), red ($g-r > 0.65$) and intermediate ($0.45 < g-r < 0.65$) colour samples. In Fig. 3.5, we can see that both models reproduce the intermediate colour population fairly well (middle panel). The Bower2006 model in particular matches the shape of the observed luminosity function closely, albeit with a shift to brighter magnitudes, similar to that seen in the case of the overall luminosity function in Fig. 3.4. The models fare worst for blue galaxies, with both models overpredicting the number of bright blue galaxies. This suggests that star formation is not quenched effectively enough in massive haloes or that the timescale for gas consumption in star formation is too long. For the case of red galaxies, the models do best brightwards of L_*, but get the number of faint red galaxies wrong, with the Baugh2005 model giving too many faint red galaxies and Bower2006 too few.

3.3.2 The Distribution of Morphological Types

In this section we examine the mix of morphological types as a function of luminosity, using different proxies for galaxy morphology.

We first look at the mix of galaxies using the Sérsic index. Using a Sérsic index value of $n = 2.5$ (which is half-way between $n = 1$ and $n = 4$), we separate galaxies into two broad morphological classes, disk-dominated galaxies (late type galaxies) with $n < 2.5$ and bulge-dominated galaxies (early type galaxies) with $n > 2.5$. Fig. 3.6 shows the fraction of galaxies in each morphological type, as a function of Petrosian magnitude, M_r, for SDSS galaxies and the `GALFORM` model (Baugh2005 in the left panel and Bower2006 in the right panel). The trend found for SDSS galaxies is that the disk-dominated population is the more common at faint magnitudes, whereas bulge-dominated objects are in the majority brighter than L_*. Fig. 3.6 shows that both models follow the same general trend, but with the changeover from one population to the other occuring brighter than L_* in the Baugh2005 model, whereas the Bower2006 model looks more similar to the observations.

Another way to morphologically classify galaxies using the profile shape is to use the Petrosian concentration index c. In Fig. 3.7, we show the fraction of early and late type galaxies as a function of luminosity based on this, where we classify galaxies (following Shen et al. 2003) with $c < 2.86$ as late type and $c > 2.86$ as early type. The resulting plots look very similar to those based on Sérsic index in Fig. 3.6, though there are differences in detail, particularly at the bright end. The agreement between the models and the SDSS data is generally better using the concentration as the classifier, particularly for the Bower2006 model.

As a third approach to determining galaxy type, we consider the bulge to total luminosity ratio, B/T measured in the $r-$band. Benson et al. (2007) fitted disk and bulge

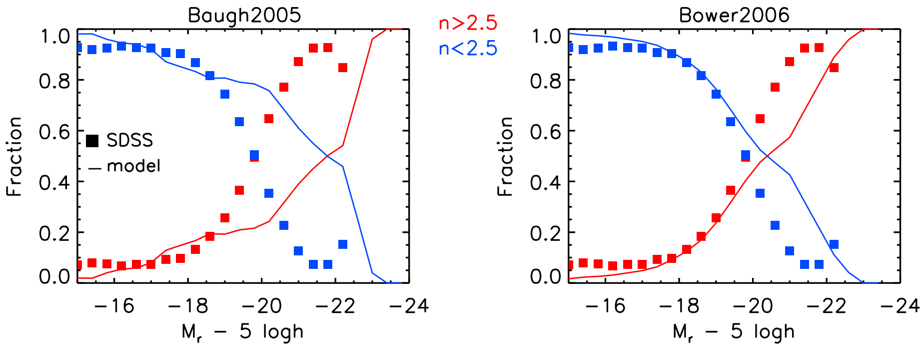

Figure 3.6: The fraction of different morphological types as a function of magnitude M_r for SDSS data (squares) and `GALFORM` (solid lines). The fraction of disk-dominated galaxies (as defined by a value of the Sérsic index $n < 2.5$) is shown in blue and bulge-dominated galaxies (i.e. those with $n > 2.5$) are plotted in red. The left panel shows the Baugh2005 model and the right panel the Bower2006 model.

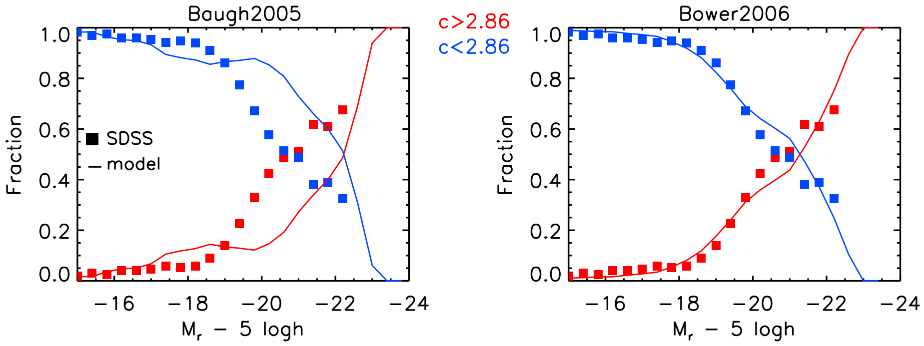

Figure 3.7: The fraction of different morphological types as a function of magnitude M_r for SDSS data (squares) and `GALFORM` (solid lines), using the Petrosian concentration index c to define type. The fraction of disk-dominated galaxies (as defined by $c < 2.86$) is shown in blue and bulge-dominated galaxies (i.e. those with $c > 2.86$) are plotted in red. The left panel shows the Baugh2005 model and the right panel the Bower2006 model.

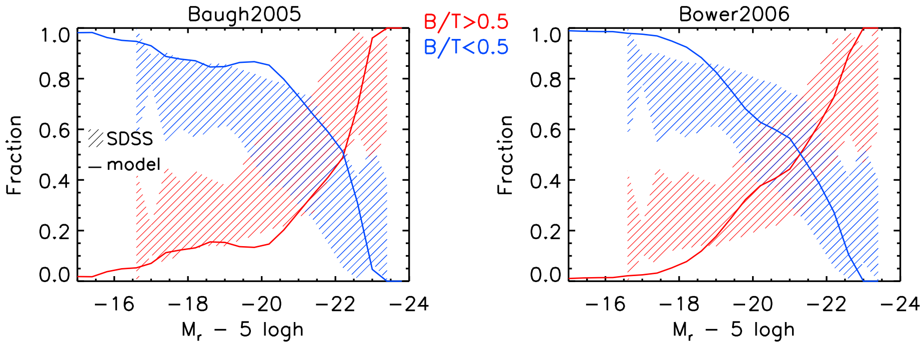

Figure 3.8: The fraction of different morphological types as a function of magnitude M_r using the bulge-to-total luminosity ratio in the $r-$band to define type. Disk-dominated galaxies ($B/T < 0.5$) are shown in blue and bulge-dominated ($B/T > 0.5$) are plotted in red. The solid curves show the model predictions, according to the label above each panel. The shaded region shows an observational estimate made from SDSS data by Benson et al. (2007). The extent of the shading shows by how much the fraction changes when a correction is applied to the observational estimates (see Benson et al. for details).

components to images of 8839 bright galaxies selected from the SDSS EDR. In fitting the disk and bulge components of each galaxy, they used the bulge ellipticity and disk inclination angle, i, as free parameters. The resulting distribution of $\cos(i)$ showed an excess of face-on galaxies. This is due in part to the algorithm mistaking part of the bulge as a disk. Benson et al. attempted to correct for the uneven distribution of inclination angles in the following way. Galaxies with $\cos(i) < 0.5$ are assumed to have been correctly fitted. Since a uniform distribution in $\cos(i)$ is expected, for each galaxy with $\cos(i) < 0.5$, a galaxy with a similar bulge and face-on, projected disk magnitude but with $\cos(i) > 0.5$ is also selected. The galaxies with $\cos(i) > 0.5$ which are left without a match are assumed to correspond to cases where the disk component has been used to fit some feature in the bulge. Benson et al. assigned to these galaxies a value of B/T=1. The correction has a considerable impact on the fraction of bulge- and disk-dominated galaxies, as shown by the extent of the shaded region in Fig. 3.8.

The observational estimates of the mix of morphological types presented in Figs. 3.6, 3.7 and 3.8 are qualitatively the same, but show that the transition from disk-dominated to bulge-dominated depends on the choice of property used to define morphology. We note that the model predictions are very similar when we set the division at $c = 2.86$ or at $B/T = 0.5$. The model predictions made using the Sérsic index, concentration and bulge-to-total luminosity ratio appear to be closer to each other than the corresponding observational measurements. This comparison gives some indication of the observational uncertainty in measuring fractions of different morphological types using the Sérsic index, concentration and bulge-to-total luminosity ratio.

3.3.3 Colour Distribution

An important feature uncovered in the SDSS data is a bimodality in the galaxy colour-magnitude relation (e.g. Strateva et al. 2001; Baldry et al. 2004). In Fig. 3.9 we plot the distribution of rest-frame Petrosian $(u - r)$ colour in selected bins of magnitude M_r for models and SDSS data. The SDSS data shows a dominant red population at bright magnitudes, with a blue population that becomes more important at fainter magnitudes. Although we see blue and red populations in the Baugh2005 model predictions for intermediate magnitudes, the red population always dominates, even at the faintest magnitudes. The Bower2006 model, on the other hand displays a clear bimodality, with the red population dominating at bright magnitudes, comparable red and blue populations at intermediate magnitudes and a slightly more dominant blue population at faint magnitudes. The Bower2006 model shows the same behaviour as the SDSS data at bright magnitudes. At faint magnitudes, the Bower2006 model still shows a red population which is not apparent in the data. Font et al. (2008) argued that these faint red galaxies are predominantly satellite galaxies, which in the Bower2006 model have exhausted their cold gas reservoirs. In the Font et al. model, which is a modified version of the Bower2006 model, the stripping of hot gas from satellites is incomplete, and so gas may still cool onto the satellite, fuelling further star formation and causing these galaxies to have bluer colours on average.

Since the SDSS photometry covers five bands (u, g, r, i and z), we can investigate the bimodality further using different colours. In Fig. 3.10 we plot the abundance of galaxies in the colour magnitude plane, for $(u - g), (g - r), (r - i)$ and $(i - z)$ Petrosian colours against magnitude M_r. The top row of panels shows the distributions for the NYU-VAGC SDSS data, the middle row shows the predictions of the Baugh2005 model, and the bottom row gives those of the Bower2006 model. In this plot, each galaxy contributes $1/V_{\rm max}$ to the density. The contours in the plot indicate the regions containing 68% and 95% of the number density of galaxies in the samples. Note that the colour shading scales

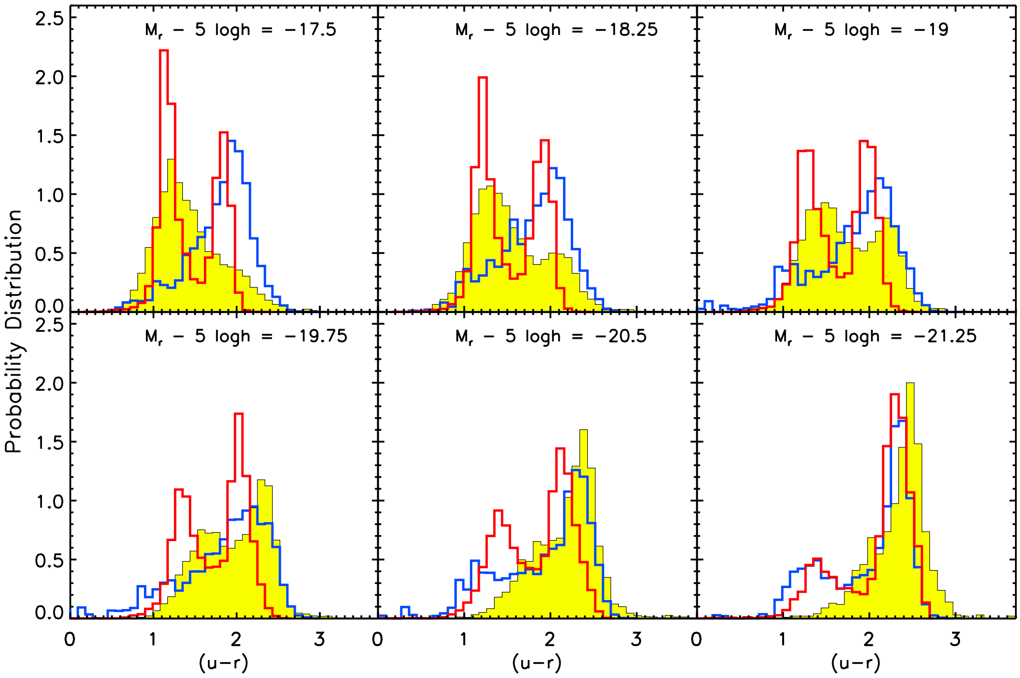

Figure 3.9: The $(u-r)$ colour distribution as function of luminosity for the Baugh2005 model (blue histograms), the Bower2006 model (red histograms) and the SDSS data (yellow histograms). The centre of the magnitude bin used in each panel is given by the legend. All the histograms are normalized to have unit area.

as the square root of the density.

For the case of the SDSS data in all colours except for $(i-z)$ we can see a bright red population and a fainter, bluer population as indicated by the splitting of the 68% density contour. The Baugh2005 model predicts a dominant red population at the brightest magnitudes. On moving to fainter magnitudes, bluer galaxies appear but red galaxies still dominate and there is no clear bimodality. The Bower2006 model displays a strong bimodality in colour, though with a bluewards shift in the locus of the colour-magnitude relation compared with the observations. Font et al. (2008) obtained better agreement of their model with the observed locus of red galaxies in the SDSS by increasing the assumed yield of metals by a factor of two relative to the Bower2006 model.

In Fig. 3.11 we plot a similar colour-magnitude distribution, but this time each galaxy contributes $L/V_{\rm max}$ to the density. By doing this more emphasis is given to brighter galaxies. As a consequence, the bimodality in the SDSS data is less readily apparent.

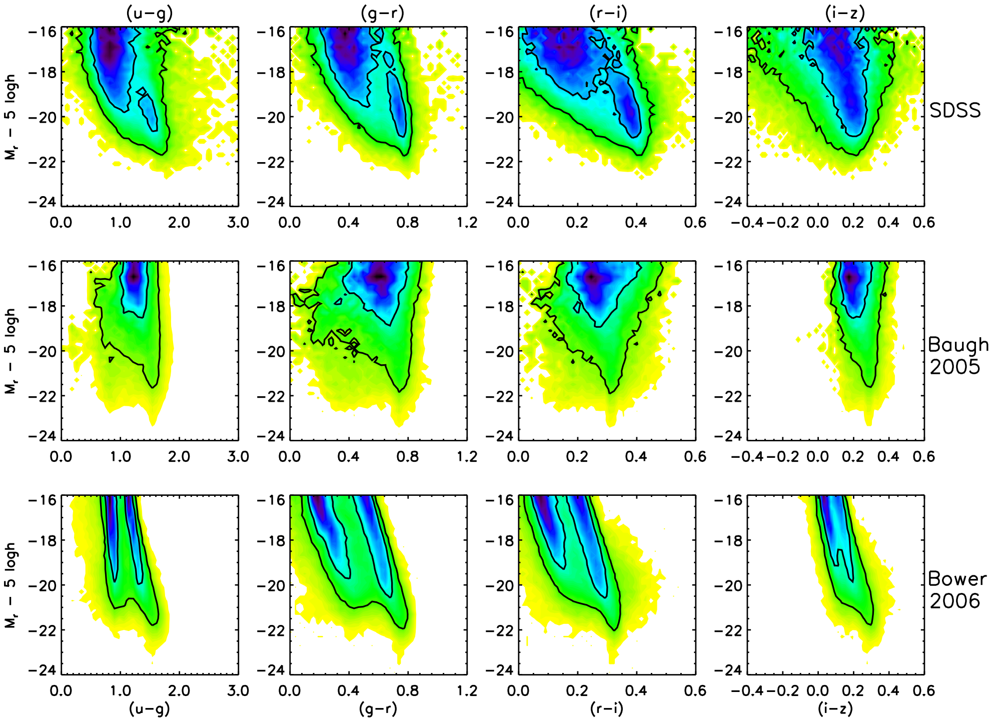

Figure 3.10: The galaxy distribution in the colour magnitude plane. Each column shows the distribution for a different colour. The top row shows the SDSS distributions, the middle row the predictions of the Baugh2005 model and the bottom row the Bower2006 model. Galaxies are weighted by $1/V_{\mathrm{max}}$. The inner contour encloses 68% of the total number density of galaxies and the outer contour encloses 95% of the density. The colour shading reflects the square root of the number density.

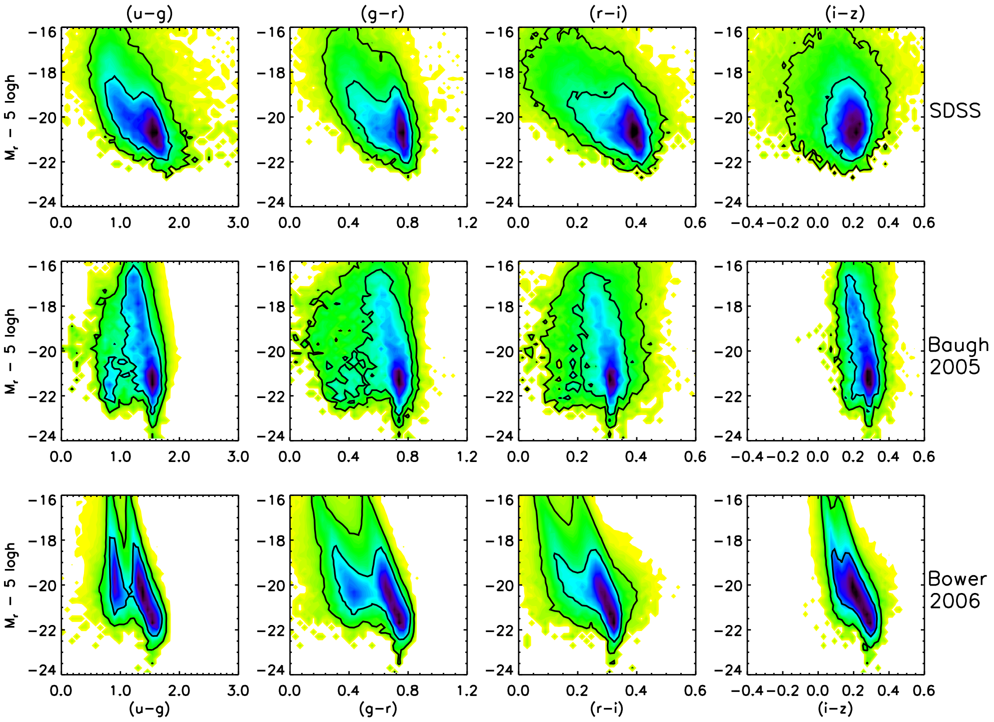

Figure 3.11: The same as Fig. 3.10, but with each galaxy weighted by the product of its luminosity and $1/V_{\rm max}$.

Intriguingly, the Baugh2005 model appears visually to be in better agreement with the observations when presented in this way.

3.3.4 Colour Distribution by Morphology

The bimodality of the colour-magnitude relation seen for SDSS galaxies suggests that different populations or types of galaxy dominate at different magnitudes. We also saw in Section 3.3.2 that disk-dominated galaxies are more abundant at faint magnitudes and the bulge-dominated population is more prevalent at bright magnitudes. A correlation is therefore expected between morphology, colour and luminosity. To see this effect more clearly, we use the Sérsic index, n, to separate galaxies into an "early-type" bulge-dominated population (with $n > 2.5$) and a "late-type" disk-dominated population ($n < 2.5$) and replot the colour-magnitude relation.

We calculate the median Petrosian colour for $(u-g), (g-r), (r-i), (i-z)$ in bins of magnitude M_r for the two populations. The results are plotted in Fig. 3.12 for the models and the SDSS data. We can see from the SDSS data that the different populations display different colour-magnitude correlations, confirming that the Sérsic index is an effective morphological classifier. The bulge-dominated galaxies are redder than the disk-

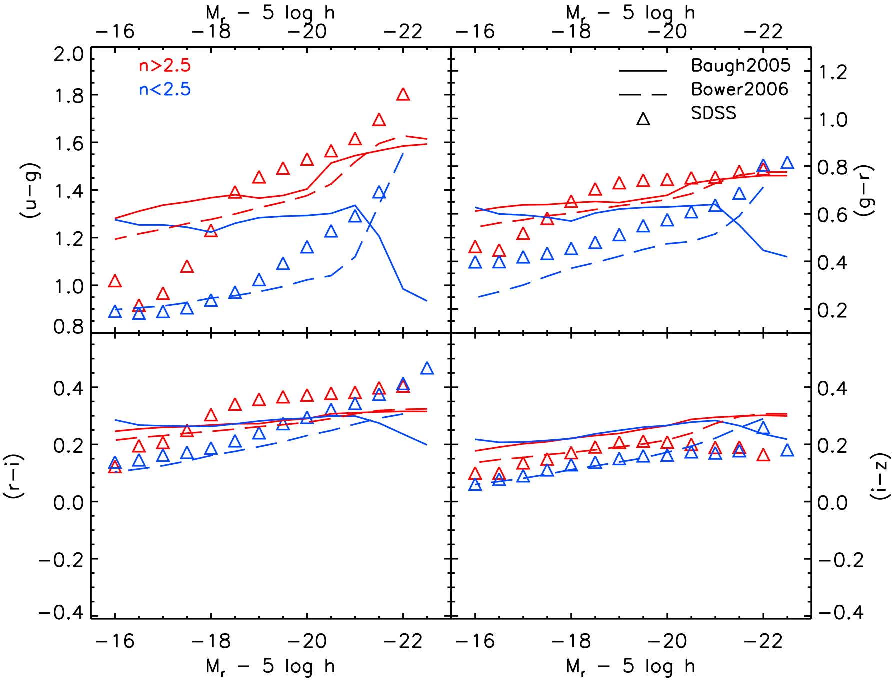

Figure 3.12: The median colour $(u-g), (g-r), (r-i), (i-z)$ for the models (continuous lines) and SDSS galaxies (triangles) as a function of magnitude M_r. Different coloured lines and symbols correspond to different morphological types of galaxies, as given by the Sérsic index ($n < 2.5$ for the disk-dominated population and $n > 2.5$ for the bulge-dominated population). Each panel corresponds to a different colour. The panels each have the same range of colour on the y-axis. The results are plotted only when there are ten or more galaxies present in a bin.

dominated galaxies, with the size of the difference decreasing as the effective wavelength of the passbands increases. Also, at fainter magnitudes, the colours of the two populations tend to become more similar.

In the Baugh2005 model, Fig. 3.12 shows that the populations split by Sérsic index have similar colours except for the brightest galaxies. Both populations are predicted to be too red at faint magnitudes. At brighter magnitudes ($M_r - 5\log h < -19$), bulge-dominated galaxies show similar behaviour to the SDSS data. Disk-dominated galaxies become bluer at the brightest magnitudes, which is opposite to the trend seen in the data. The Bower2006 model predicts a clear separation in colour for populations classified by Sérsic index, with blue disk-dominated galaxies even at faint magnitudes, which is in better agreement with SDSS data. In both models, the faint bulge-dominated population is predicted to be too red.

3.3.4.1 What Drives the Colours? A Look at the Specific Star Formation Rate and Metallicity

To identify which feature of the models is producing the differences in colour seen in Fig. 3.12, we now examine the specific star formation rate SSFR (the star formation rate [SFR] per unit stellar mass) and stellar metallicity of galaxies in both models. The specific star formation rate quantifies how vigorously a galaxy is forming stars in terms of how big a contribution recent star formation makes to the total stellar mass. Galaxies with a high specific star formation rate will tend to have bluer colours and stronger emission lines than more "passive" galaxies. We use the Sérsic index to separate the galaxies as before, into an "early-type" bulge-dominated population (with $n > 2.5$) and a "late-type" disk-dominated population ($n < 2.5$). In the top panel of Fig. 3.13 we plot the median of the SSFR as a function of magnitude M_r. In the bottom panel of this figure we plot the median of the V-band luminosity-weighted stellar metallicity. The top panel of Fig. 3.13 shows that bulge-dominated galaxies have very low specific star formation rates in both models. The disk-dominated galaxies have very different specific star formation rates in the two models. In the Bower2006 model, the disk-dominated galaxies are undergoing significant amounts of star formation, except at the brightest magnitudes. Although the strength of supernova feedback is stronger in the Bower2006 model than it is in the Baugh2005 model, reheated gas tends to recool on a shorter timescale because it is reincorporated into the hot halo faster. The drop in the specific star formation rate for the brightest galaxies in the Bower2006 model can be traced to the AGN feedback

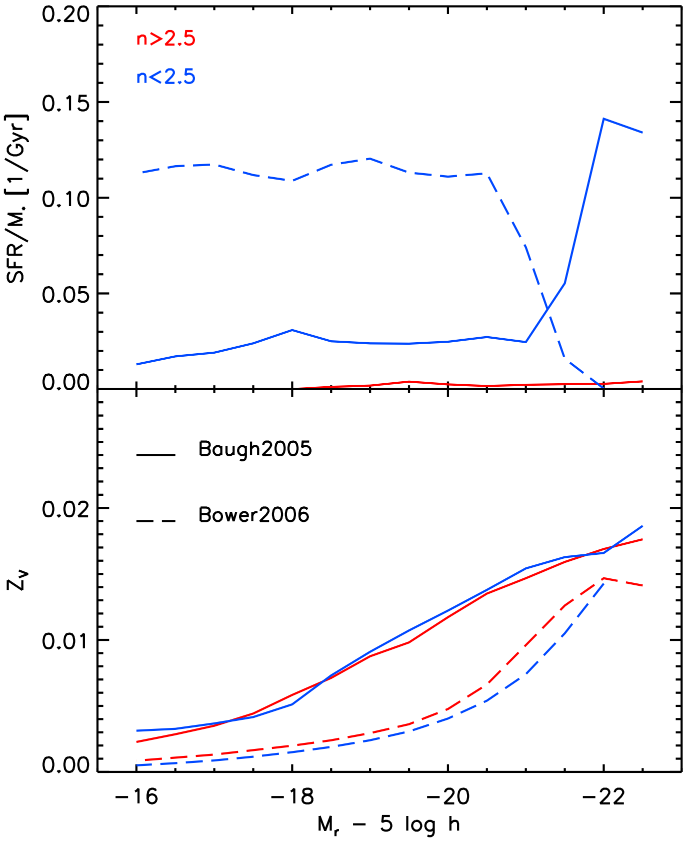

Figure 3.13: The top panel shows the specific star formation rate, i.e. the star formation rate per unit stellar mass, as a function of magnitude M_r for the `GALFORM` models, as indicated by the key in the lower panel. The lower panel shows the stellar metallicity, weighted by the V-band luminosity as a function of magnitude M_r. Different colours correspond to different morphological types as set by the Sérsic index, as shown by the label in the top panel.

which shuts down gas cooling for these galaxies. Note that disk-dominated galaxies make up only a small fraction of the galaxies at these magnitudes. Within a given model, the metallicities of the disk and bulge-dominated populations are similar. However, the metallicities in the Baugh2005 model are higher than in Bower2006, presumably because some fraction of the star formation in the former model occurs in starbursts with a top-heavy IMF, which correspondingly produces a higher yield of metals. Hence, given these differences, one expects bluer galaxies at faint magnitudes in the Bower2006 model than in the Baugh2005 model.

3.3.4.2 Correlation Between Sérsic Index, Colour and Magnitude

To investigate further the correlation between the Sérsic index, colour and absolute magnitude, we plot in Fig. 3.14 the luminosity weighted density in the various projections of the Sérsic index (n), $(g-r)$ colour and M_i absolute magnitude plane, both for SDSS data and `GALFORM` models. In the data we can see that disk-dominated galaxies (i.e. those with small n values) tend to be bluer and also fainter, whereas the bulge-dominated galaxies (those with large n values) tend to be redder and brighter. The predictions of both `GALFORM` models are peaked around Sérsic indices of $n = 1$ (nominally pure disk galaxies) and $n = 4$ (pure bulge galaxies). Despite these density peaks, the numbers of galaxies in the different morphological classes are similar to the SDSS data (as shown in Fig. 3.6) showing that at a broad-brush level, the distribution of n predicted by the `GALFORM` models is in reasonable agreement with the observations.

Bearing in mind the level at which the models are able to match the distribution of Sérsic indices, both models reproduce fairly well the behaviour seen in the SDSS observation, with a spike corresponding to a faint blue disk-dominated population, which changes to a red, bulge-dominated population at bright magnitudes. Compared with the SDSS, the Baugh2005 model overpredicts the number of red disk-dominated galaxies (around values $(g-r) \sim 1$ and $n \sim 1$) and the number of moderate luminosity bulge-dominated galaxies (around values $M_i - 5\log h \sim -19$ and $n \sim 4$). The Bower06 model predicts a distribution which agrees better with the observational data.

3.3.5 The Distribution of Disk and Bulge sizes

We now examine the model predictions for the linear size of the disk and bulge components of galaxies. We compare the model predictions with SDSS observations using the radius enclosing 50% of the Petrosian flux, R_{50}. The calculation of disk and bulge sizes was

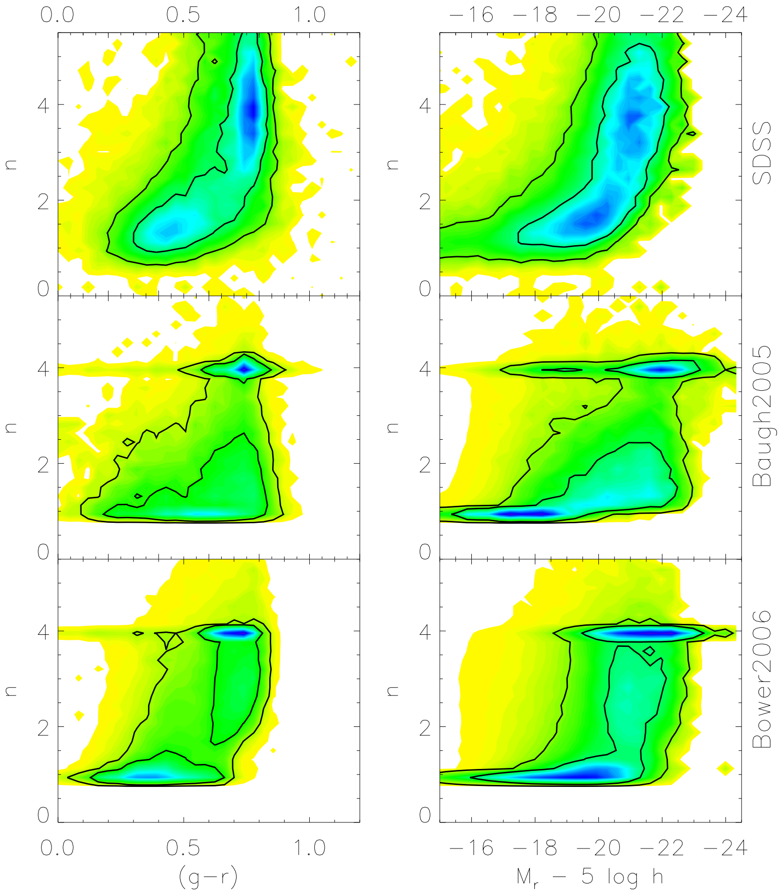

Figure 3.14: The luminosity-weighted density of galaxies in different projections of the Sérsic index (n), (g-r) colour and magnitude plane. Contours indicate the regions containing 68% and 95% of the total density of galaxies. Top panels: SDSS data, intermediate panels: Baugh2005 model and bottom panels: Bower2006 model.

reviewed in Section 2.3 and Section 2.4 of this thesis. We use the concentration index, c, to divide galaxies into two broad classes of disk-dominated and bulge-dominated samples. First we discuss the accuracy of the predictions for R_{50} for disk-dominated galaxies and then for bulge-dominated galaxies, before illustrating the sensitivity of the results to various physical ingredients of the models. The observations we compare against are our own analysis of the size distribution in the NYU-VAC constructed from DR4, as discussed below, and the results from Shen et al. (2003; hereafter Sh03), which were derived from a sample of 140000 galaxies from DR1.

3.3.5.1 Disk-Dominated Galaxies

Following Sh03, we take $c < 2.86$ to define the disk-dominated sample (recall that pure disk galaxies have $c \sim 2.3$ and pure bulges have $c \sim 3.3$, as shown by Fig. 3.2). Besides the selection introduced by use of the SDSS spectroscopic sample ($r_{\rm Pet} < 17.77$), further selection criteria are required in the size distribution analysis. The size measurement for compact galaxies could be affected by the point-spread function of the image or because these objects could be misclassified as stars by the SDSS imaging processing software. To minimize such contamination, Sh03 selected galaxies with angular sizes $R_{50} > 1.6''$ (this excludes only a few percent of the galaxies). Sh03 further restricted the sample to galaxies with surface brightness $\mu_{50} \leq 23.0$ mag arcsec^{-2}, and apparent magnitude in the range $r_{\rm min}(\theta, \phi) \leq r \leq r_{\rm max}(\theta, \phi)$ with, typically, $r_{\rm min} \sim 15.0$ and $r_{\rm max} \sim 17.77$, and redshift $z \geq 0.005$.

We apply the same criteria as used by Sh03 to the low redshift NYU-VAGC catalogue. This requires us to recalculate the value of $V_{\rm max}$ needed to construct statistical distributions, to take into account the bright magnitude limit, size cut and surface brightness cut. Note that although the Sh03 sample is from the smaller DR1, it contains more galaxies than the NYU-VAGC sample used here because it extends to higher redshift.

The correlation of size with luminosity for disk-dominated galaxies is shown in the upper six panels of Fig. 3.15, in which we plot the distribution of R_{50} in selected magnitude bins in the $r-$band. The `GALFORM` predictions are plotted as unshaded histograms, with the Baugh2005 results in blue and the Bower2006 results in red. The observed distributions are shown by the yellow filled histograms. Except for the brightest two magnitude bins shown, the models tend to overpredict the size of disk-dominated galaxies, particularly in the case of the Bower2006 model. In the Baugh2005 model, the peak of the distribution shifts to larger sizes with brightening magnitude, reproducing the trend seen in the observations. On the other hand in the Bower2006 model, there is little dependence of disk size on luminosity. Both models display a larger scatter in sizes than is seen in the data. The panels for early-types are discussed in the next section.

To further quantify the trend of size with luminosity, we calculate the median value of R_{50} and plot the results in Fig. 3.16, where the continuous green line represents the fiducial `GALFORM` model (the left panel shows the results for the Baugh2005 model and the right panel for the Bower2006 model) and open symbols represent the NYU-VAGC data, where we overplot for comparison (and to check for consistency) the results from Sh03 (filled triangles). Fig. 3.16 shows that our analysis of the size distribution in the NYU-VAGC is consistent with the results of Sh03. The apparent magnitude cut $r_{\rm min}$ together with using a low-redshift sample in comparison with Sh03, removes the galaxies brighter than $M_r - 5\log h = -21.5$.

The SDSS data show an increase of over one decade in R_{50} across the luminosity range plotted for disk-dominated galaxies. This increase is reproduced by the predictions of the Baugh2005 model. The behaviour of the Bower2006 model is quite different, with an essentially flat size-luminosity relation to L_*, followed by a decrease in size for brighter galaxies. We investigate the impact of various processes on the form of the size predictions in Section 3.4.

3.3.5.2 Bulge-Dominated Galaxies

We select a bulge-dominated sample by taking those galaxies with concentration index $c > 2.86$. In the lower six panels of Fig. 3.15, we plot the distribution of sizes R_{50} for bulge-dominated galaxies for a selection of magnitude bins. In general, the model predicts values of R_{50} larger than observed, except for the $M_r - 5\log h = -20.5$ bin for Bower2006 and $M_r - 5\log h = -21.25$ for Baugh2005. As for the case of disk-dominated galaxies, the predicted scatter in sizes is larger than observed.

We plot the median size of the bulge-dominated samples in the top row row of Fig. 3.16. The predicted size-luminosity relation is flatter than observed, turning over at the brightest magnitudes plotted. The brightest galaxies are three to five times smaller than observed, confirming the conclusion reached by (Almeida et al., 2007).

As the DR4 data set we are working with covers a larger solid angle than the sample used by Sh03, the combined set of data measurements covers a wider range of magnitudes than can be reached by either sample alone. Again where there is overlap, we find that our analysis of DR4 is consistent with the results of Sh03.

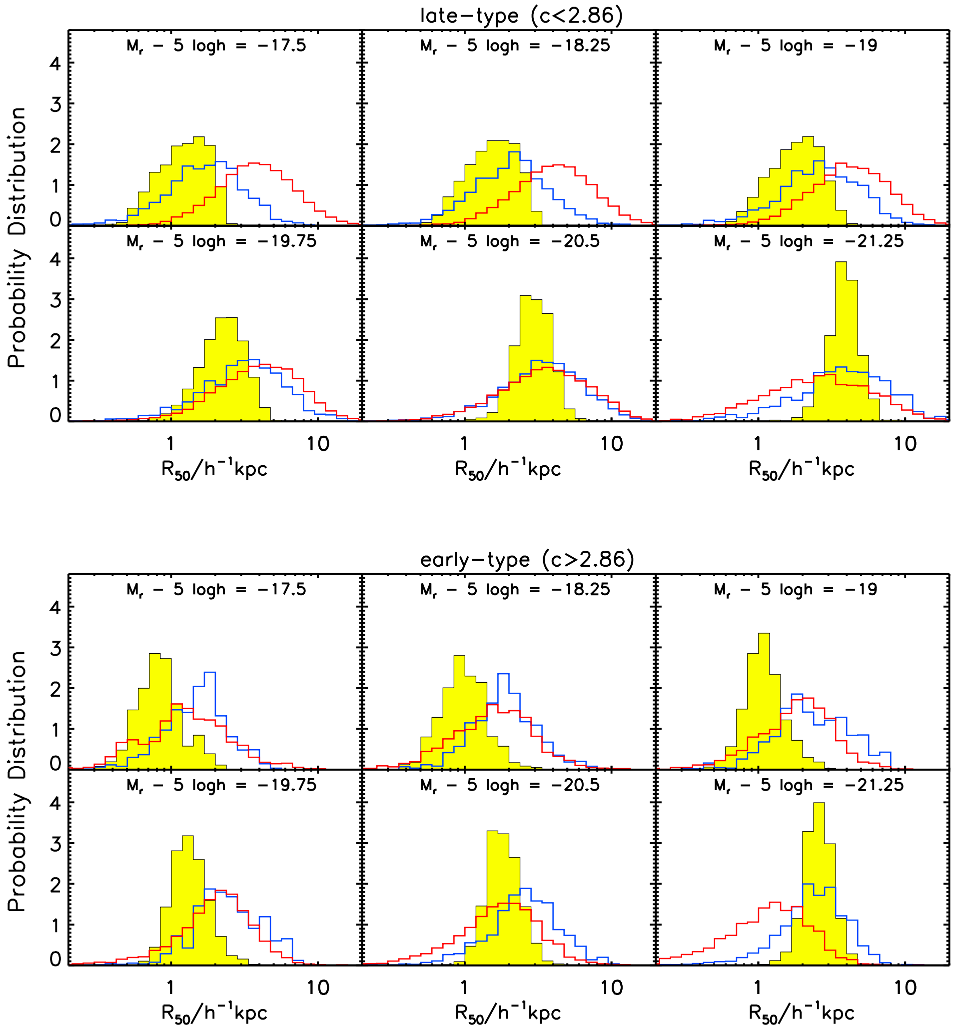

Figure 3.15: The distribution of the Petrosian half-light radius, R_{50}, for early type galaxies (with concentration parameter $c > 2.86$) in the top six panels and for late type galaxies ($c < 2.86$) in the lower six panels. Each panel corresponds to a different one magnitude wide bin, as indicated by the legend. The `GALFORM` predictions are shown by unshaded histograms (Baugh2005 - blue; Bower2006 - red) and the SDSS data by the yellow shaded histogram. All of the histograms are normalized to have unit area.

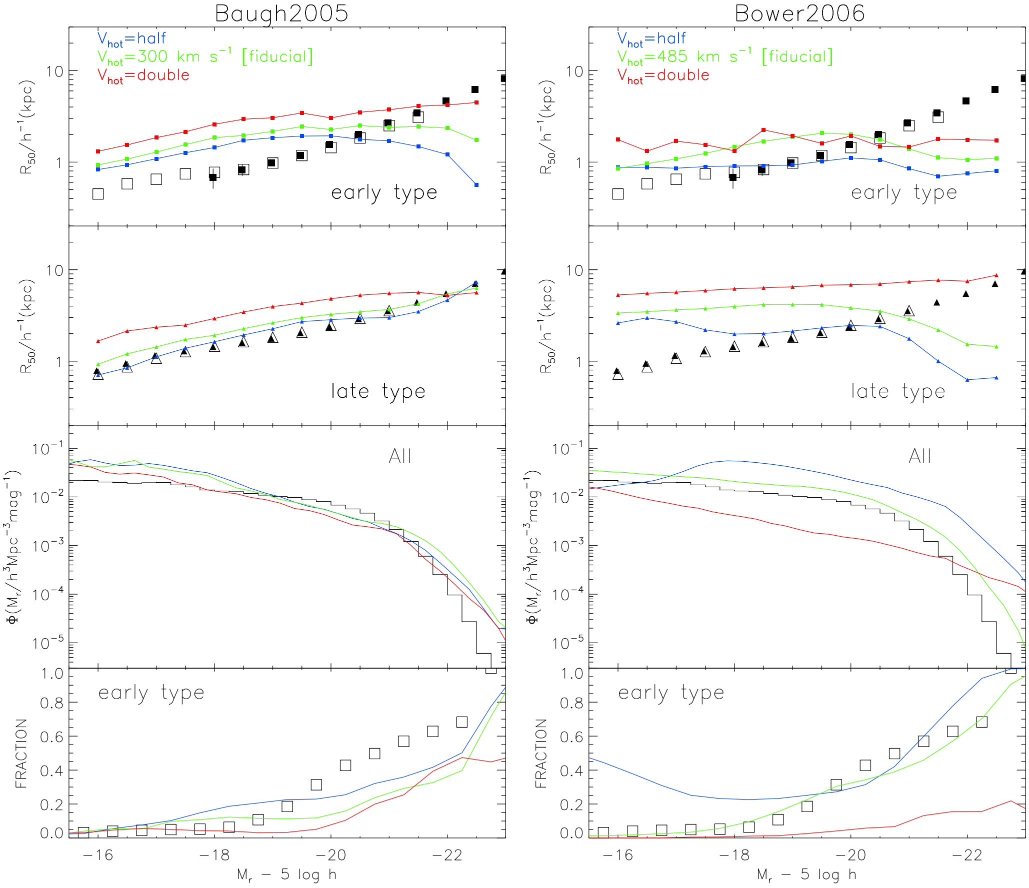

Figure 3.16: A compilation of predictions for the Baugh2005 (left) and Bower2006 (right) models. The top row shows the median R_{50} as a function of magnitude for bulge-dominated galaxies ($c > 2.86$), the second row shows the median R_{50} for disk-dominated galaxies ($c < 2.86$), the third row shows the $r-$band luminosity function of all galaxies and the bottom row shows the fraction of early-type galaxies as a function of magnitude. The predictions of the fiducial model in both cases are shown by the green lines. In this plot, we also show the impact of changing the strength of supernova feedback, rerunning the model with either half the fiducial value of $V_{\rm hot}$ (blue curves; see Section 2.3.4) or twice the value (red curves). In first and second rows, the open symbols show our determination of the median size from the NYU-VAGC; the filled symbols show the results obtained by Sh03. The black histogram in the third row shows our determination of the luminosity function in DR4 using the $1/V_{\rm max}$ estimator. The squares in the bottom row show the fraction of early-types in the NYU-VAGC, defined according to concentration parameter $c > 2.86$, as a function of magnitude.

3.4 Sensitivity of the Predictions to Physical Ingredients

The calculation of sizes involves several components as outlined in Section 2.3 and Section 2.4. Given that this is the area in which, overall, the model predictions agree least well with the observations, it is instructive to vary some of the physical ingredients of the model to see if the agreement can be improved. In the tests which follow, we vary the strength of one ingredient at a time and assess the impact on the size-luminosity relation. We also show the effect of the parameter change on the form of the overall galaxy luminosity function and the mix of morphological types. These variant models are not intended to be viable or alternative models of galaxy formation, but instead allow us to gain some physical insight into how the model works.

(i) *The strength of supernova feedback.*

SN feedback plays an important role in setting the sizes of disk galaxies, by influencing in which haloes gas can remain in the cold phase to form stars. Cole et al. (2000) demonstrated that increasing the strength of SN feedback results in more gas cooling to form stars in more massive haloes, which leads to larger disks. Conversely, reducing the feedback allows gas to cool and form stars in smaller haloes resulting in smaller discs. The strength of SN feedback is parameterized using $V_{\rm hot}$ and $\alpha_{\rm hot}$ as shown in Eq. 2.15. The adopted values for these parameters are: $V_{\rm hot} = 300\,{\rm km\,s^{-1}}$ and $\alpha_{\rm hot} = 2$ in the Baugh2005 model and $V_{\rm hot} = 485\,{\rm km\,s^{-1}}$ and $\alpha_{\rm hot} = 3.2$ in the Bower2006 model. We perturb the models by increasing and reducing the value of $V_{\rm hot}$ to double and half the fiducial value in each model, and plot the results in Fig. 3.16. The normalization of the size-luminosity relation for disk-dominated galaxies changes as expected on changing the strength of supernova feedback, moving to larger sizes on increasing $V_{\rm hot}$ and smaller sizes on reducing $V_{\rm hot}$. Reducing $V_{\rm hot}$ in the Baugh2005 model leads to better agreement with the observed size-luminosity relation for disk-dominated galaxies, at the expense of producing slightly more faint galaxies. Similar trends are seen in the predictions for the size-luminosity relation of bulge-dominated galaxies. Note that there are very few bulge-dominated galaxies at faint magnitudes in the Bower2006 model, hence the noisy size-luminosity relation in this region. Changing the strength of feedback in this way has little impact on the slope of the size-luminosity relation.

(ii) *The threshold for disks to become unstable.*

The threshold for a disk to become unstable is set by the threshold $\epsilon < \epsilon_{\rm disk}$ (see Eq. 2.29). We show the result of varying this threshold in Fig. 3.17. In the case of the Bower2006 model, we increase and reduce the threshold from the fiducial value of $\epsilon_{\rm disk} = 0.8$; increasing the threshold means that more disks become unstable. The original Baugh2005 model does not test for the stability of disks, so in this case we switch the effect on and try two different values for the threshold. The result of turning on dynamical instabilities is straightforward to understand in this model. For a given mass and rotation speed of disk, the stability criteria $\epsilon \propto \sqrt{r_{\rm disk}}$, and so disks with smaller values of $r_{\rm disk}$ will preferentially be unstable. The removal of small disks raises the median disk size but reduces the fraction of galaxies that are disk-dominated. The impact of varying the stability threshold on the Bower2006 model is less easy to interpret: even though the fraction of faint disk-dominated galaxies fails dramatically on increasing the threshold, there is little change in the median size of the surviving disks. This change has a bigger impact on the size of bulge-dominated galaxies, with a sequence that is inverted compared with the Baugh2005 model. One result that is easily understood is the response of the luminosity function. The burst of star-formation which can accompany the transformation of a dynamically unstable disk into a bulge is an important channel for generating black hole mass in the Bower2006 model. If fewer disks become unstable, less mass is converted into black holes and AGN feedback has less impact on the cooling flows in massive haloes, leading to too many bright galaxies.

(iii) *The orbital energy of merging galaxies*

The parameter $f_{\rm orbit}$ quantifies the orbital energy of two galaxies which are about to merge (Eq. 2.31). Our standard choice in both models is $f_{\rm orbit} = 1$, in which case Eq. 2.31 is equal to the energy of two point masses in a circular orbit at a separation of $r_1 + r_2$. We vary the value of $f_{\rm orbit}$ trying $f_{\rm orbit} = 0$, which corresponds to a parabolic orbit, and $f_{\rm orbit} = 2$. The results are plotted in Fig. 3.18. As expected, the median size of disk-dominated galaxies is unaffected by varying $f_{\rm orbit}$. Increasing the value of $f_{\rm orbit}$ makes bulge-dominated galaxies smaller, with a larger effect seen for brighter galaxies. A smaller value of $f_{\rm orbit}$ improves the shape of the size-luminosity relation of bulge-dominated galaxies in the Baugh2005 model; however, faint bulge-dominated galaxies are still too large after making this change.

(iv) *The contribution of the dark matter in galaxy mergers*

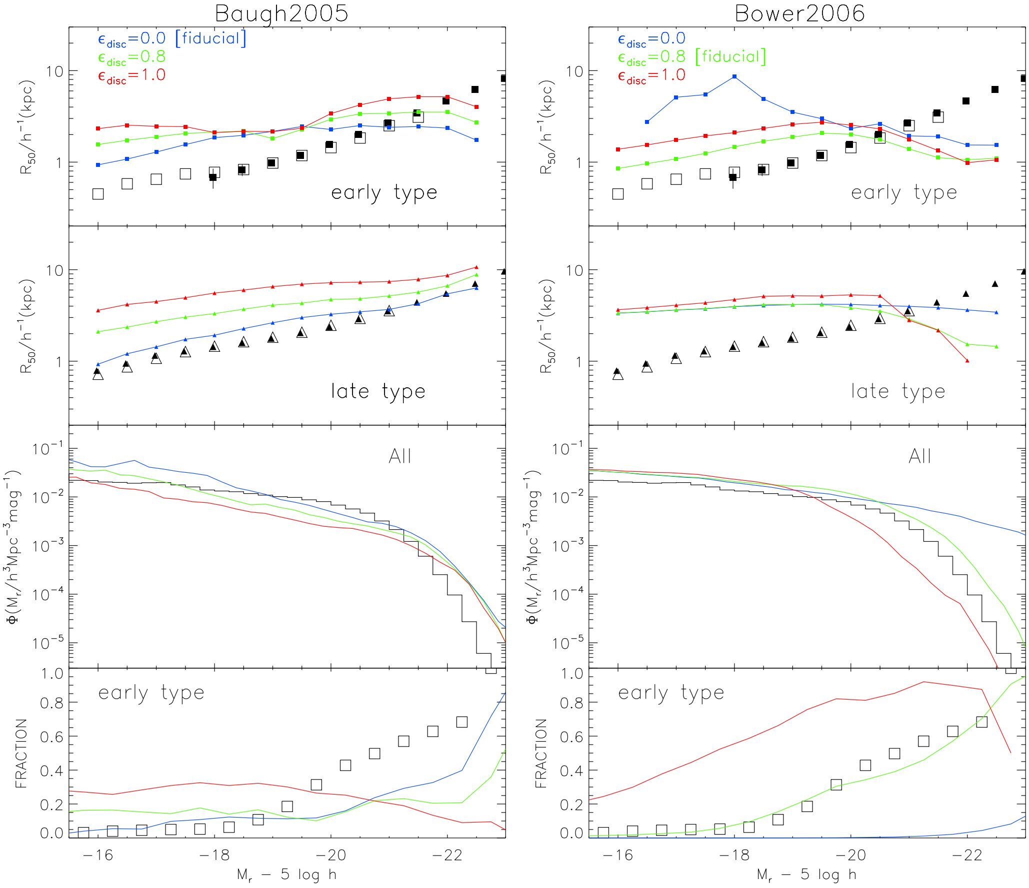

Figure 3.17: Similar to Fig. 3.16, but varying the disk instability threshold $\epsilon_{\rm disk}$ in Eq. 2.29.

The parameter $f_{\rm dark}$ controls the amount of dark matter associated with model galaxies during merger evenst (see Eq. 2.32), which has an impact on the size of the merger remnant, through Eq. 2.31 and Eq. 2.34. We run the models using values of $f_{\rm dark} = 1$ and $f_{\rm dark} = 0$, the latter of which corresponds to the case of a galaxy without participating dark matter. We can see that the reduction of $f_{\rm dark}$ from the fiducial value leads to smaller sizes for the early type galaxies in both models. The effect is particularly important at bright magnitudes. As expected, there is no change in the predicted sizes for late type galaxies. We do not find, either, a variation in the luminosity function, but there is an increase in the fraction of early type galaxies, particularly at intermediate magnitudes. We can see that we can improve the sizes of early type galaxies, matching with those inferred from SDSS observations for galaxies with magnitudes fainter than $L\star$. However, this change is counterproductive at bright magnitudes, resulting in even smaller sizes.

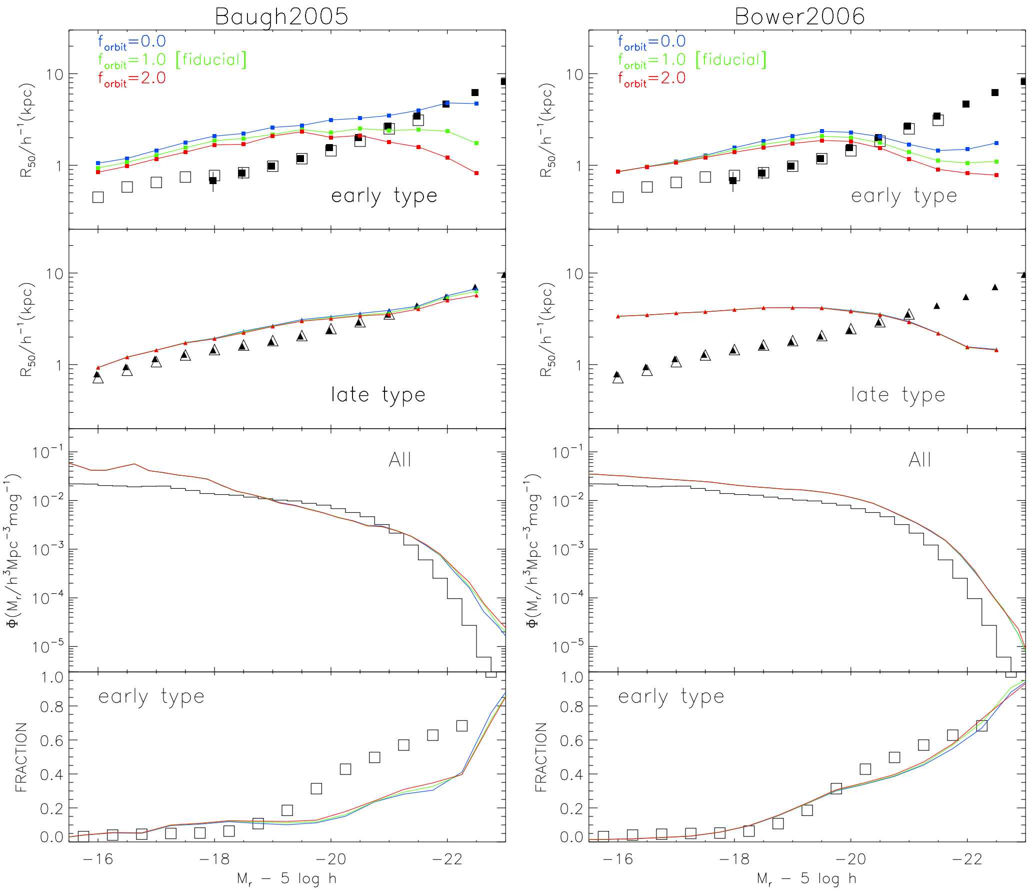

Figure 3.18: Similar to Fig. 3.16, but varying the $f_{\rm orbit}$ parameter in Eq. 2.34.

3.4.1 What Drives the Slope of the Size-Luminosity Relation?

We have seen that the prediction of the Bower2006 model for the size-luminosity relation of disk-dominated galaxies is much flatter than that of the Baugh2005 model (Fig. 3.16). Moreover the Baugh2005 model is in better agreement with the observed relation. In the previous section we varied selected model parameters one at a time relative to the fiducial model, to show their impact on the model size-luminosity relation. In this exercise, the most dramatic change in the Bower2006 predictions resulted from varying the strength of SNe feedback. Reducing the value of the parameter $V_{\rm hot}$, which sets the "pivot" velocity below which SNe feedback has a strong impact, leads to a shift in the size-luminosity relation to smaller sizes, with an improved match to the observed relation recovered for intermediate luminosity galaxies. In this section, we investigate the effect of varying several parameters together, essentially moving from the Bower2006 parameters for SNe feedback and the star formation timescale in disks, towards a set which more closely

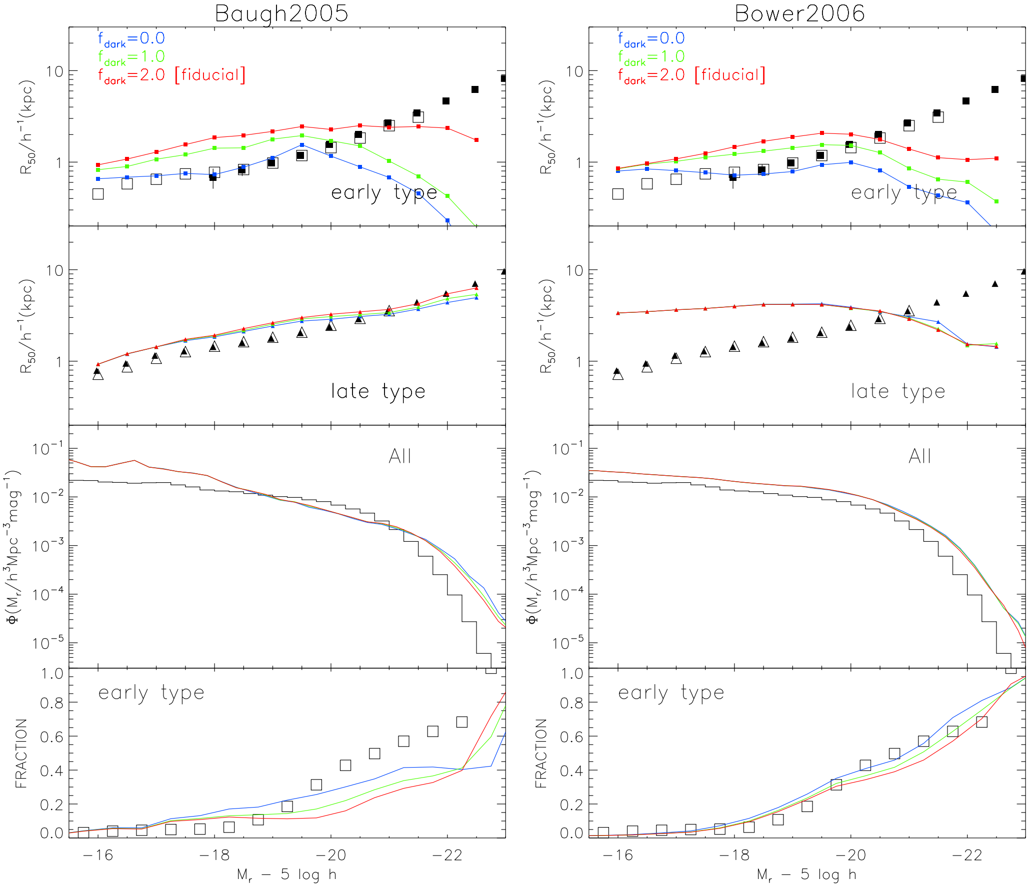

Figure 3.19: Similar to Fig. 3.16, but varying the $f_{\rm dark}$ parameter in Eq. 2.32

resembles that used in the Baugh2005 model. The size-luminosity relations for disk- and bulge-dominated galaxies are plotted in Fig. 3.20 for a sequence of models. The starting point is the fiducial Bower2006 model. For each step in the sequence, one parameter is varied relative to the previous step, as shown in the key in Fig. 3.20. The first change made is to the value of $\alpha_{\rm hot}$, which controls the slope of the SNe feedback. Changing from the Bower2006 value of $\alpha_{\rm hot} = 3.2$ to $\alpha_{\rm hot} = 1$ gives a much improved match to the observed size-luminosity relation, particularly for intermediate luminosities. Faint disk-dominated galaxies are still somewhat too large, and bright galaxies in general are still too small. The next step is to retain the above change to $\alpha_{\rm hot}$, and also to change the value of $V_{\rm hot}$ to that used in Baugh2005. This results in a modest improvement in the size-luminosity relation for faint galaxies. Finally, the scaling of the quiescent star formation timescale with the disk dynamical time is switched off. The resulting size-luminosity relation is now in very good agreement with the observations for disk-dominated galaxies. However,

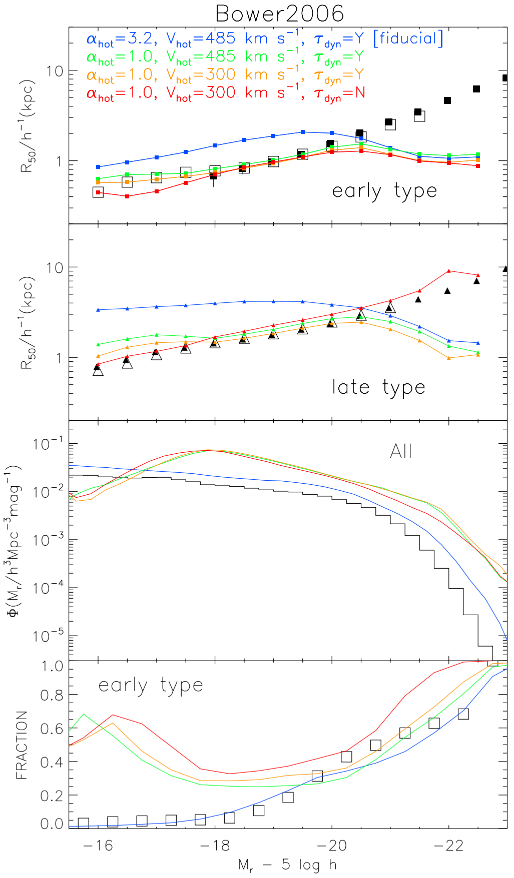

Figure 3.20: The impact of cumulative parameter changes for a sequence of models, starting from the fiducial model of Bower2006 (blue). One parameter is changed in each step, but unlike the cases presented in Figs. 16, 17, 18, 19, the change made is relative to the previous model in the sequence. The key lists the parameter change relative to the previous model in the sequence. The upper two panels show the size-luminosity relation for bulge and disk-dominated galaxies respectively. The third panel shows the luminosity function and the bottom panel shows the morphological mix of galaxies as a function of luminosity.

bright bulge-dominated galaxies are still too small. Furthermore, the luminosity function and the predicted fraction of early types with luminosity are now much poorer matches to observations than in the fiducial Bower2006 model (lower two panels of Fig. 3.20).

In summary, even though the sizes of disk-dominated galaxies can be brought into reasonable agreement with observations in a variant of the Bower2006 model with modified SNe feedback and disk star formation timescale, this is at the expense of agreement with the observed luminosity function and early-type fraction. Furthermore, neither the fiducial Baugh2005 model nor the fiducial or modified Bower2006 models are able to reproduce the observed sizes of early-type galaxies, in particular for bright galaxies. No single parameter change seemed able to solve the latter problem. The most promising area to explore further appears to be the modelling of galaxy mergers; changing the amount of orbital energy brought in by merging galaxies in our prescription led to an increase in the sizes of the brightest bulge-dominated galaxies.

3.5 Summary and Discussion

Observations of local galaxies have always played a central role in setting the parameters of galaxy formation models. However, the huge size of the SDSS sample combined with the quality and uniformity of the data allow much more precise and exacting tests of the physics of such models than was previously possible. To take full advantage of this opportunity, it is necessary for the model to be able to generate predictions which are as close as possible to the measurements made for real galaxies. In this Chapter we use the `GALFORM` model, which predicts the size of both the disk and bulge components of galaxies. Hence we are able to take the model output for the luminosity and scale-lengths of a galaxy's disk and bulge and turn these into predictions for the quantities measured for SDSS galaxies: the Petrosian magnitude, the radius containing 50% of the Petrosian flux (R_{50}), the concentration parameter (c) and the Sérsic index (n), the latter two quantities providing descriptions of the light profile of the galaxy.

The first major result of this work is to understand the correlation between different indicators of galaxy morphology. The concentration parameter, Sérsic index and bulge-to-total (B/T) luminosity ratio have all been used to divide galaxies into morphological classes (e.g Bershady et al., 2000; Hogg et al., 2004; Benson et al., 2007). The B/T ratio is easy to compute theoretically, yet is perhaps the hardest of these quantities to measure observationally. Both the c-B/T and n-B/T planes show scatter. This can be traced to the ratio of the disk and bulge scale-lengths; galaxies with different values of this ratio occupy different loci in the c-B/T and n-B/T planes. The scatter is particularly large in the case of the Sérsic index n versus B/T. The scatter would be even larger if we simply generated galaxies by hand, taking the ratio of disk and bulge scale-lengths from a grid. The scatter we find is limited by the distribution of $r_{\rm d}/r_{\rm b}$ values predicted by `GALFORM`.

We compared the predictions of two different versions of the `GALFORM` model with SDSS data: that of Baugh et al. (2005), which has a top-heavy IMF in starbursts and feedback from superwinds, and Bower et al. (2006), which has AGN feedback and a normal IMF in all modes of star formation. In the first stage of the comparison, none of the model parameters were adjusted to improve the fit to the data. The models gave reasonable matches to the total galaxy luminosity function, with the Bower et al. model giving the best overall match to the shape. The match to the luminosity function of different colour subsamples is less impressive; both models overpredict the number of bright blue galaxies and fail to match the number of red galaxies. The Bower et al. model has a strongly bimodal colour distribution, whereas the Baugh et al. model shows only weak bimodality. The Bower et al. model agrees better overall with the observed colours in SDSS, although the predicted bimodality appears somewhat too strong, and the positions of the peaks in the colour distribution do not agree exactly with what is observed.

Another clear success of the models is in predicting the correct trend of morphological type with galaxy luminosity. We used all three morphological indicators (concentration parameter, Sérsic index and bulge-to-total luminosity ratio from disk+bulge fits) to separate galaxies into disk-dominated and bulge-dominated types. In the SDSS data, the fractions of these types are found to shift from being almost completely disk-dominated at low luminosity to almost entirely bulge-dominated at high luminosity, though with differences in the detailed behaviour depending on which morphological indicator is used. Both the Baugh et al. (2005) and Bower et al. (2006) models successfully reproduce this general trend, although the Bower et al. model agrees better in detail with the observed behaviour at intermediate luminosities. Both models qualitatively reproduce the observed correlation of colour with morphology (with bulge-dominated galaxies on average being redder than disk-dominated galaxies at every luminosity), although quantitatively the Bower et al. model agrees better with the SDSS data, the Baugh et al. model predicting too many red disk-dominated galaxies.

Perhaps the most serious shortcoming of the models is in the predicted galaxy sizes. Whilst the Baugh et al. model gives a very good match to the luminosity-size relation for disks, the sizes of bulge-dominated galaxies do not match the observations. The slope of the size-luminosity relation for bulge-dominated galaxies in the Baugh et al. model matches the observations for faint galaxies, but the normalization is too high. Brighter than L_*, the predicted relation flattens, with the consequence that the brightest bulge-dominated galaxies are around a factor of three too small (see also Almeida et al. 2007). The situation is worse for the sizes predicted by the Bower et al. model; in this case the size - luminosity relation is flat for disk-dominated galaxies, while for bulge-dominated galaxies the predicted sizes at high luminosities fall even further below the observed relation than for the Baugh et al. model. We have demonstrated that a steeper slope for the size-luminosity relation for disk-dominated galaxies can be recovered in the Bower et al. model if we set some physical processes to have the same parameters as used in the Baugh et al. model. The primary improvement in the model predictions is seen on reducing the strength of SNe feedback. Also, by adjusting the star formation timescale in disks by switching off the dependence on the disk dynamical time, we can recover the observed slope of the size-luminosity relation even at high luminosities. However, this improvement in the size - luminosity relation comes at the expense of producing too many galaxies overall.

The differences between the predictions of the two models for the sizes of disk-dominated galaxies lie in the revised cooling model adopted by Bower et al. (2006), the strength of supernova feedback, the inclusion of AGN feedback and the inclusion of dynamical instabilities for disks. In the Bower et al. model, gas which is reheated by supernova feedback is reincorporated into the hot halo on a shorter timescale than in the Baugh et al. (2005) model. Neither model is able to match the observed size of bright bulge-dominated galaxies. We explore a range of processes in the models, varying the strength of supernova feedback, changing the threshold for disks to become unstable, and changing the prescription for computing the size of the stellar spheroid formed in a galaxy merger. The latter seems the most promising solution, at least in the case of the Baugh et al. model. If we neglect the orbital energy of the galaxies which are about to merge (i.e. setting the parameter $f_{\mathrm{orbit}} = 0$), then the sizes of bright galaxies are in much better agreement with the observed sizes (though the faint bulge-dominated galaxies are still too large). A similar change in the predictions results from ignoring the adiabatic contraction of the dark matter halo in response to the gravity of the disk and bulge (Almeida et al., 2007).

The `GALFORM` model is one of the few able to make the range of predictions considered in this thesis and hence to take full advantage of the constraining power of the SDSS. The model for disk sizes works well under certain conditions, albeit with too much scatter. Our analysis suggests that the problems with disk sizes and colours are connected to the treatment of gas cooling and supernova feedback, while the problems with spheroid sizes are probably due to an overly-simplified treatment of the sizes of galaxy merger remnants. The prescription used to compute the size of spheroids is in need of improvement, which will require the results of numerical simulations of galaxy mergers. This study highlights the need to make careful and detailed comparisons with observational data in order guide improvements in the treatment of physical processes in galaxy formation models.

Chapter 4

The Role of Submillimetre Galaxies in Hierarchical Galaxy Formation

4.1 Introduction

Our understanding of the star formation history of the Universe has changed dramatically as new populations of star-forming galaxies have been discovered at high redshifts. A key advance was the discovery of the cosmic far-infrared background by COBE (Puget et al., 1996), with an energy density similar to that in the UV/optical background, which implies that the bulk of star formation over the history of the universe has been obscured by dust, with most of the radiation from young stars being reprocessed by dust grains to far-infrared and sub-mm wavelengths. This was followed by the discovery of the submillimetre galaxies (SMGs) using the Submillimetre Common User Bolometer Array (SCUBA) instrument on the James Clerk Maxwell Telescope (JCMT) (Smail et al., 1997; Hughes et al., 1998), which are generally interpreted as dust-enshrouded galaxies undergoing a starburst. Follow-up studies have concentrated on SMGs with 850 μm fluxes brighter than about 5 mJy. Spectroscopy has revealed that most such SMGs lie at redshifts $z \sim 1 - 3$, with a median around $z \sim 2$, when the Universe had only 20% of its current age (Chapman et al., 2005). Explaining the abundance and redshifts of SMGs has posed a challenge to theoretical models of galaxy formation ever since their discovery.

In the standard picture, due to the high star formation rates inferred in these galaxies (of $\sim 100 - 1000 M_{\odot}\mathrm{yr}^{-1}$ for a standard initial mass function, e.g. Hughes et al. 1998; Chapman et al. 2005), the SCUBA phase is expected to play an important role in the build up of the stars in massive galaxies. Central to this topic are the questions: do

SMGs represent the assembly of massive present day ellipticals? What is the typical duration of the SCUBA phase? What are the typical stellar mass and host halo mass of their descendants? Do the descendants all have high masses, and are they preferentially spheroid-dominated? And finally, what is the overall contribution of the SCUBA phase to the stellar mass of present-day galaxies?

In this chapter we address these questions using the predictions of a semi-analytical model for galaxy formation and evolution. A powerful feature of semi-analytical models is the ability to connect high redshift galaxies to their present-day descendants. Since it is believed that the dust plays a central role in producing the submillimetre radiation observed from SMGs, the model must take into account the energy reprocessed by dust when the spectral energy distribution (SED) is calculated. The analysis in this chapter is based on the Baugh et al. (2005) version of the `GALFORM` semi-analytical model.

The semi-analytical galaxy formation approach has been used by other authors to model submillimetre galaxies. Kaviani et al. (2003) were able to reproduce the number counts of SCUBA sources, but only by treating the dust temperature as a free parameter, for which they needed to choose quite a low value (20-25 K). Fontanot et al. (2007) reproduced the number counts of galaxies in the 850 μm band using a self-consistent calculation of the dust temperature and a standard Salpeter initial mass function for all type of star formation, but their model does not match the observed redshift distribution of SMGs at the fluxes $S_\nu \sim 5$ mJy for which it is currently measured. Swinbank et al. (2008) tested the Baugh et al. (2005) model by comparing in detail the SEDs and stellar, dynamical, gas and halo masses of submillimetre galaxies against observational data, finding broad agreement. No attempt has been made before to relate the predicted SMGs with their present-day descendants.

In Section 4.2, we present examples from the model of galaxy evolution histories which produce SMGs. In Section 4.3, we study properties predicted for SMGs at different redshifts, such as stellar and host halo masses and morphologies, and also the duration of the SMG phase. In Section 4.4, we show the model predictions for the present-day descendants of SMGs, including their stellar and host halo masses and morphologies. In Section 4.5, we compute what fraction of present-day galaxies had SMG progenitors and in Section 4.6 we calculate the contribution of SMGs to the present-day stellar mass density. Finally we present our conclusions in Section 4.7.

4.2 Galaxy Merger Trees: Examples with SMG Progenitors

To follow galaxy evolution in `GALFORM` we output the model predictions at different redshifts. We label a galaxy as a bright SMG when its 850 μm flux exceeds 5 mJy. As examples of different merger histories which can produce bright SMGs, we plot in the left panels of Fig. 4.1 and of Fig. 4.2, galaxy merger trees for three different present-day galaxies, covering a range in present stellar mass from $\sim 3\times 10^{10}h^{-1}M_{\odot}$ to $\sim 10^{12}h^{-1}M_{\odot}$. For these examples we require that a SMG phase appears in the main progenitor branch (leftmost branch). We define the main progenitor branch as follows: starting at the final time, we step back in time (up the tree), following the branch of the most massive progenitor each time there is a merger. (Note that the main progenitor need not be the most massive progenitor at all times.) We indicate with a red circle when a galaxy at a given redshift is a bright SMG and with a blue circle otherwise. In these selected examples, more massive present-day galaxies can show more than one bright SMG episode.

In the right panels of Fig. 4.1 and of Fig. 4.2 we show the evolution of the 850 μm flux for the main progenitor galaxy (leftmost branch) in the trees. Following each merger that triggers a burst, there is a rapid increase in the 850 μm flux, followed by a slow decline in flux. The time interval when the flux is above 5 mJy is different in the different examples. In the same panels, we also plot the evolution of the stellar, gas and dark matter halo masses for the main progenitor, together with the mass formed in ongoing bursts. In the upper sub-panels, we plot the evolution of the bulge to total stellar mass ratio B/T as an indication of the morphology of the galaxy (and we also indicate when the central galaxy became a satellite galaxy, if that happens).

In the first example shown (Fig. 4.1), the central galaxy becomes a satellite galaxy at $z = 2.3$ (note the large increase in the host halo mass due to the merger with a more massive halo). In the second example (Fig. 4.2), the galaxy becomes a satellite at $z = 0.3$ and in the third example (Fig. 4.2), the galaxy is always the central galaxy in its halo. As mentioned previously, satellite galaxies cannot accrete any more gas by cooling, so star formation can only continue until the pre-existing cold gas reservoir is used up, which limits the increase in stellar mass once a galaxy becomes a satellite (blue line).

We also indicate in the right-hand panels when the galaxy undergoes a merger with another galaxy. If there is a burst (see Section 2.3) the gas from the merging pair is used up to produce a burst of star formation (which raises the 850 μm flux). Note that the galaxy mergers at $z = 2.7$ and $z = 2.5$ in the first and second examples, respectively,

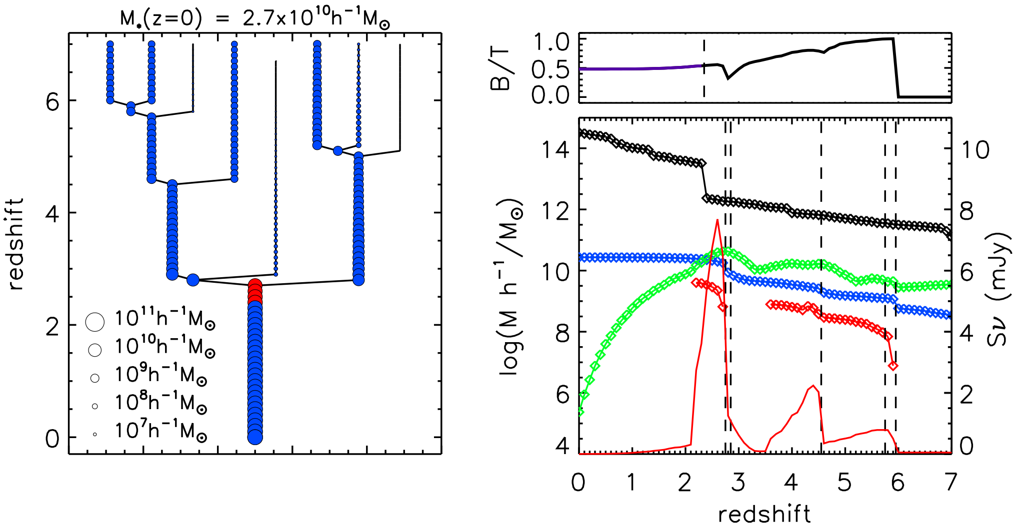

Figure 4.1: Left panel: galaxy merger tree for a galaxy with SMG progenitor. The size of the symbol is proportional to the stellar mass as indicated by the key. The red circles indicate galaxies in a bright SMG phase (when the 850 μm flux exceeds 5 mJy). Right panel: evolution with redshift of the galaxy on the main progenitor branch. Top subpanels: evolution of the bulge-to-total stellar mass ratio (B/T). The dashed vertical line indicates the redshift at which the central galaxy (black line) becomes a satellite galaxy (blue line) after a halo merger. Lower subpanels: the symbols show the evolution of the stellar mass (blue), cold gas mass (green), dark matter host halo mass (black) and the mass formed in ongoing bursts (red) in units shown on the left axis. The red line shows the evolution of the 850 μm flux, in units shown on the right axis, and the dashed vertical black lines indicate the redshift at which the galaxy undergoes a merger with another galaxy (see left panel). The stellar mass of the galaxy at $z = 0$ is $M_* = 2.7\times10^{10}h^{-1}M_\odot$.

are minor mergers since the morphology of the resulting galaxy is a mix of bulge+disk ($B/T \sim 0.5$ in both cases). The galaxy mergers at $z = 5.9$ and $z = 2.1$ in the first and second examples, respectively, are major mergers since the resulting galaxy is a pure bulge galaxy with $B/T = 1$. Since more hot gas can be accreted by cooling onto central galaxies, more star formation takes place, changing again the morphology of the galaxy.

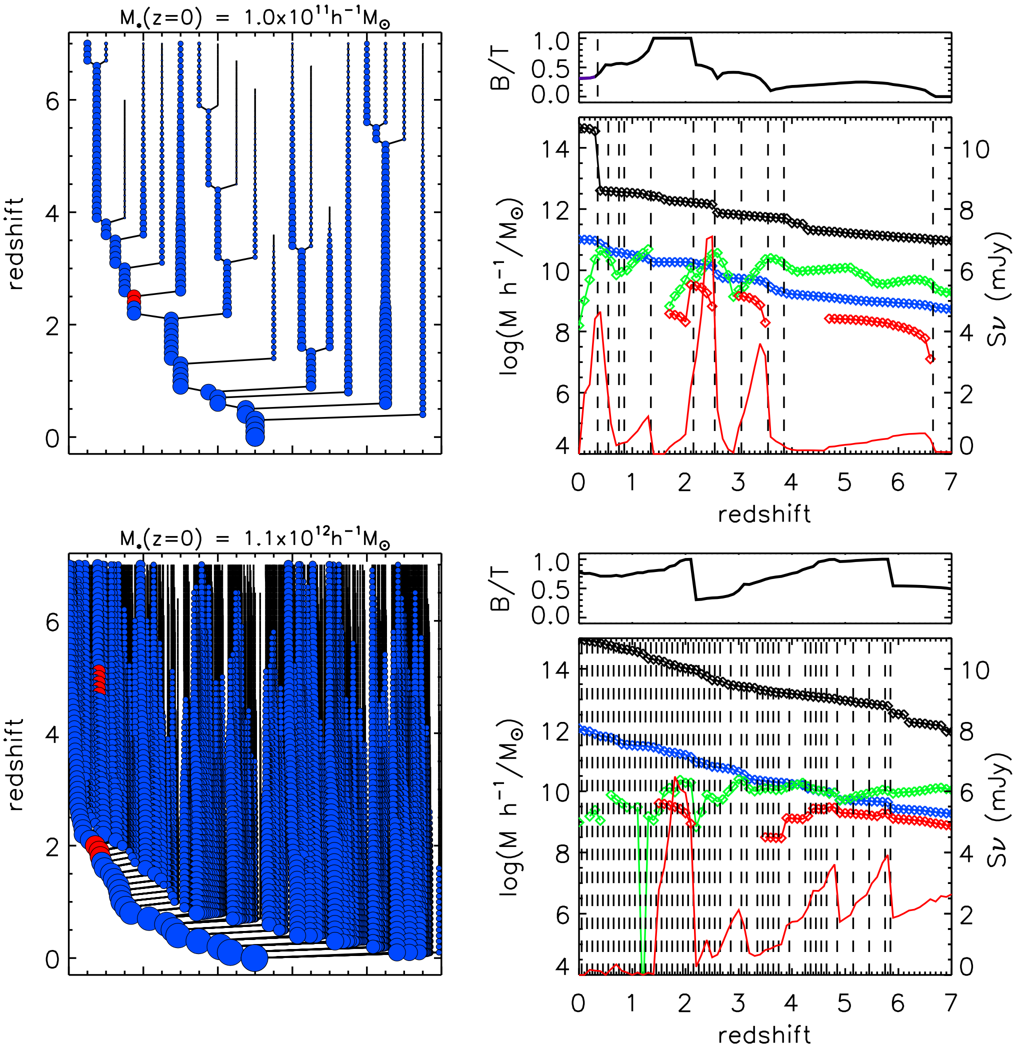

Figure 4.2: Similar to Fig. 4.1, but the stellar masses of the galaxies at $z = 0$ are $M_* = 1.0 \times 10^{11} h^{-1} M_\odot$ (top) and $M_* = 1.1 \times 10^{12} h^{-1} M_\odot$.

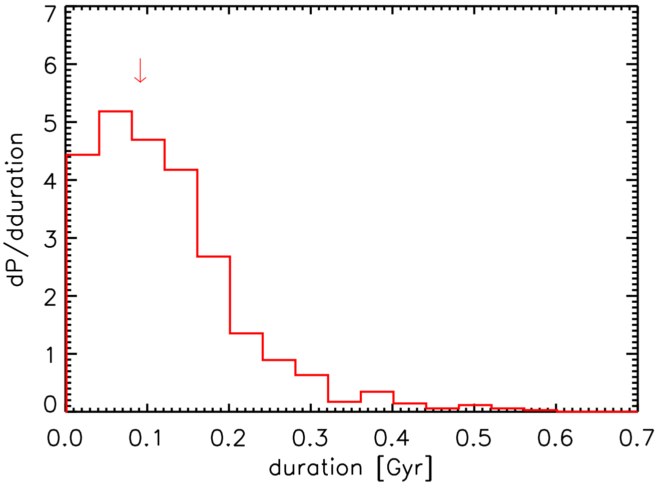

Figure 4.3: Duration of the bright SMG phase, i.e. the time for which the flux is $S_\nu(850\ \mu\mathrm{m}) > 5$ mJy. The median of the distribution is 0.09Gyr (indicated by the arrow). The distribution is normalised to unit area.

4.3 Properties of SMGs at Different Redshifts

Having identified all the SMGs in the model, we can study the evolution of some of their properties. In the model, the redshift distribution of SMGs shows a peak at $z \sim 2$ (Baugh et al. 2005, see also Swinbank et al. 2008) similar to that observed by Chapman et al. (2004). We define two types of submillimetre galaxies according to a threshold in 850 μm flux. We define a galaxy as a *bright* SMG when its flux exceeds 5 mJy and as a *faint* SMG when its flux exceeds 1 mJy. Most currently observed SMGs have fluxes around 5 mJy or brighter (bright SMGs here). We present the faint SMGs as a comparison sample.

4.3.1 Duration of SMG Phase

We define the duration of the bright SMG phase to be the time when the flux of a galaxy is above 5 mJy. This time is typically smaller than the duration of the star formation burst which triggered the flux increase (see examples in Fig. 4.1 and in Fig. 4.2). In Fig. 4.3 we plot the distribution of SMG phase durations all of the bright SMG phases identified in the redshift range $z = 2 - 3$. The durations range from < 0.04 Gyr to 1 Gyr. The median of the distribution is 0.09 Gyr. For comparison, the median duration of the star formation bursts that triggered the bright SMG phase is 0.66 Gyr.

4.3.2 Stellar and Halo Masses

In the top left panel of Fig. 4.4, we plot the median stellar mass and host halo mass for the bright SMGs as a function of redshift. For the bright SMGs sample at redshift $z = 1.5$, the stellar and parent halo mass are respectively four and three times more massive than the bright SMGs identified at redshift $z = 6$. For comparison, we show also the results for faint SMGs selected with $S_\nu > 1$ mJy in the bottom left panel. Faint SMGs identified at redshift $z = 6$ have typically 1/4 of the stellar mass of the bright SMGs identified at the same redshift, and they live in haloes with half the mass. At redshift $z = 2.4$ they have typically half the stellar mass and they live in haloes with half the mass of those which host the bright SMGs.

4.3.3 Morphology

In a similar way, we can study the morphologies of SMGs identified at different redshifts. As mentioned, a major merger produces a pure bulge galaxy, whereas a minor merger produces a disk+bulge galaxy (if the main merging galaxy had a disk at the moment of merging). In the top left panel of Fig. 4.5, we plot the median of the bulge-to-total stellar mass ratio B/T (where B/T=0 indicates a pure disk galaxy and B/T=1 indicates a pure bulge galaxy) for the bright SMGs. At high redshift, bright SMGs have intermediate values of B/T ($B/T \sim 0.4$), but the typical B/T increases as we get closer to the median redshift of bright SMGs ($z \sim 2$).

For comparison, we show also the results for faint SMGs selected with $S_\nu > 1$ mJy in the bottom left panel of Fig. 4.5. These faint SMGs typically have intermediate values of B/T at all redshifts and the samples at higher redshifts have higher values of B/T compared to lower redshift (showing an opposite trend compared to bright SMGs).

4.3.4 SMG Triggering, Minor or Major Mergers?

As we discussed before, most (> 99%) of bright SMGs in our model are starbursts triggered by galaxy mergers. Bursts happen in all major mergers and in some minor mergers (see Section 2.3). Which type of merger dominates the triggering of SMGs? We answer this question in Fig. 4.6, where we plot the distribution of stellar masses of $z = 0$ descendants of bright SMGs at $z > 1$ separated into those triggered by minor mergers (blue) and produced by major mergers (red). We find that 71% are produced by minor mergers, 29% are produced by major mergers, and 0.7% are quiescent galaxies (i.e. not ongoing

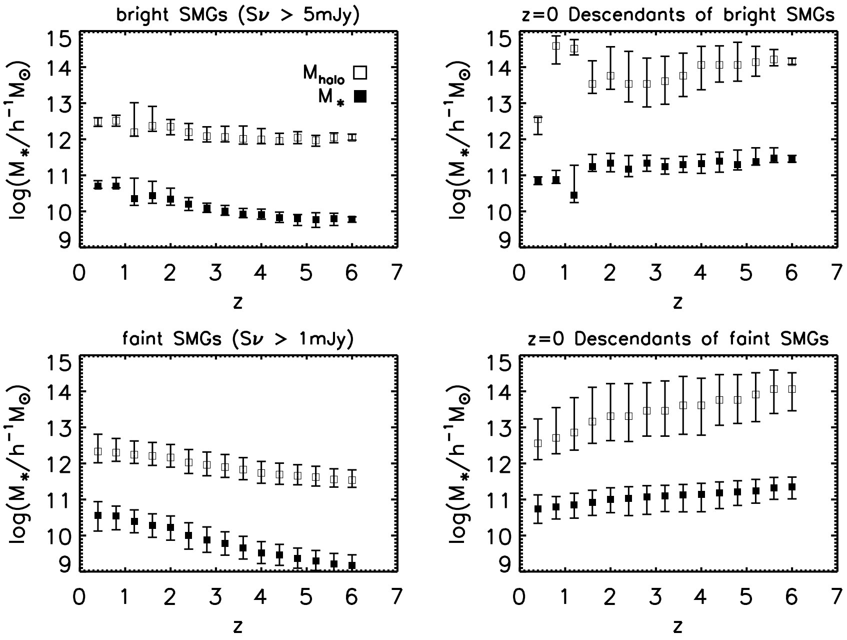

Figure 4.4: Left panels: The median stellar and host halo masses for SMGs selected at different redshifts. Right panels: median stellar and host halo masses of the $z = 0$ descendants of SMGs identified at different redshifts. Top panels: bright SMGs selected with $S_\nu > 5$ mJy. Bottom panels: faint SMGs selected with $S_\nu > 1$ mJy. Filled squares show stellar masses and open squares show halo masses. Errorbars indicate the 10% and 90% percentiles.

starbursts). Major mergers dominate the distribution for the highest present-day stellar masses, but minor mergers dominate at lower masses. These proportions are qualitatively consistent with the result shown in (Fig. 4.5) that the bulge-to-total stellar mass ratios B/T of SMGs are typically intermediate between pure disk and pure bulge.

4.4 Properties of SMG Descendants

Most of the SMGs detected in flux-limited surveys lie at redshit $z = 1 - 4$. SMGs at redshift $z < 1$ account for only a small fraction of the population in a flux limited sample due to the small volume at low redshift. Model SMGs at low redshifts $z < 1$ are mostly objects with modest star formation rates which have bright sub-mm fluxes simply due to their proximity to us, rather than because an intense episode of star formation has taken place. In this section, we will focus on the descendants of the *high-z* SMGs, which we define to be those with $z > 1$, and will investigate the distribution in stellar and parent

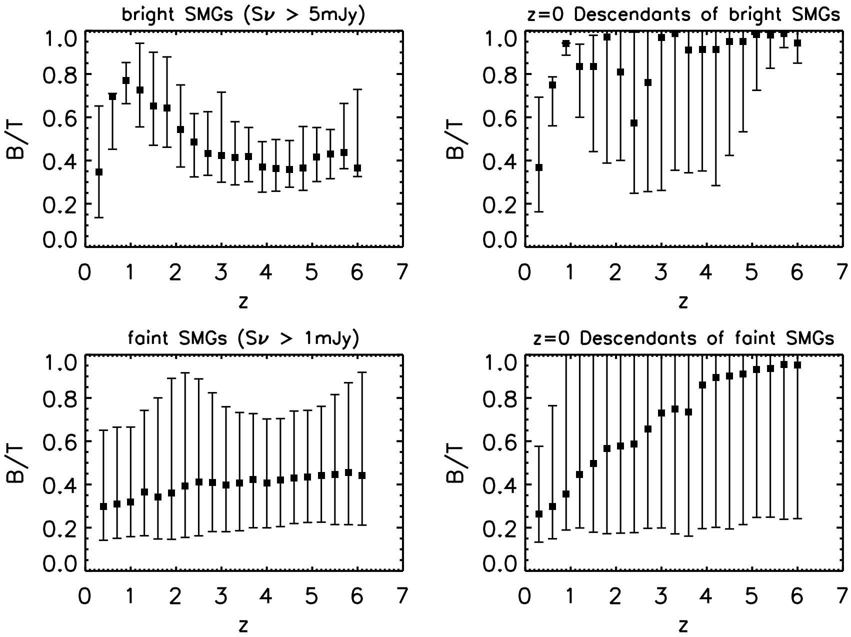

Figure 4.5: Left panels: The predicted distribution of bulge-to-total stellar mass ratio B/T for SMGs selected at different redshifts. Right panels: the B/T distribution of the $z = 0$ descendants from SMGs identified at different redshifts. Top panels: bright SMGs selected with $S_\nu > 5$ mJy. Bottom panel: faint SMGs selected with $S_\nu > 1$ mJy. The filled-squares show the median of the distribution at each redshift and the errorbars indicate the 10% and 90% percentiles.

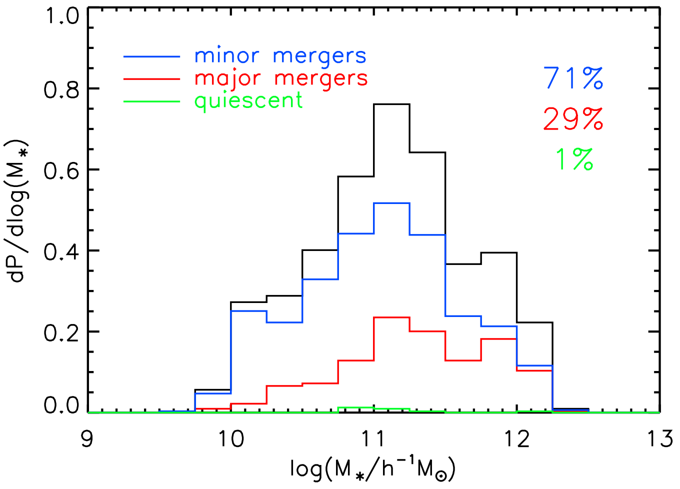

Figure 4.6: Number distribution of $z > 1$ bright ($S_\nu > 5$ mJy) SMGs produced by major mergers (red), minor mergers (blue) and quiescent galaxies (green). The total distribution is normalised to have unit area.

halo mass, morphology and central/satellite galaxy classification.

4.4.1 Stellar and Host Halo Masses of SMG Descendants

What are the masses of the present-day descendants of SMGs seen at different redshifts? In the right panels of Fig. 4.4, we plot the stellar and host halo masses of the $z = 0$ descendants of the SMG samples selected at different redshifts. We find that bright SMGs identified at higher redshift typically evolve into somewhat more massive galaxies hosted in more massive haloes compared to bright SMGs found at lower redshifts. The model predicts that bright SMGs at the median of the observed redshift distribution ($z \sim 2.4$) increase their stellar mass by one order of magnitude to redshift $z = 0$ (from $\sim 3 \times 10^{10} h^{-1} M_{\odot}$ to $\sim 3 \times 10^{11} h^{-1} M_{\odot}$).

The top left panel of Fig. 4.7 shows the stellar mass of the descendants of all bright SMGs with $z > 1$. We separate the galaxies into bulge-dominated ($B/T > 0.5$) and disk-dominated ($B/T < 0.5$) samples. The number of bulge-dominated descendants is more than double the number of disk-dominated descendants. Also, the bulge-dominated descendant galaxies have a higher median mass. For all the descendants, the median stellar mass is $1.8 \times 10^{11} h^{-1} M_{\odot}$. The distribution of host dark matter halo masses of the $z = 0$ descendants shown in the top right panel of Fig. 4.7 shows a fairly flat distribution in halo mass for disk-dominated descendants. For bulge-dominated descendants, the distribution shows a preference for higher masses. The median dark matter halo mass for the $z = 0$ descendants of all bright $z > 1$ SMGs is $5.8 \times 10^{13} h^{-1} M_{\odot}$. For comparison, we also show the results for the faint SMGs selected with $S_{\nu} > 1$ mJy. The median stellar and dark matter halo masses of the descendants are slightly smaller than for the bright SMGs, and their distribution is wider. In this case, the proportions of disk-dominated and bulge-dominated descendants are similar.

In Fig. 4.8, we repeat the same analysis but separate the descendants into central and satellite galaxies in the halo where they live at present-day. We can see that nearly 80% of the $z = 0$ descendants of bright SMGs are central galaxies. We note that satellite galaxies that are descendants of bright SMGs are found only in the more massive haloes today.

4.4.2 Morphology of Descendants of SMGs Compared to Other Similar Mass Galaxies

The top right panel of Fig. 4.5 shows us that bright SMGs identified at different redshifts typically evolve to bulge-dominated galaxies at redshift $z = 0$. According to the bottom right panel, the descendants of faint SMGs have intermediate values of B/T for lower and intermediate redshifts. Only the higher redshift samples evolve into bulge-dominated systems at present-day.

Fig. 4.7 shows that the majority of the descendants of both bright and faint $z > 1$ SMGs are bulge-dominated systems. The top panel of Fig. 4.9 shows the probability distribution of B/T for the descendant galaxies of bright SMGs (in black). 75% of the descendants are bulge-dominated galaxies ($B/T > 0.5$) and 25% are disk-dominated galaxies ($B/T < 0.5$). Among these, 55% of the descendants are pure bulge systems ($B/T > 0.9$) and only 5% are pure disk systems ($B/T < 0.1$). The bottom panel shows the probability distribution of B/T for the descendants of faint SMGs (in black). In this case, 60% of the descendants are bulge-dominated systems.

But, are these results a special characteristic of SMG descendants, or are these morphologies simply typical of $z = 0$ galaxies with similar stellar mass? To answer this, we select comparison samples (for bright and faint SMGs) composed of galaxies at $z = 0$ with a similar stellar mass distribution to the bright and faint SMG descendants. These samples overlap the descendant samples, particularly for the faint SMGs. In Fig. 4.9, we plot in black the probability distribution of B/T of the SMG descendants, and in red of the comparison samples.

The descendant and comparison samples for bright and faint SMGs show very similar distributions. Despite the fact that most of the descendants of bright SMGs are bulge-dominated galaxies, their morphologies are not significantly different from other $z = 0$ galaxies with similar stellar masses.

4.5 SMG Progenitors of Present-Day Galaxies

In the previous section we studied the properties of the descendants of SMGs. We identified SMGs in the model at a particular redshift and we found their $z = 0$ descendants. In this section we want to study the connection of SMGs to present day galaxies from the opposite perspective: given a galaxy today with a particular mass, what is the probability that this galaxy has SMG progenitors? And for dark matter haloes at present-day, what

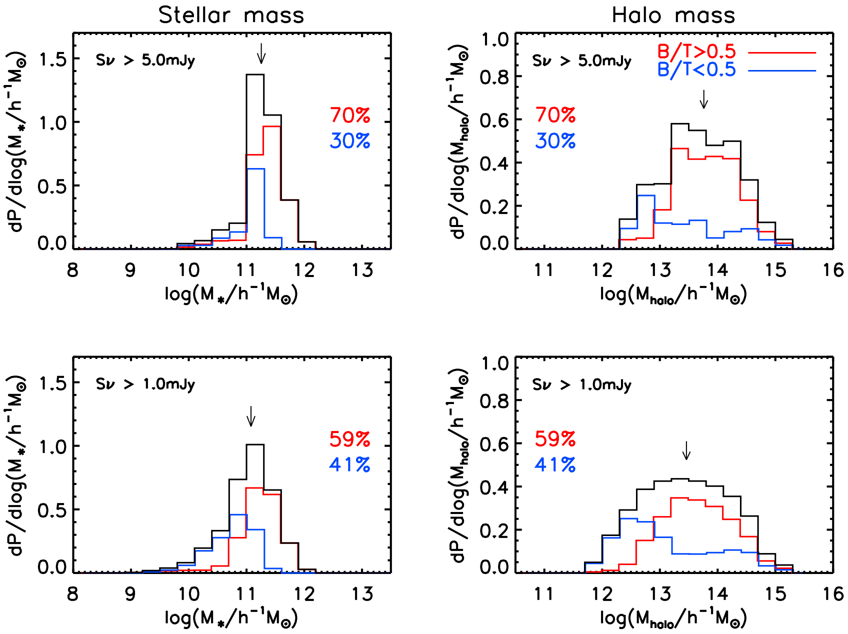

Figure 4.7: Stellar mass distribution (left panels) and host halo mass distribution (right panels) for descendants of bright SMGs ($S_\nu > 5$ mJy, top panels) and for descendants of faint SMGs ($S_\nu > 1$ mJy, bottom panels). The red distribution is for bulge-dominated ($B/T > 0.5$) descendant galaxies and the blue for disk-dominated ($B/T < 0.5$) descendant galaxies. Black lines represent the sum of the red and blue distributions. The mass distributions are normalised to unit area for the full sample.

is the probability that a progenitor halo hosted at least one SMG? Fig. 4.10 answers these questions, for both bright and faint SMGs at $z > 1$ (top and bottom panels respectively). The left panels show this probability as a function of stellar mass, and the right panels as a function of halo mass. We see that the probability that a galaxy or halo had one or more SMG progenitors at $z > 1$ brighter than a given 850μm flux increases with increasing mass. From the top left panel, we see that present-day galaxies have a probability of 10% to be descendants of bright SMGs ($S_\nu > 5$ mJy) at a stellar mass of $10^{11}h^{-1}M_\odot$, and 50% at a mass of $7 \times 10^{11}h^{-1}M_\odot$. For comparison, we see from the lower-left panel that 50% of galaxies are descendants of faint SMGs ($S_\nu > 1$ mJy) for stellar masses of $2 \times 10^{10}h^{-1}M_\odot$. We find in both cases (bright and faint SMGs) that at intermediate masses ($\sim 10^{10} - 10^{11}h^{-1}M_\odot$) there are more disk-dominated descendants of SMGs than bulge-dominated descendants. For haloes, we see from the right panels that more than 50% of the haloes with masses larger than $10^{14}h^{-1}M_\odot$ are predicted to have bright SMG

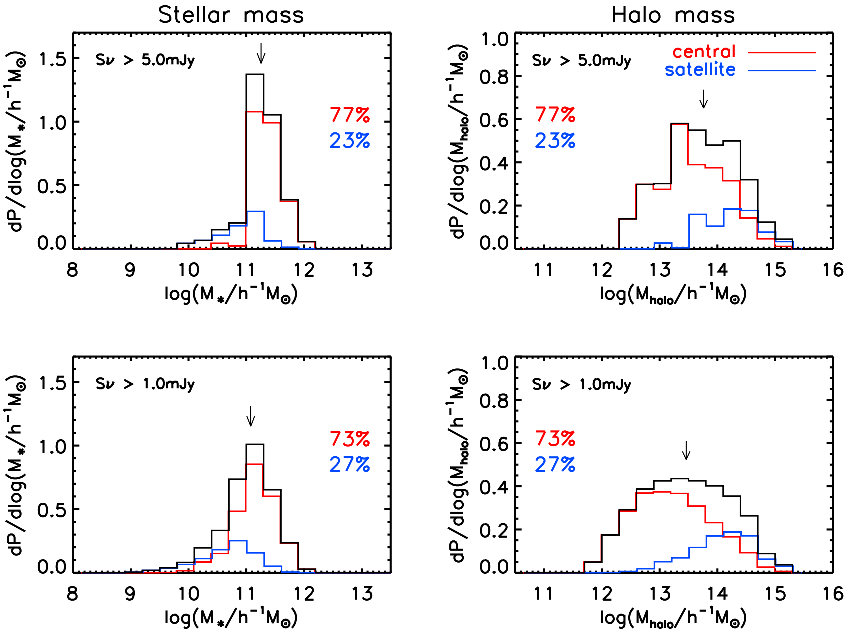

Figure 4.8: Similar to Fig. 4.7 but separating the descendant galaxies into central (red) and satellite (blue) galaxies.

progenitors, and 50% of the haloes with masses larger than $2 \times 10^{12} h^{-1} M_{\odot}$ are predicted to have faint SMG progenitors.

4.6 Contribution of SMGs to the Present-Day Stellar Mass

We saw in the previous section that most massive galaxies today are predicted to be descendants of SMGs. We found also in Section 4.1 that the median of the SMG phase duration is 0.09 Gyr. Since a high star formation rate is inferred in this phase, we want to know what is the contribution to the present-day stellar mass actually produced in the SMG phase.

In Fig. 4.11 we plot the evolution of the cosmic star formation rate density. We show both the total, as well as the contributions from bursts and quiescent disks, and the contributions from galaxies in the bright ($S_{\nu} > 5$ mJy) or faint ($S_{\nu} > 1$ mJy) SMG phase. We see that the contribution to star formation from quiescent disks dominates at redshit $z \lesssim 3.5$, but bursts dominate at higher redshifts. At redshifts $z = 2 - 4$, around 1% of the cosmic star formation is produced by bursts in bright SMGs, and around 10% is produced by bursts in faint SMGs. The quiescent star formation rate is typically one order of magnitude smaller than burst star formation rate for bright SMGs at high redshift. For

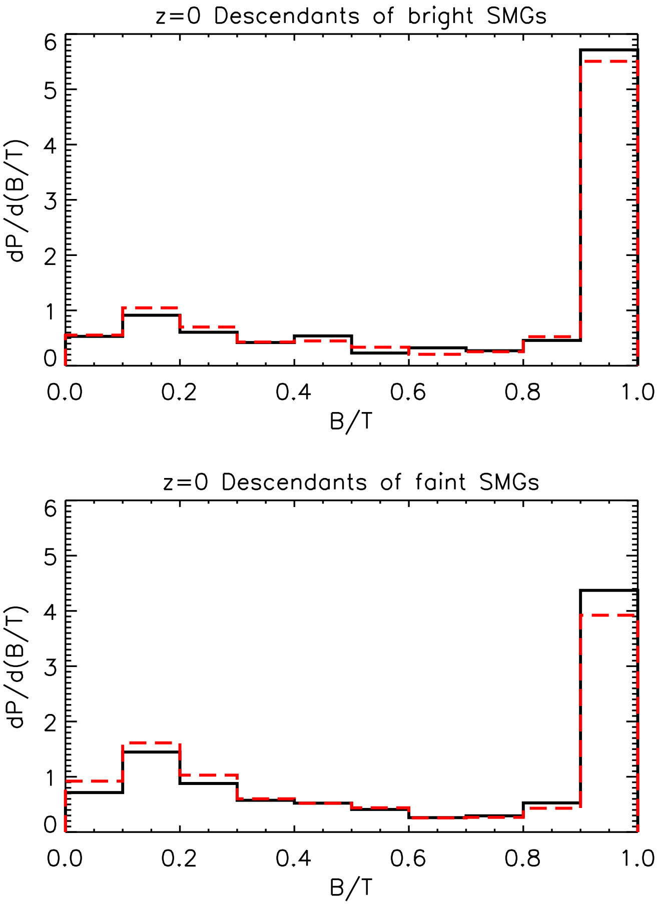

Figure 4.9: Probability distribution of the bulge-to-total stellar mass ratio (B/T) for descendants of bright SMGs (top panel, black) and for descendants of faint SMGs (bottom panel, black). Dashed red lines represent the comparison samples formed by galaxies at $z = 0$ with a similar stellar mass distribution to the bright and faint SMG descendants.

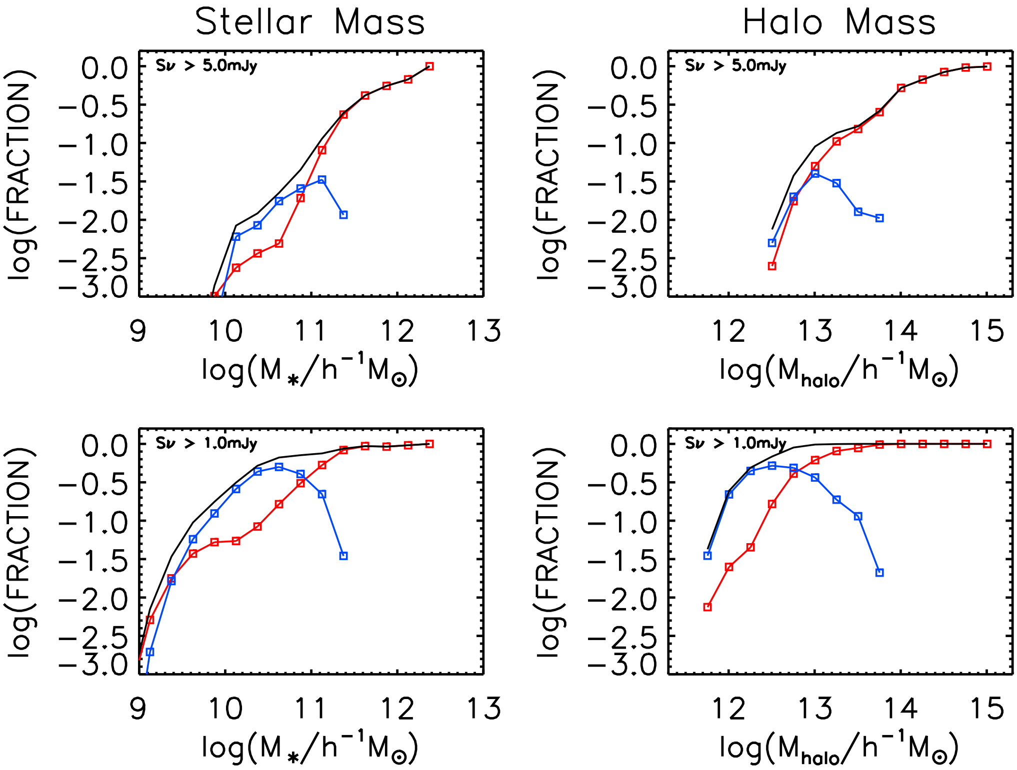

Figure 4.10: Left panels: fraction of present-day galaxies by stellar mass that are predicted to be descendants of bright SMGs ($S_\nu > 5$ mJy, top panel) and descendants of faint SMGs ($S_\nu > 1$ mJy, bottom panel). Right panels: fraction of present-day halos by mass that are predicted to have halo progenitors that hosted at least one bright SMG (top panel) or at least one faint SMG (bottom panel). These are computed for $z > 1$ SMG progenitors. Left panels: bulge-dominated ($B/T > 0.5$) descendants in red and disk-dominated ($B/T < 0.5$) descendants in blue. Right panels: bulge-dominated ($B/T > 0.5$) halo central galaxy in red and disk-dominated ($B/T > 0.5$) halo central galaxy in blue. The black line represents all of the SMG descendants (the sum of the blue and red lines).

faint SMGs, the burst star formation rate dominates at redshift $z \gtrsim 2$, but quiescent star formation becomes more important at lower redshift. At low enough redshift ($z \ll 1$), star formation at any level in a galaxy is sufficient to produce a sub-mm flux above the bright or faint thresholds, which is why the quiescent and burst contributions from bright and faint SMGs converge on the total quiescent and burst contributions at $z = 0$.

In the top panel of Fig. 4.12 we plot the comoving stellar mass density as a function of redshift, both the total, and the contributions to this from star formation in the quiescent and burst modes, and the contributions from star formation during bright and faint SMG phases at $z > 1$. Note that the stellar mass densities we plot are the values after allowing for recycling of gas to the interestellar medium from dying stars, using the recycled fractions for the two IMFs given in Sec. 2.5.2. The lower panel shows the different contributions to the stellar mass density plotted as fractions of the total stellar mass density at that redshift. We see from this that bursts of star formation contribute a total of 5% to the present-day stellar mass density. Star formation (burst+quiescent) in the faint SMG phase at $z > 1$ contributes 2% to the present-day stellar mass density, while the bright SMG phase at $z > 1$ contributes only 0.06%.

Finally, we examine in more detail the contribution of the mass produced by all bursts and by bursts in the bright SMG phase as a function of stellar mass. In Fig. 4.13 we plot the fraction of the present stellar mass (allowing for recycling) produced by all bursts in all galaxies (red) and only in descendants of bright SMGs (black). We also plot the contribution to the stellar mass produced by bursts in the bright SMG phase to all present-day galaxies (green) and only to the descendants of bright SMGs (blue). We see from this plot that on average bursts contribute 3-8% to the present-day stellar masses of galaxies over the whole range $\sim 10^9 - 10^{12} h^{-1} M_{\odot}$. If we look only at galaxies which are descendants of bright SMGs, then we find an average fraction that is the same at the highest stellar masses, but increases with decreasing mass, reaching 60% for the least massive descendants ($\sim 5 \times 10^9 h^{-1} M_{\odot}$). However, bursts during the bright SMG phase at $z > 1$ contribute less than this. For descendants of bright SMGs, the fraction varies from 30-40% for the least massive descendants ($\sim 5 \times 10^9 h^{-1} M_{\odot}$), to 0.2% for the most massive ones ($\sim 10^{12} h^{-1} M_{\odot}$). The average contribution to the current stellar mass of all galaxies from bursts in the bright SMG phase increases with stellar mass, but is always below 0.3%. For a present-day stellar mass of $1.8 \times 10^{11} h^{-1} M_{\odot}$, which is the median descendant mass of bright SMGs (see Sec. 4.4.1), the contribution of bursts in the bright SMG phase to the present stellar mass is only 1% even for descendants of bright SMGs,

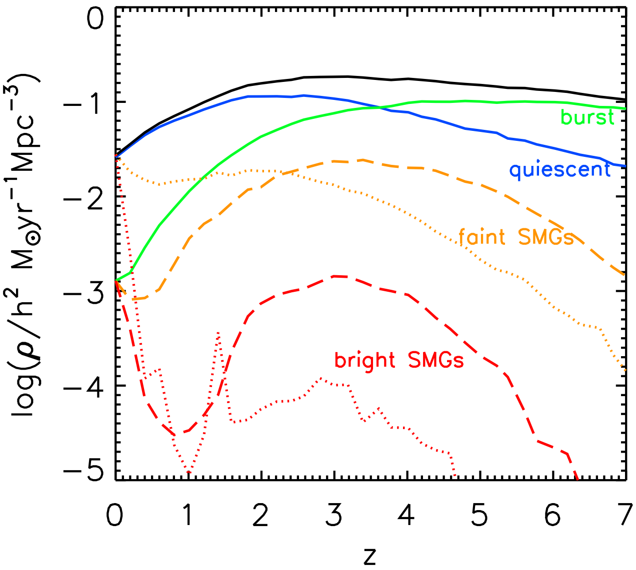

Figure 4.11: Evolution of the cosmic star formation rate per unit comoving volume. The black line shows the total total star formation rate, while the green and blue lines show the separate contributions from bursts and quiescent star formation respectively. The red and orange lines respectively show the star formation rate in bright and faint SMGs, for which the separate contributions from bursts and quiescent star formation are shown by dashed and dotted lines.

and falls to only 0.2% if we look at all galaxies of that mass.

4.7 The robustness of the model predictions to selected parameter changes

In an earlier chapter we investigated the impact on the predictions of changing the strengths of various processes in the model. We found that by reducing the strength of SN feedback and adjusting the star formation timescale we can improve the size-luminosity relation. These changes not only have an impact on the sizes of galaxies but also an impact on other model predictions, e.g. the luminosity function, which does not agree with observational estimates as well as the fiducial model.

In this section we test the robustness of our predictions for the properties of SMGs and their descendants to varying a subset of the model parameters. We investigate the

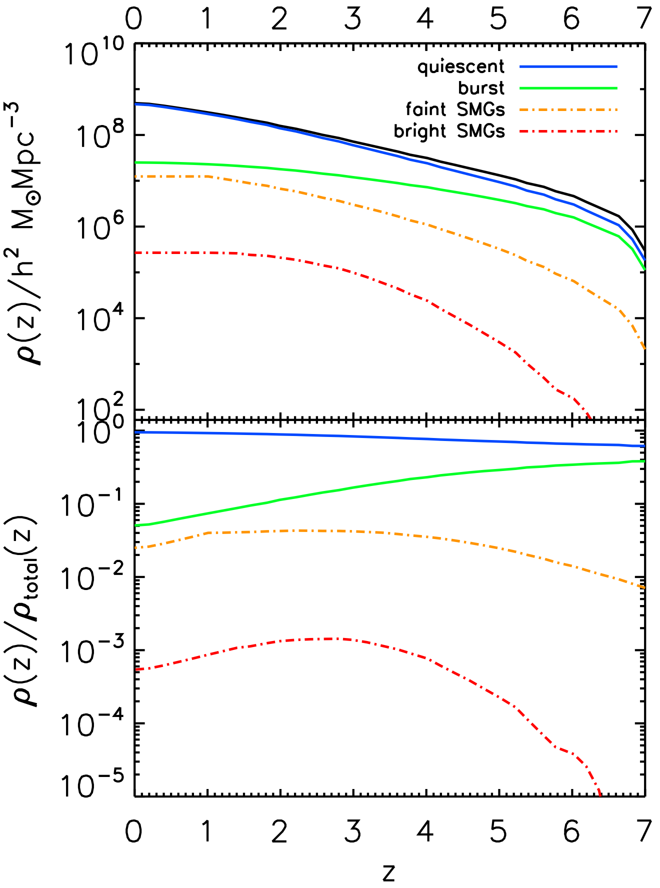

Figure 4.12: Top panel: comoving stellar mass density as a function of redshift. The black line shows the total, while the blue and green lines show the contributions to this from quiescent and burst star formation respectively, and the red and orange lines show the contributions from star formation in bright or faint SMG phases. For the SMGs, we only show the contributions from SMG phases at $z > 1$. Bottom panel: similar to the top, except that the different contributions to the stellar mass density are plotted as fractions of the total stellar mass density at that redshift.

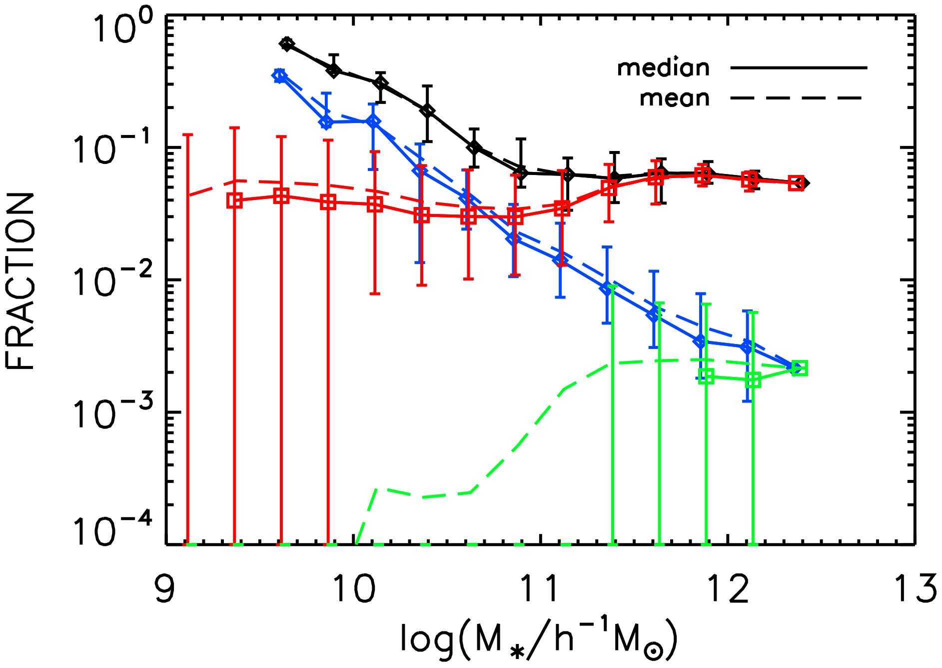

Figure 4.13: Fraction of the stellar mass produced in bursts as a function of present-day stellar mass. The red lines show the average fraction produced by all bursts in all galaxies, while the black lines show the fraction produced by all bursts in descendants of bright SMGs only. The green lines show the fraction produced by bursts in the bright SMG phase for all galaxies, and the blue lines show the fraction produced by bursts during an SMG phase in descendants of bright SMGs only. Note that in this plot we only include the contribution of bright SMGs at $z > 1$. The dashed lines show the mean, and the solid lines the median, with the errorbars showing the 10% and 90% percentiles.

effect of increasing and decreasing the SN feedback (see Eq. 2.15), modifying the orbital energy of two galaxies undergoing a merger ($f_{\rm orbit}$, see Eq. 2.31) and turning on the disk instability criteria (see Eq. 2.29).

In Fig. 4.14 we show the $S_\nu(850\ \mu{\rm m})$ luminosity function at $z = 2.4$ for the fiducial model and the variations listed above. The increase of the SN feedback results in brighter sub-mm luminosities. The decrease of the SN feedback decreases the sub-mm luminosities, drastically reducing the number of bright SMGS ($\log(S_\nu/{\rm mJy}) > 0.7$). In Chapter 3 we saw that an increase or decrease of the SN feedback result in an increase or decrease of the disk sizes respectively. A larger disk produces a larger contribution to the sub-mm flux.

Fig. 4.14 shows that there is not a significant impact on the luminosity function from changing the $f_{\rm orbit}$ parameter. This is expected since this parameter mainly affects the size of stellar spheroids. Finally, turning on the disk instability criteria can trigger more additional bursts increasing the sub-mm emission from galaxies.

In this example we found that the sub-mm luminosity function can be affected by changing the parameters, but the impact on the properties of the SMGs and their descendants is our main concern here.

In Fig. 4.15 we show the median stellar mass of bright SMGs and their $z = 0$ descendants for the fiducial model and the variants. The stellar masses of bright SMGs and those of their descendants are insensitive to the changes made to the selected parameters. Only in the case of turning on the disk instability criteria is the stellar mass reduced to around half of the value predicted in the fiducial model. The descendants of bright SMGs show only a significant variation with $f_{\rm orbit} = 0$ where the stellar mass doubles its value compared to the fiducial model. We note that we do not find any bright SMG in the volume considered for the scenario with increased SN feedback.

In Fig. 4.16 we repeat the same exercise for faint SMGs and their $z = 0$ descendants. The stellar mass of faint SMGs shows more variation compared to bright SMGs, particularly for the case with the disk instability criteria with $\epsilon_{\rm disk} = 1$. The median of the stellar mass of the descendants of faint SMGs only show a significant variation for $V_{\rm hot} = 600\,{\rm km\,s^{-1}}$ and for $\epsilon_{\rm disk} = 1$. All the changes are modest compared with the 10-90 percentile ranges.

The median mass of the halos which host SMGs depend little on the parameter changes as seen in Fig. 4.17 and in Fig. 4.18 for bright and faint SMGs respectively. The median mass of the halos hosting the descendants of SMGs show more variation on changing the

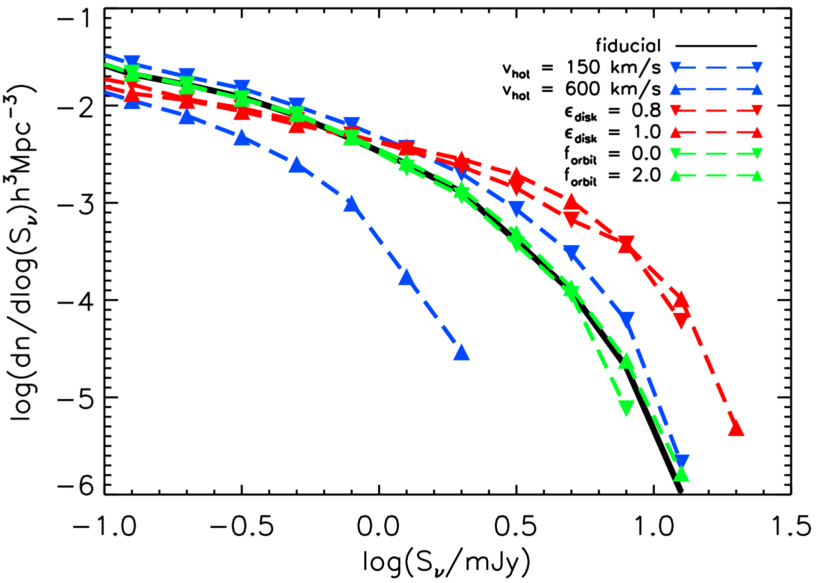

Figure 4.14: The impact on the sub-mm luminosity function at $z = 2.4$ of changing parameters in the model. Different colours correspond to different models as indicated in the label.

model parameters, specially the case with $\epsilon_{\rm disk} = 0.8$ where the mass is reduced to around 30% of the fiducial value.

We have seen that the stellar mass and halo mass are not noticeably sensitive to the choice of model parameters, unlike the case of the sub-mm luminosity function. In most cases all of the different median values fall well inside the 10-90 percentile range of the fiducial case.

4.8 Conclusions

We have investigated predictions for the properties and descendants of submillimetre galaxies (SMGs) in a theoretical model of galaxy formation in a ΛCDM universe. This model has previously been shown to reproduce the observed number counts and redshifts of SMGs, as well as a wide variety of other galaxy properties at low and high redshift.

We find that SMGs in the model are typically the progenitors of massive galaxies today, with a median stellar mass $\sim 2 \times 10^{11} h^{-1} M_{\odot}$ for the descendants of bright SMGs, having 850μm fluxes brighter than 5 mJy. The descendants of SMGs are predicted to be mainly bulge-dominated systems, but the SMG phase does not appear to play a dominant role in building the bulge, since their morphologies are similar to those of other present-

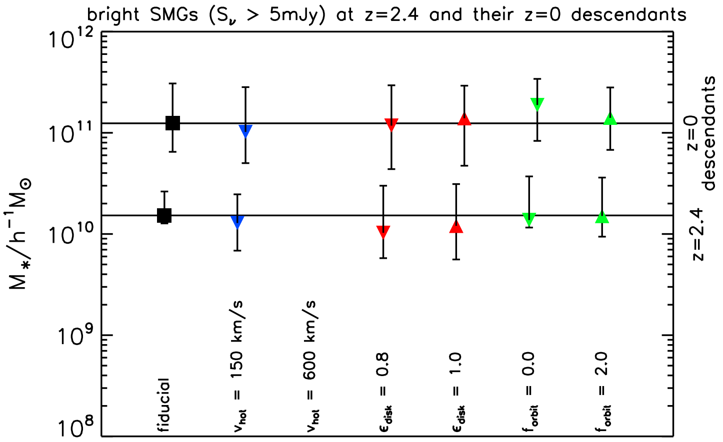

Figure 4.15: The impact on the stellar mass of $z = 2.4$ bright SMGs and their $z = 0$ descendants of varying model parameters. Different colours correspond to different models as indicated in the label. The horizontal line represent the corresponding stellar mass in the fiducial model. The bars show the 10-90 percentile range of the distributions.

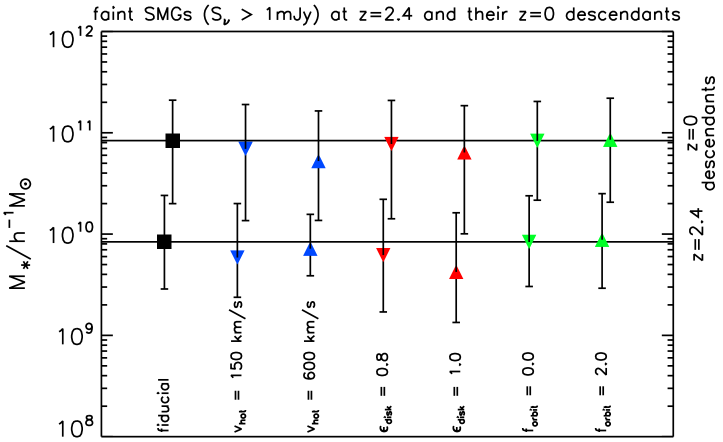

Figure 4.16: Similar to Fig. 4.15 but for faint SMGs.

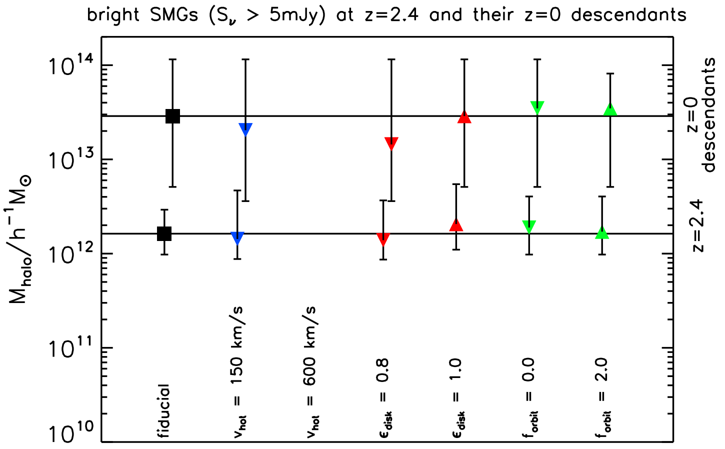

Figure 4.17: The impact on the host halo mass of $z = 2.4$ bright SMGs and on the hosting halo mass of the $z = 0$ descendants of varying model parameters. Different colours correspond to different models as indicated in the label. The horizontal line represent the corresponding halo mass in the fiducial model. The bars show the 10-90 percentile range of the distributions.

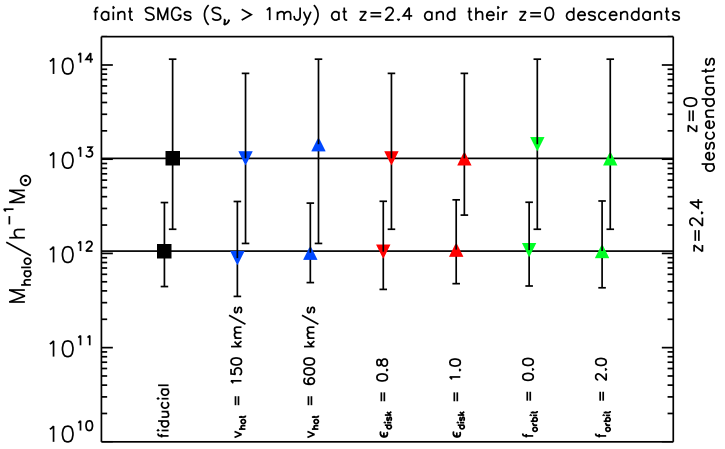

Figure 4.18: Similar to Fig. 4.17 but for faint SMGs.

day galaxies with similar stellar masses. The descendants of SMGs are predicted to live in the most massive haloes today. Looking at the mass distribution of present-day galaxies, the most massive galaxies are predicted to be descendants of SMGs, and the most massive haloes are predicted have hosted SMGs in their progenitors.

For the descendants of bright SMGs, the contribution to the present-day stellar mass from star formation in the SMG phase is predicted to range from $\sim 30\%$ for the least massive descendants to $\sim 0.2\%$ for the most massive descendants. When we compute the contribution of SMGs to the total stellar mass density today (considering only SMGs at $z > 1$), we find that only 0.06% of the stellar density is produced by the star formation in the bright SMG phase at $z > 1$ (allowing for mass recycling).

The model predicts that SMGs are the progenitors of massive galaxies today. Most of the mass in these massive systems today is built up by galaxy mergers and the accretion of smaller systems, making the contribution of stars formed during the SMG phase typically very small.

The stellar and host halo mass of the SMGs and their descendants are predicted to be robust to changing the strength of various processes in the model. The sub-mm luminosity function is more sensitive to these changes.

Chapter 5

Descendants of Lyman-break Galaxies in the Lambda-CDM Cosmology

5.1 Introduction

The high redshift galaxy populations identified using the Lyman-break selection technique have been crucial in the development of our understanding of star formation in the young Universe. This technique is based on being able to observe a measureable Lyman discontinuity to the blue-side of the restframe spectral energy distribution at 912Å. A small amount of flux can be expected from the blue-side of the Lyman limit in a galaxy since, i) few energetic photons can be produced by stars at these wavelengths, ii) energetic photons can be absorbed by the interstellar medium and ionize neutral hydrogen, and iii) such photons can also be absorbed by intergalactic hydrogen clouds along the line of sight from the galaxy to the Earth. Galaxies identified with this technique are known as Lyman-break galaxies (hereafter LBGs, Steidel and Hamilton 1992; Steidel et al. 1996).

Ground-based observations are restricted to use the Lyman-break technique for galaxies at $z > 2.5$. For this redshift range the absorption edge, which occurs in the far-ultraviolet, is shifted to wavelengths that are not blocked by the Earth's atmosphere.

The Lyman-break technique uses multi-band photometry. By using a suitable set of filters, galaxies in a particular range of redshifts can be isolated. In Fig. 5.1 we show an example of a $z \sim 3$ LBG candidate.

The multi-band photometry is also set to minimise the contamination from background and foreground objects. LBGs are selected to be red in the shorter wavelength colour, due to the presence of the beak, and blue in the longer wavelength colour, to show they

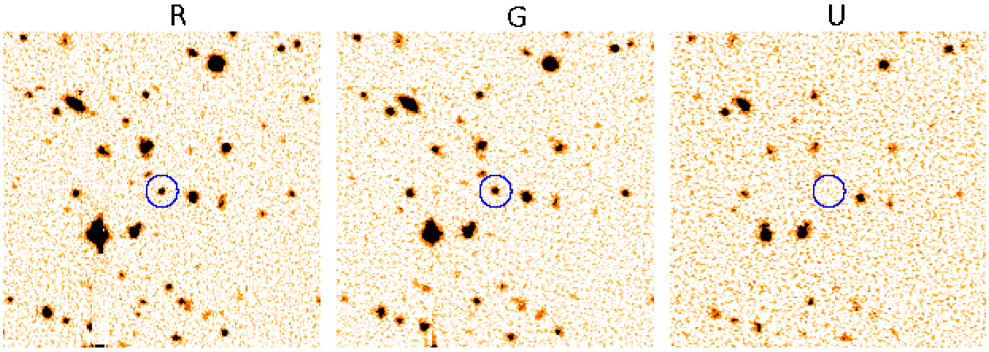

Figure 5.1: Illustration example of a candidate Lyman-break galaxy, taken with the 200-inch Hale Telescope at the Palomar Observatory in California. The images were taken through red (R), green (G), and ultraviolet (U) filters, suitable to detect LBGs at $z = 2.6 - 3.4$. The object at the center of the circle is clearly present in both the R and the G image, but disappears in the U image. Taken from C. Steidel web page, http://www.astro.caltech.edu/∼ccs/.

are star-forming galaxies. When dust effects are important, the extinction corrections required to derive star formation rates for LBGs from their rest-frame ultraviolet (UV) can be large and unreliable. This is a potential source of confusion in identifying or missing galaxies. (Adelberger and Steidel, 2000).

The analysis in this chapter is based on the Baugh et al. (2005) version of the `GALFORM` semi-analytical model.

5.2 Lyman-break Galaxies Selection

5.2.1 UV Luminosity Function: Selecting Lyman-break Galaxies.

The observational selection criteria typically used to identify LBGs at a particular redshift basically consist of applying a suitable multi-band photometry.

Since in the model we can predict the galaxy population at any desired redshift by construction, we will use the UV luminosity as a selection criteria to identify LBGs. We focus our attention on two redshifts, being the approximate extremes of the range covered by current LBGs studies (Steidel et al., 2003; Bouwens et al., 2007).

Baugh et al. (2005) presented predictions for the rest-frame UV luminosity function at $z = 3$. Here we extend their results, adding new observational data, to $z = 6$. In Fig. 5.2 we show the predicted rest-frame $\lambda = 1500$Å luminosity function at $z = 3$ and $z = 6$ including dust extinction. The model matches the observed data at $z = 3$. The

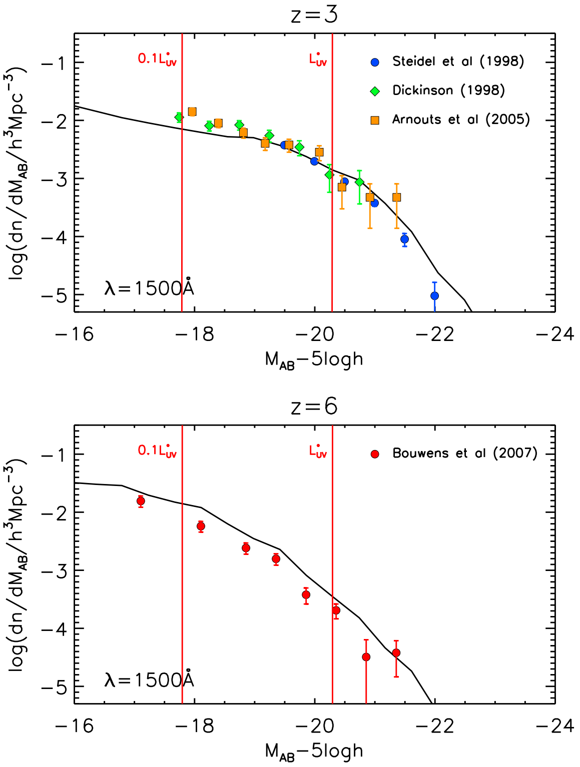

Figure 5.2: The luminosity function in the rest-frame UV at $z = 3$ (top panel) and at $z = 6$ (bottom panel). The symbols with error bars show the observational estimates taken from the sources given in the legend. The predicted luminosity functions include dust extinction. The vertical red lines indicate the position of L^*_{UV} and $0.1L^*_{UV}$ (defined at $z = 3$) used to identify faint and bright LBGs.

luminosity function predicted at $z = 6$ is around twice the observed values. Following the common practice in observational studies, we define a characteristic luminosity L^*_{UV}. We define a galaxy as a bright LBG if the UV luminosity is $L_{UV} > L^*_{UV}$ and as a faint LBG if its UV luminosity is $L_{UV} > 0.1L^*_{UV}$ (which includes bright LBGs). We apply this selection for both redshifts. Note that L^*_{UV} in both cases is the characteristic luminosity at $z \approx 3$ found by Steidel et al. (1999b) (corresponding to $M^*_{UV} = -20.3 + 5\log h$ in our cosmology). In Fig. 5.2 we also show where the $0.1L^*_{UV}$ and L^*_{UV} limits lie in the diagram.

The characteristic luminosity $L^*_{UV,z=6}$ at $z = 6$ ($M^*_{UV,z=6} = -19.47 + 5\log h$ in our cosmology, Bouwens et al. 2007) is about a magnitude fainter than the L^*_{UV} at $z = 3$. The number of galaxies at the value of L^*_{UV} (defined at $z = 3$) found at $z = 6$ is an order of magnitude lower than at $z = 3$. A more detailed study of the LBG luminosity function is done in Lacey et al. (2009).

5.2.2 Examples of Lyman-break Galaxies in the Galaxy Formation Model

As an example of the different formation and merger histories which can produce bright LBGs, we plot in the left panels of Fig. 5.3 and Fig. 5.4 galaxy merger trees for three different present-day galaxy masses. For these examples we require that the LBG appears in the main progenitor branch (leftmost branch). The galaxy trees are plotted in the following way. At each merger, stepping back from $z = 0$, we plot the most massive branch on the left and the other branches to the right. The main progenitor branch is the path traced out from $z = 0$ in this way. Note that at $z > 0$, the main progenitor branch does not necessarily represent the largest progenitor in the whole tree at a given epoch. The largest of all the progenitors at a given time could jump from one branch of the galaxy tree to another and does not define a smooth path back in redshift through the galaxy tree.

In the first example, we show the galaxy merger tree for a galaxy at $z = 0$ with $M_* = 2.5 \times 10^9 h^{-1} M_\odot$ with a bright LBG progenitor at $z = 6$. In the second example, we show the galaxy merger tree for a galaxy at $z = 0$ with $M_* = 6.6 \times 10^{10} h^{-1} M_\odot$ with a bright LBG progenitor at both $z = 6$ and $z = 3$. In the third example, we show the galaxy merger tree for a galaxy at $z = 0$ with $M_* = 2.1 \times 10^{11} h^{-1} M_\odot$ with a bright LBG progenitor at $z = 6$. Note that these trees are purely illustrative examples, chosen to increase the complexity and the mass of the descendants from top to bottom, and are not a statistically representative sample.

In the right hand panels of Fig. 5.3 and Fig. 5.4 we show the evolution of the L_{UV}/L_{UV}^* ratio for the main progenitor galaxy (left most branch) in the trees. To understand better the connection of different galaxy properties at different redshifts, we also follow the evolution of the stellar, host halo and cold gas mass of the galaxy and the mass produced in bursts of star formation. We also plot in the right hand top panels of Fig. 5.3 Fig. 5.4 and the evolution of the bulge to total stellar mass ratio B/T as an indicator of the morphology of the galaxy (and we also show when the central galaxy became a satellite galaxy, if that happens). In the first example, the galaxy became a satellite galaxy at $z = 1.1$, whereas the other two main progenitors are always central galaxies.

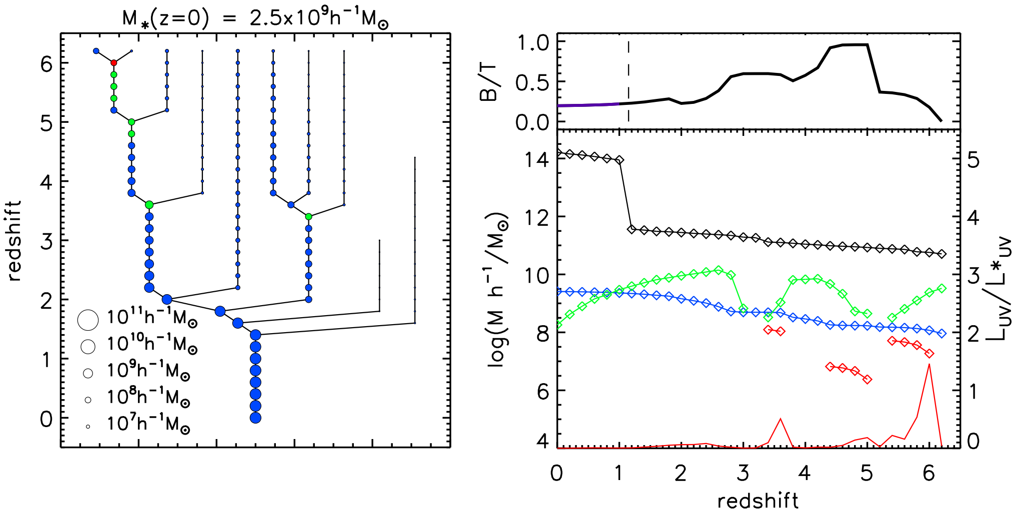

Figure 5.3: Left panel: galaxy merger tree for a galaxy with LBG progenitor. The size of the symbol is proportional to the stellar mass as indicated by the key. The green circles are drawn when $L_{UV} > 0.1L^*_{UV}$, red circles are drawn when $L_{UV} > L^*_{UV}$ and blue if $L_{UV} < 0.1L^*_{UV}$. Right panel: evolution with redshift of the galaxy on the main progenitor branch. Top subpanel: evolution of the bulge to total stellar mass value ratio (B/T). The dashed vertical line indicates the redshift at which the central galaxy (black line) becomes a satellite galaxy (blue line) after a halo merger. Bottom subpanel: the symbols show the evolution of the stellar mass (blue), cold gas mass (green), dark matter host halo mass (black) and the mass formed in ongoing bursts (red) in units according to the left label. The red line shows the evolution of the ratio L_{UV}/L^*_{UV} with redshift in units according to the label at right. Note that L^*_{UV} is defined at $z = 3$. The stellar mass of the galaxy at $z = 0$ is $M_* = 2.5 \times 10^9 h^{-1} M_\odot$.

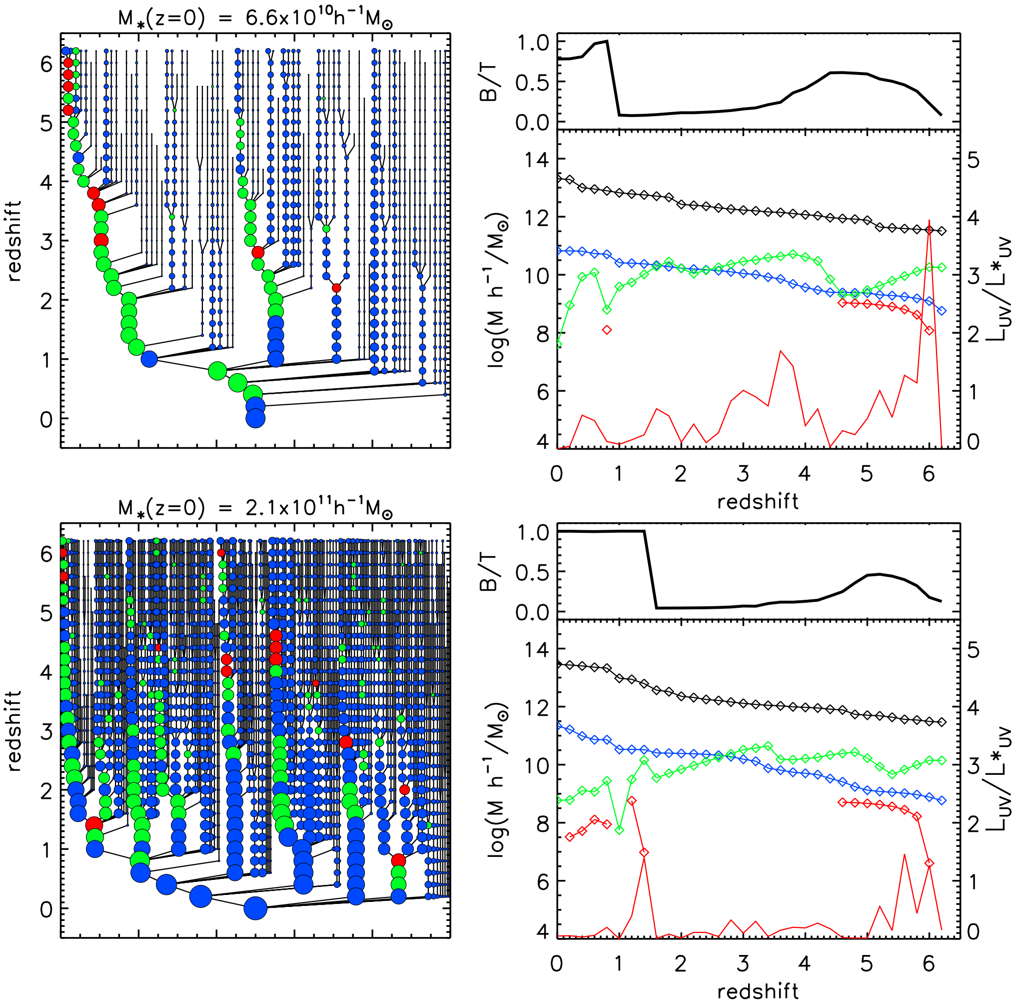

Figure 5.4: Similar to Fig. 5.3. From top to bottom, the stellar mass of the galaxies at $z = 0$ are$M_{*} = 6.6 \times 10^{10}, 2.1 \times 10^{11} [h^{-1} M_{\odot}]$ respectively.

5.3 Properties of LBGs at Different Redshifts and of their $z = 0$ Descendants

Having identified LBGs in the model we compare the stellar mass, host halo mass and morphology of LBGs at different redshifts ($z = 3$ and $z = 6$). By following their evolution, we also investigate the properties of the $z = 0$ descendant galaxies.

5.3.1 Stellar Mass

In the left panels of Fig. 5.5, we plot the stellar mass distribution of faint LBGs ($L_{UV} > 0.1L^{*}_{UV}$) identified at $z = 3$ and $z = 6$. The median stellar mass of faint LBGs at $z = 3$ is $M_{*} = 2.5 \times 10^{8}h^{-1}M_{\odot}$, which is an order of magnitude larger than the median mass of faint LBGs at $z = 6$. In the right panel of the same figure we plot the stellar mass distribution of the $z = 0$ descendants of these two populations ($z = 3$ and $z = 6$). The median of the stellar mass of the descendants of both populations are predicted to be the same (at $M_{*} = 8 \times 10^{9}h^{-1}M_{\odot}$). The descendants of LBGs show a larger range of stellar mass compared to LBGs.

We separate the galaxies into bulge-dominated galaxies (if the bulge to total stellar mass ratio is $B/T > 0.5$) and into disk-dominated galaxies (if $B/T < 0.5$). We find that faint LBGs at $z = 6$ are preferentially bulge-dominated systems (80% are predicted to have $B/T > 0.5$). At $z = 3$ there is a more mixed population with almost half of the faint LBGs predicted to be bulge-dominated systems. Descendants of $z = 3$ and $z = 6$ faint LBGS have similar morphology mixes They are predicted to be mainly disk-dominated systems (60% with $B/T < 0.5$). Lower mass LBG descendants ($M \lesssim 10^{11}h^{-1}M_{\odot}$) are typically predicted to be disk-dominated systems, whereas higher mass LBG descendants ($M \lesssim 10^{11}h^{-1}M_{\odot}$) are typically bulge-dominated systems in the model.

In the left panels of Fig. 5.6 we plot the stellar mass distribution of bright LBGs ($L_{UV} > L^{*}_{UV}$) identified at $z = 6$ and $z = 3$. In this case, the median stellar mass of bright LBGs at $z = 3$ is $M_{*} = 1.25 \times 10^{9}h^{-1}M_{\odot}$, which is five times larger than their faint counterparts, and five times larger than the median mass of bright LBGs at $z = 6$. The median stellar mass of the $z = 0$ descendants of these two populations ($z = 3$ and $z = 6$) are predicted to be $M_{*} = 4 \times 10^{10}h^{-1}M_{\odot}$ for the bright LBGs at $z = 3$ and $M_{*} = 10^{11}h^{-1}M_{\odot}$ for the bright LBGs at $z = 6$ as shown in the right panel of the same figure. Bright LBGs at $z = 6$ and their descendants are predicted to be slightly more bulge dominated than the bright LBGs at $z = 3$ and their descendants.

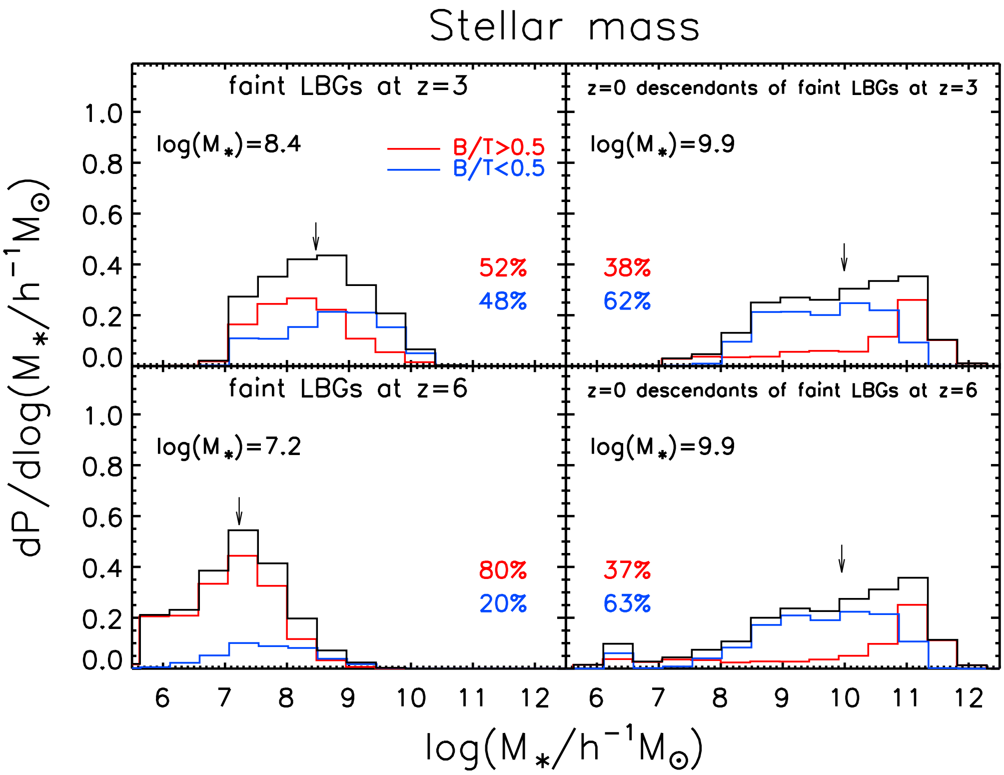

Figure 5.5: Stellar mass distribution of faint LBGs ($L_{UV} > 0.1L^{*}_{UV}$,left) and their $z = 0$ descendants (right). Top panel: For $z = 3$ Lyman-break galaxies, bottom panel: for $z = 6$ Lyman-break galaxies. The median stellar mass value is given in the label and indicated by an arrow. Faint LBGs are separated into bulge-dominated galaxies ($B/T > 0.5$, red) and disk-dominated galaxies ($B/T < 0.5$, blue). The percentage in each class is labelled. The red and blue distributions combine to give the total stellar mass distribution (black).

Descendants of faint LBGs at $z = 3$ and $z = 6$ have similar stellar masses. Descendants of bright LBGs at $z = 6$ have typically somewhat larger masses than the descendants of bright LBGs at $z = 3$.

5.3.2 Host Halo Mass

In the left panel of Fig. 5.7 we plot the mass distribution of dark matter halos which host faint LBGs ($L_{UV} > 0.1L^{*}_{UV}$) identified at $z = 6$ and $z = 3$. Faint LBGs at $z = 3$ live in halos with a median mass of $M_{*} = 8 \times 10^{10}h^{-1}M_{\odot}$, five times larger than the halos that host $z = 6$ faint LBGs. The $z = 0$ descendants of faint $z = 3$ LBGs are hosted by halos with a median mass of $M_{*} = 6.3 \times 10^{12}h^{-1}M_{\odot}$, and the descendants of faint $z = 6$ LBGs are hosted by halos with a median mass of $M_{*} = 10^{13}h^{-1}M_{\odot}$. Halos hosting descendants of faint LBGs have a broader distribution compared to halos hosting the progenitors of

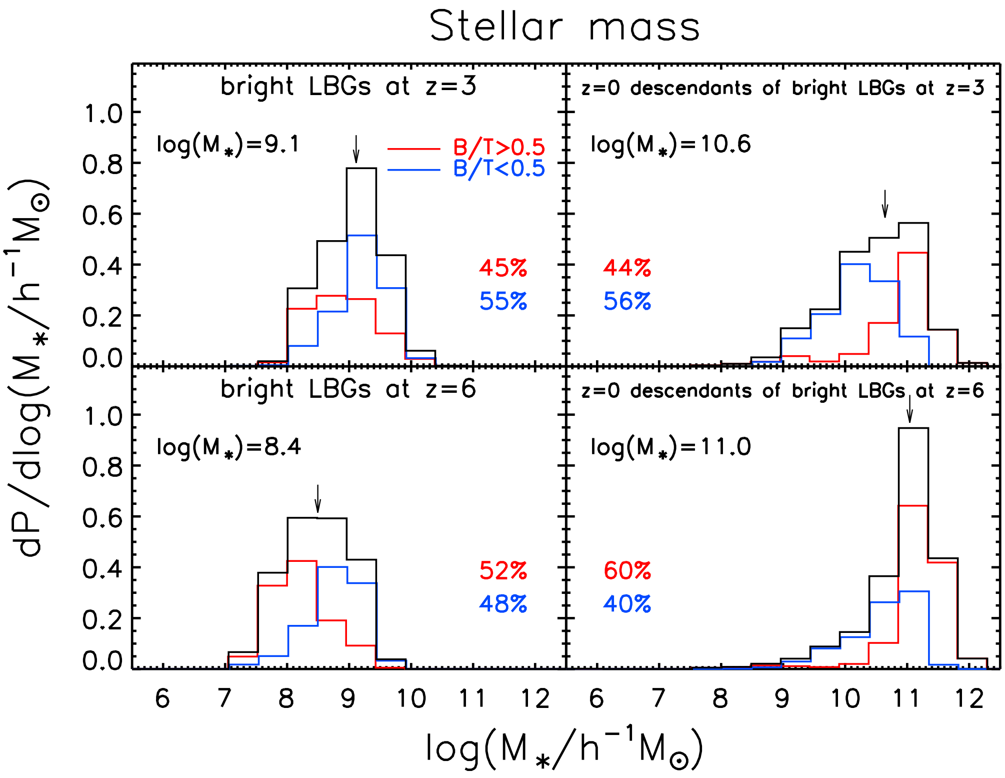

Figure 5.6: Similar to Fig. 5.5 but for bright LBGs ($L_{UV} > L^*_{UV}$).

faint LBGs.

Bright $z = 3$ LBGs live in halos with a median mass of $M_* = 2.5 \times 10^{11} h^{-1} M_\odot$ and the bright $z = 6$ LBGs live in halos with a median mass of $M_* = 1.6 \times 10^{11} h^{-1} M_\odot$. The $z = 0$ descendants of bright $z = 3$ LBGs are hosted by halos with a median mass of $M_* = 10^{13} h^{-1} M_\odot$, and the $z = 0$ descendants of bright $z = 6$ LBGs are hosted by halos with a median mass of $M_* = 5 \times 10^{13} h^{-1} M_\odot$.

5.3.3 Morphology

In Section 4.1 we showed that the model predicts a mix of morphological types (based on the B/T value) for LBGs and their descendants. Here we study the distribution of B/T predicted by the model.

In Fig. 5.9 we show the bulge to total stellar mass ratio (B/T) for faint LBGs and their descendants. In Fig. 5.10 we show the predictions for bright LBGs. Despite the fact that faint LBGs at $z = 3$ and $z = 6$ show a different distribution of morphological types (more bulge dominated LBGs are predicted at $z = 6$), their descendants show a very similar distribution of types.

When we separate LBGs in central and satellite galaxies we find that more than 97% of

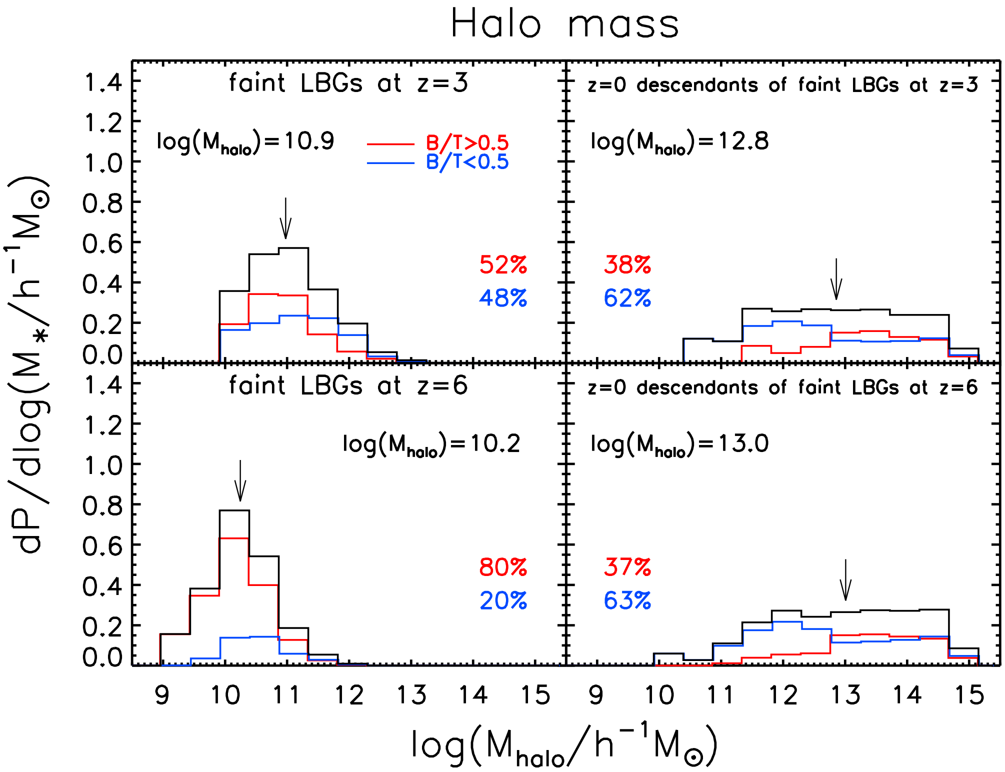

Figure 5.7: Host halo mass distribution of faint LBGs ($L_{UV} > 0.1L^*_{UV}$,left) and the host halo mass distribution of their $z = 0$ descendants (right). Top panel: For $z = 3$ Lyman-break galaxies, bottom panel: for $z = 6$ Lyman-break galaxies. The median host halo mass value is written and indicated by an arrow.

the LBGs are central galaxies. The $z = 0$ descendants are typically a mix of populations, where central galaxies represent around 60% of the total LBG descendants.

5.4 Present-Day Galaxies with LBG Progenitor

In the previous section we selected LBGs at redshifts $z = 3$ and $z = 6$ and compared the properties of their $z = 0$ descendants. In this section we study what is the predicted probability for present-day galaxies to have LBGs progenitors and what is the probability for present-day halos to have progenitors that hosted LBGs.

In the left panels of Fig. 5.11 we plot the fraction of present-day galaxies that are predicted to have at least one faint LBG progenitor as a function of the stellar mass. The model predicts a very similar probability of having $z = 3$ and $z = 6$ faint LBGs (in Fig. 5.5 we already found that the stellar mass distribution of the $z = 0$ descendants were similar for $z = 3$ and for $z = 6$ faint LBGs). We find that all galaxies with stellar masses larger than $M > 2.5 \times 10^{11} h^{-1} M_{\odot}$ are predicted to have faint LBGs progenitors at $z = 3$

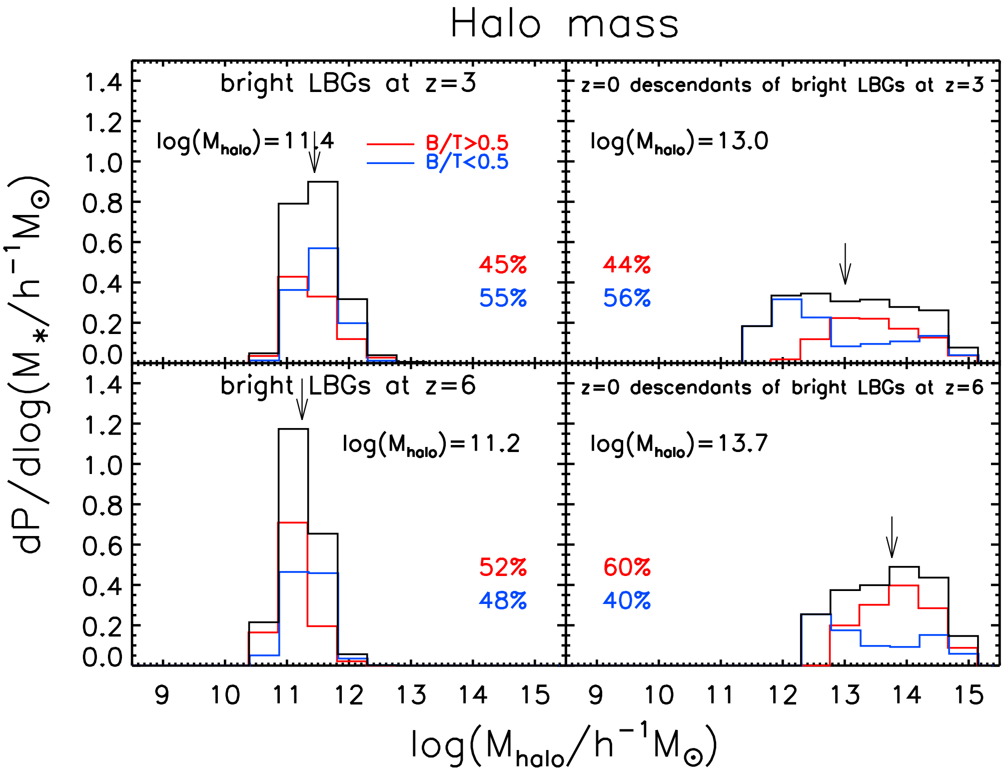

Figure 5.8: Similar to Fig. 5.7 but for halos hosting bright LBGs ($L_{UV} > L^*_{UV}$).

and at $z = 6$. Galaxies with a mass of $M = 4 \times 10^9 h^{-1} M_\odot$ are predicted to have a 10% of probability of having faint LBGs progenitors at $z = 3$ and at $z = 6$. A Milky Way mass galaxy ($M = 4 \times 10^{10} h^{-1} M_\odot$, taken from adding the disk and bulge Milky Way mass given by Binney and Tremaine 2008) is predicted to have a 50% of probability of having a faint LBG progenitor at $z = 3$ or at $z = 6$. Expressed in terms of halo masses (right panel of same figure), we find that all halos today with a mass larger than $M > 5 \times 10^{13} h^{-1} M_\odot$ are predicted to have halo progenitors that hosted faint LBGs at $z = 3$ and $z = 6$.

In the left panels of Fig. 5.12 we show the equivalent results for bright LBG progenitors. We find that galaxies with a mass of $M = 8 \times 10^{10} h^{-1} M_\odot$ are predicted to have a 10% of probability of having at least one bright LBG progenitor at $z = 3$. Galaxies with a mass of $M = 1.25 \times 10^{11} h^{-1} M_\odot$ are predicted to have a 10% of probability of have at least one bright LBG progenitor at $z = 6$. A Milky Way mass galaxy is predicted to have a 6% and a 2% of probability of having a bright LBG progenitor at $z = 3$ and at $z = 6$, respectively. From the right panel of the same plot, we find that all present-day halos with a mass larger than $M > 10^{14} h^{-1} M_\odot$ are predicted to have halo progenitors that hosted bright LBGs at $z = 3$.

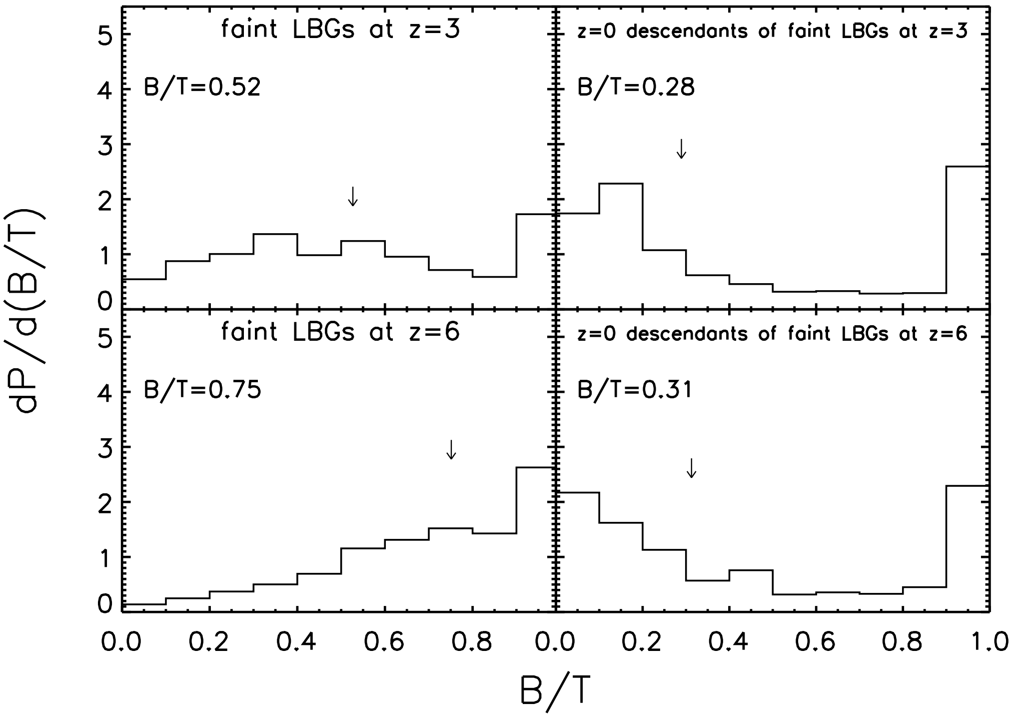

Figure 5.9: Bulge to total stellar mass ratio (B/T) distribution of faint LBGs ($L_{UV} > 0.1L^*_{UV}$,left) and B/T distribution of their $z = 0$ descendants (right). Top panel: For faint $z = 3$ Lyman-break galaxies, bottom panel: for faint $z = 6$ Lyman-break galaxies. The median B/T value is written in each panel and indicated by an arrow.

5.5 Burst and Quiescent Star Formation in LBGs

As mentioned, the model considers two modes of star formation, each with a different IMF. This has an impact on the number and properties of LBGs. In this section we study the correlation of the star formation, stellar mass and UV luminosity in the galaxies at $z = 3$ and $z = 6$. We want to understand what is the contribution between the different star formation mechanisms (quiescent or bursts) and the production of LBGs at the different redshifts.

To start, we select all galaxies at $z = 3$ and $z = 6$ and we plot in Fig. 5.13 the stellar mass vs host halo mass (left panel), the stellar mass vs star formation rate SFR (middle panel) and the stellar mass vs the L_{UV}/L^*_{UV} ratio. To gain more from this we separate the galaxies according to which mechanism of star formation is dominant. We plot galaxies in red if the burst SFR is higher than the quiescent SFR and in blue if the quiescent SFR is the higher.

We see that there is a correlation between the stellar and host halo mass of the galaxies.

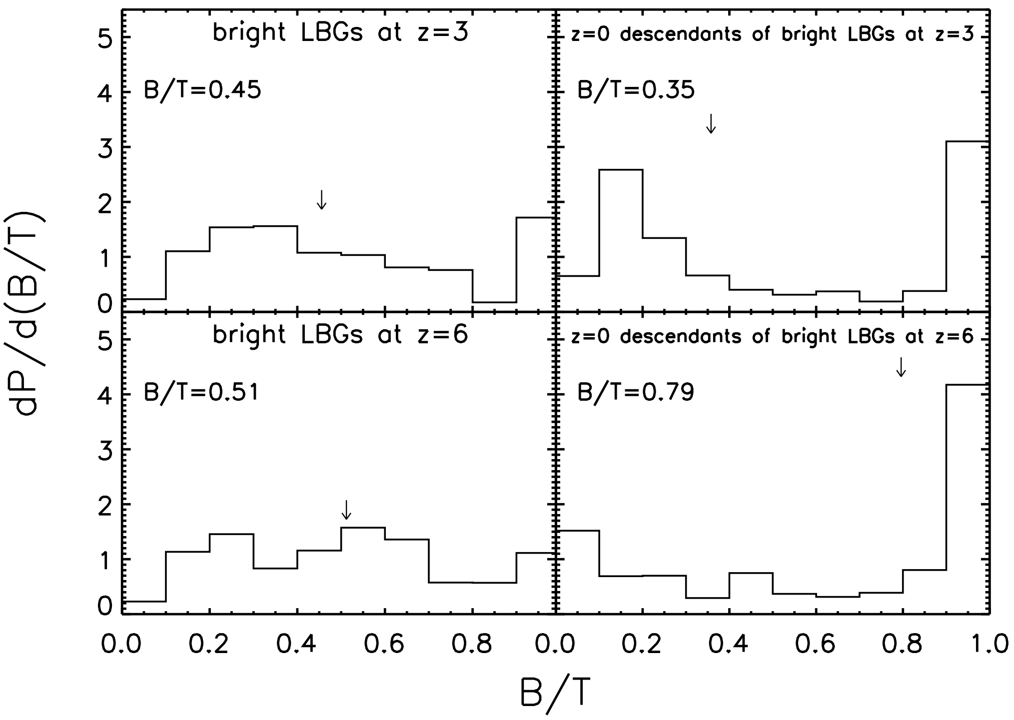

Figure 5.10: Similar to Fig. 5.9 but for bright LBGs ($L_{UV} > L^*_{UV}$).

The tight correlation observed is typically for central galaxies that actively keep merging with other galaxies. This is more obvious in Fig. 5.14, where we have separated the galaxies into central and satellites. More passive galaxies, typically satellite galaxies in the model are responsible for the large scatter in the relation.

There is also a correlation between the stellar mass and star formation rate. The tight correlation observed in this case is produced by galaxies where the quiescent star formation dominates (as suggested by the blue contours). The model predicts that quiescent star formation rate is proportional to the stellar mass. The scatter is produced mainly by galaxies undergoing bursts of star formation.

Now we repeat the same exercise but for Lyman-break galaxies:

- In Figs. 5.15 and 5.16 we plot the relations for faint and bright LBGs respectively. We plot galaxy density in red if the burst SFR is larger that quiescent star formation and in blue if the quiescent SFR is larger that burst star formation. Most LBGs are produced by bursts of star formation. LBGs where the quiescent star formation dominates have typically larger masses compared to LBGs where bursts dominate. LBGs dominated by quiescent star formation require a higher star formation rate to be bright in the rest-frame UV band due to the IMF addopted in the quiescent

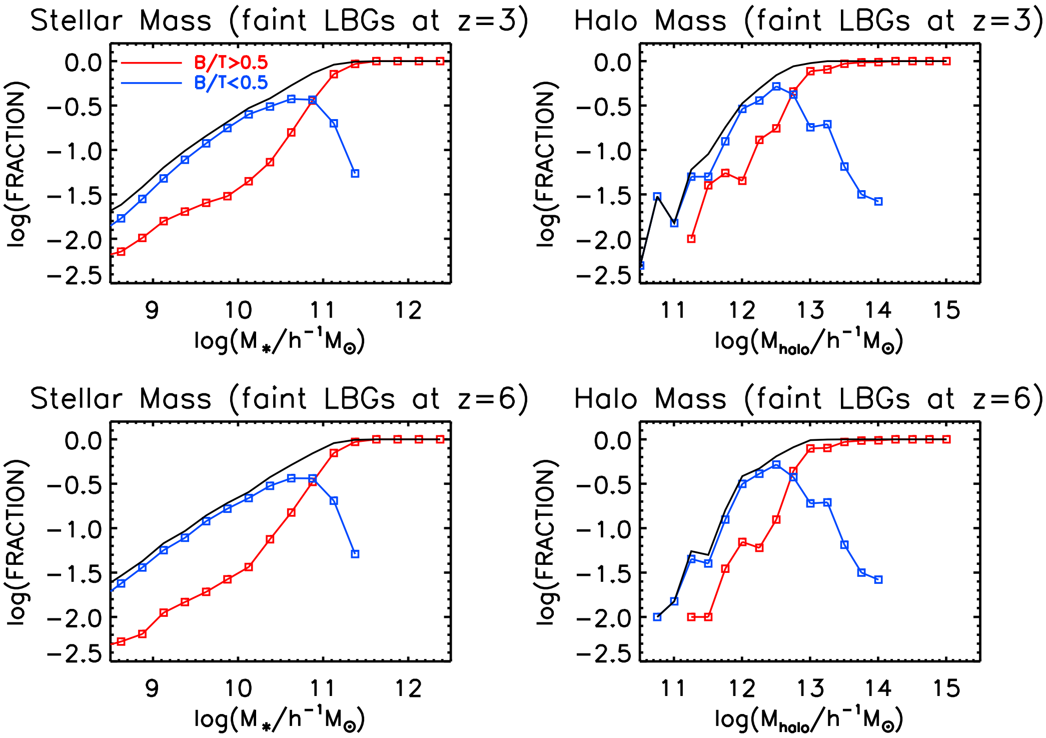

Figure 5.11: Left panels: fraction of present-day galaxies by stellar mass that are predicted to have faint LBGs progenitors ($L_{UV} > 0.1L^*_{UV}$). Right panels: fraction of present-day halos by mass that are predicted to have halo progenitors that hosted at least one faint LBG progenitor. Top panel for $z = 3$ progenitors and bottom panel for $z = 6$ progenitors. Galaxies are separated in bulge-dominated ($B/T > 0.5$) descendants in red and disk-dominated ($B/T < 0.5$) descendants in blue. The black line represents all LBG descendants (the sum of the blue and red line).

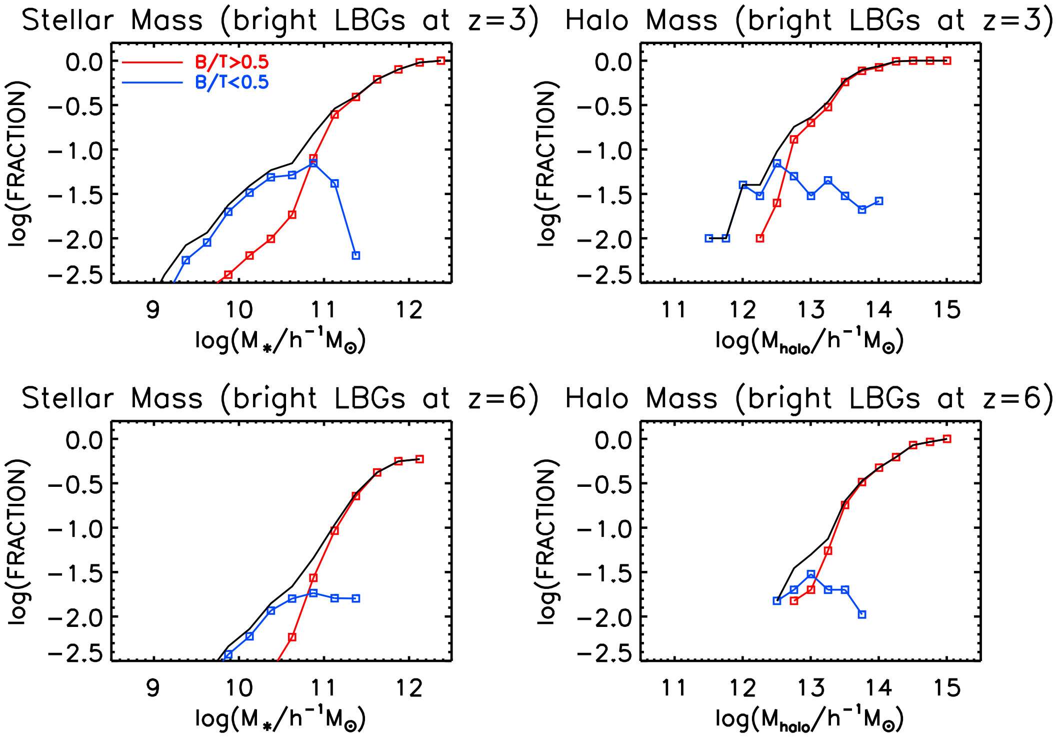

Figure 5.12: Similar to Fig. 5.11 but computing the probability for bright LBG progenitors ($L_{UV} > L^*_{UV}$).

mode of star formation.

- In Figs. 5.17 and 5.18 we plot the relations for faint and bright LBGs respectively. Here, we plot galaxy density in red if the total mass produced by burst in the galaxy is at least half of the total stellar mass of the galaxy and in blue otherwise. The model predicts that almost all LBGs at $z = 6$ have built their stellar mass through burst processes. At $z = 3$, quiescent star formation have contributed larger than bursts in more than 60% of the LBGs. LBGs with a larger contribution from quiescent star formation are predicted typically slightly larger than LBGs with a larger contribution from bursts.

- In Figs. 5.19 and 5.20 we plot the relations for faint and bright LBGs respectively. We plot galaxy density in red if the total mass produced in the ongoing burst in the galaxy (if any) is at least half of the total stellar mass of the galaxy and in blue otherwise. The contribution from the ongoing bursts to the stellar mass of LBGs is more important at $z = 6$ than at $z = 3$.

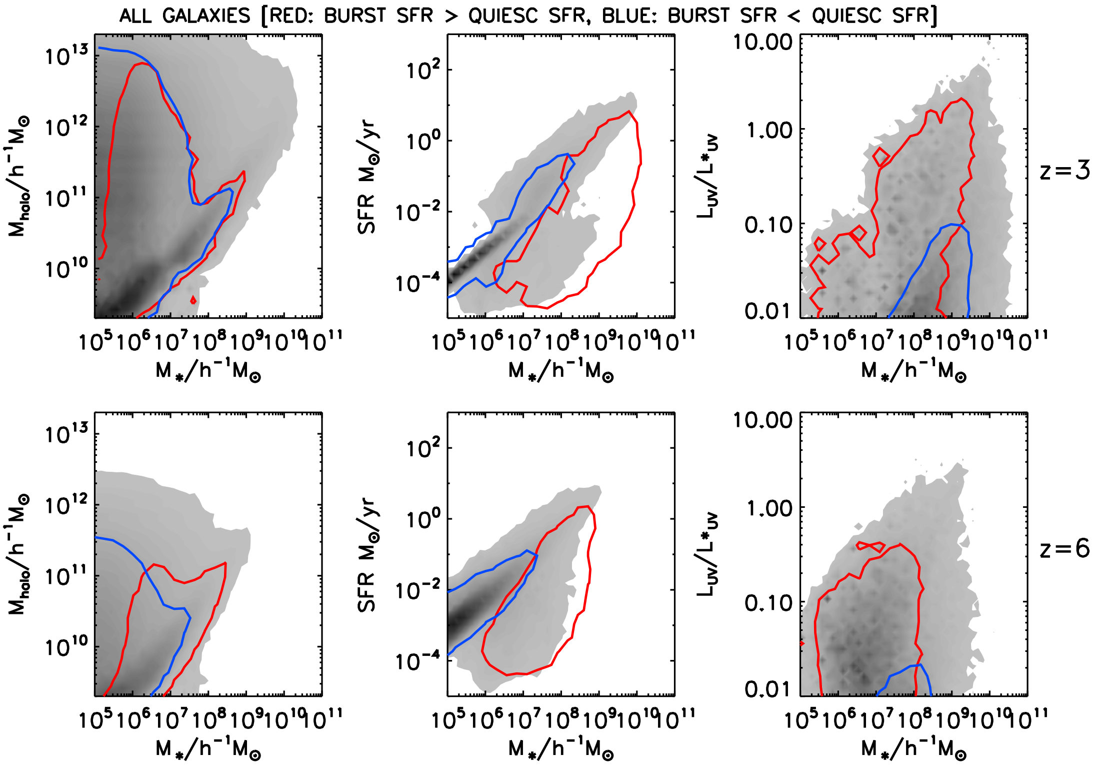

Figure 5.13: For all galaxies at $z = 3$ (top panels) and $z = 6$ (bottom panels) we plot the stellar mass vs host halo mass (left panels), the stellar mass vs star formation rate (middle panels) and the stellar mass vs L_{UV}/L^*_{UV} ratio (right panels) densities. We plot galaxy density contours in red if the burst SFR is higher than the quiescent SFR and in blue if the opposite is true. The contours enclose 95% of the selected densities. The colour shading reflects the square root of the number density.

5.6 What is the connection between LBGs and SMGs?

The Lyman-break technique and sub-millimetre surveys are two of the most successful and productive methods for uncovering significant populations of high redshift galaxies. LBGs are selected on the basis of their emission in the UV. SMGs are detected through the reradiation by dust of light absorbed predominantly in the UV. It is natural to ask what is the overlap, if any between these two populations. A first indication of the answer is suggested by the different redshift ranges of the populations. LBGs selected using ground based photometry are restricted to have $z \geq 3$. Bright SMGs (with 850μm flux $S_{850} > 5$ mJy), on the other hand, have a median redshift of $z \sim 2$. Hence, we will be looking at the UV luminosity of galaxies in the high redshift tail of the SMG redshift distribution. Almeida et al. (2010) performed a similar comparison at $z = 2$, and found that $\approx 1\%$ of galaxies bright in the UV were also bright SMGs.

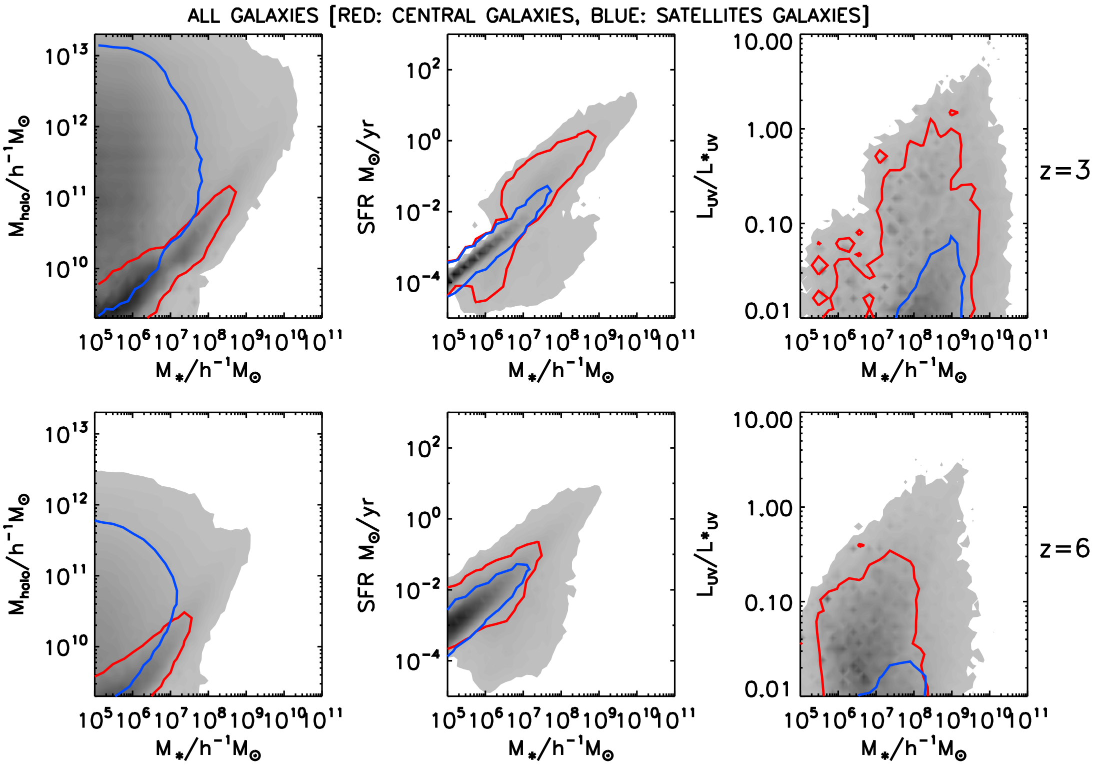

Figure 5.14: Similar to Fig. 5.13. We plot galaxy density contours in red for central galaxies and in blue for satellite galaxies.

The multiwavelength nature of our semi-analytical model and its self consistent treatment of dust make it ideally placed to address the overlap between the SMG and LBG populations. Here we examine the predicted relation between 850μm flux and UV luminosity at $z = 3$ and $z = 6$. Following the companion to this paper (Gonzalez et al. 2010), in which we study the evolution of SMGs in the model, we define a galaxy as a bright SMG when its 850μm flux exceeds 5 mJy and as a faint SMG when its 850μm flux exceeds 1 mJy.

The top panels of Figs. 5.21 and 5.22 show the relation between the 850 μm flux and the UV luminosity for galaxies at $z = 3$ and $z = 6$, respectively. There is scatter in this relation, particularly at fainter magnitudes. Nevertheless an increase in the UV luminosity typically corresponds to an increase in the submillimetre flux. We find that only 2.3% of the bright LBGs ($L_{UV} > L^*_{UV}$) are also bright SMGs ($S_{850} > 5$ mJy) at $z = 3$. This figure decreases to 0.5% for $z = 6$. At $z = 3$, almost half (46%) of the bright SMGs are predicted to also be bright LBGs. We find that approximately one third of the bright SMGs are bright LBGs at z=6 (we note that the model predicts very few SMGs at $z = 6$, as suggested by the redshift distributions plotted in Baugh et al. 2005).

The middle panels of Figs. 5.21 and 5.22 show the number density of galaxies as a

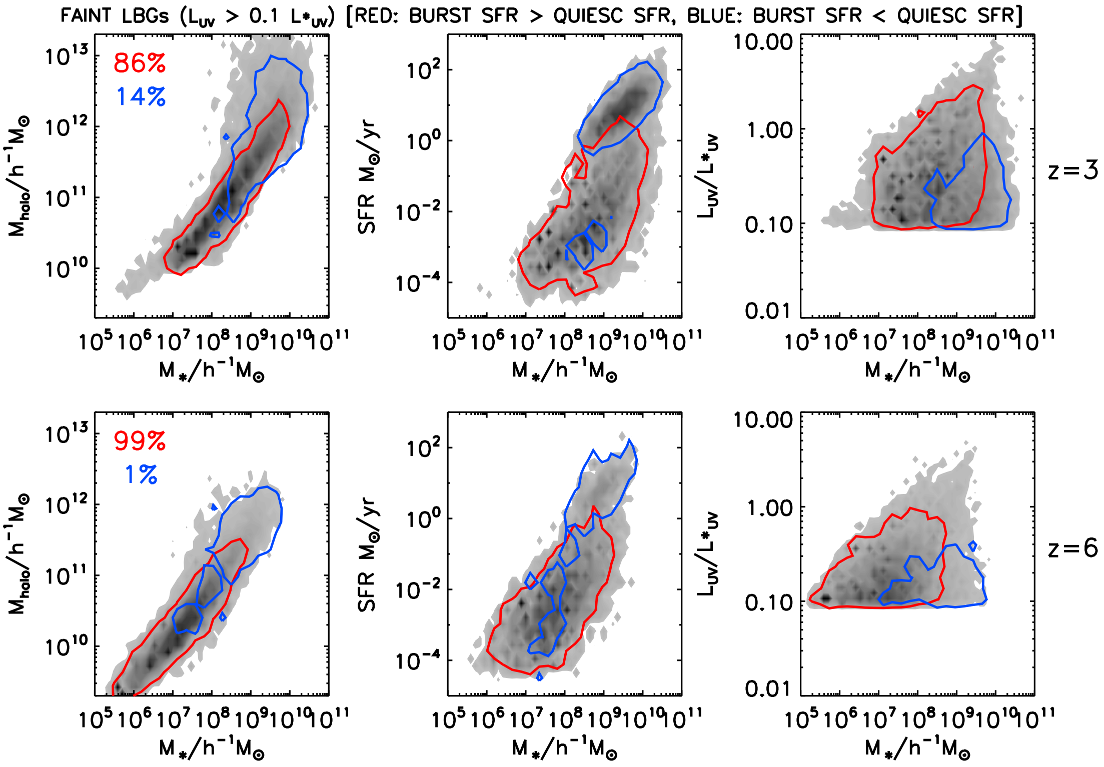

Figure 5.15: Similar to Fig. 5.13 but for faint LBGs. We plot galaxy density contours in red if the burst SFR is higher than the quiescent SFR and in blue if the quiescent SFR is higher than the burst SFR.

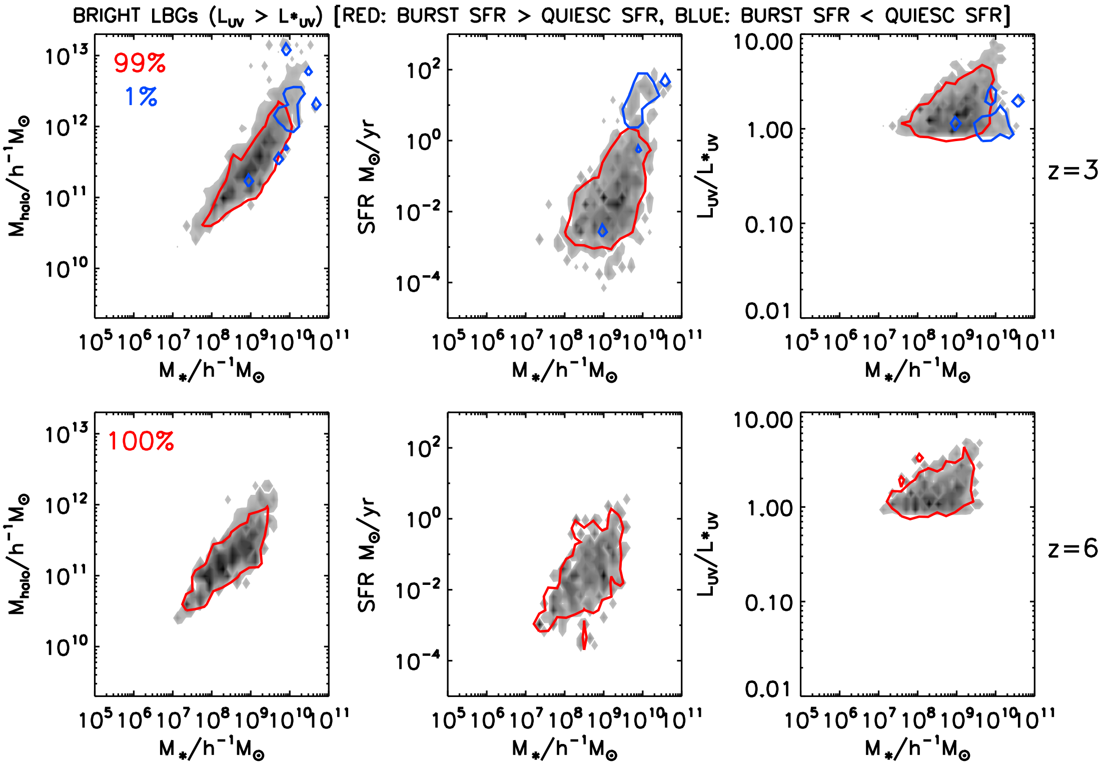

Figure 5.16: Similar to Fig. 5.13 but for bright LBGs. We plot galaxy density contours in red if the burst SFR is higher than the quiescent SFR and in blue if the quiescent SFR is higher than the burst SFR.

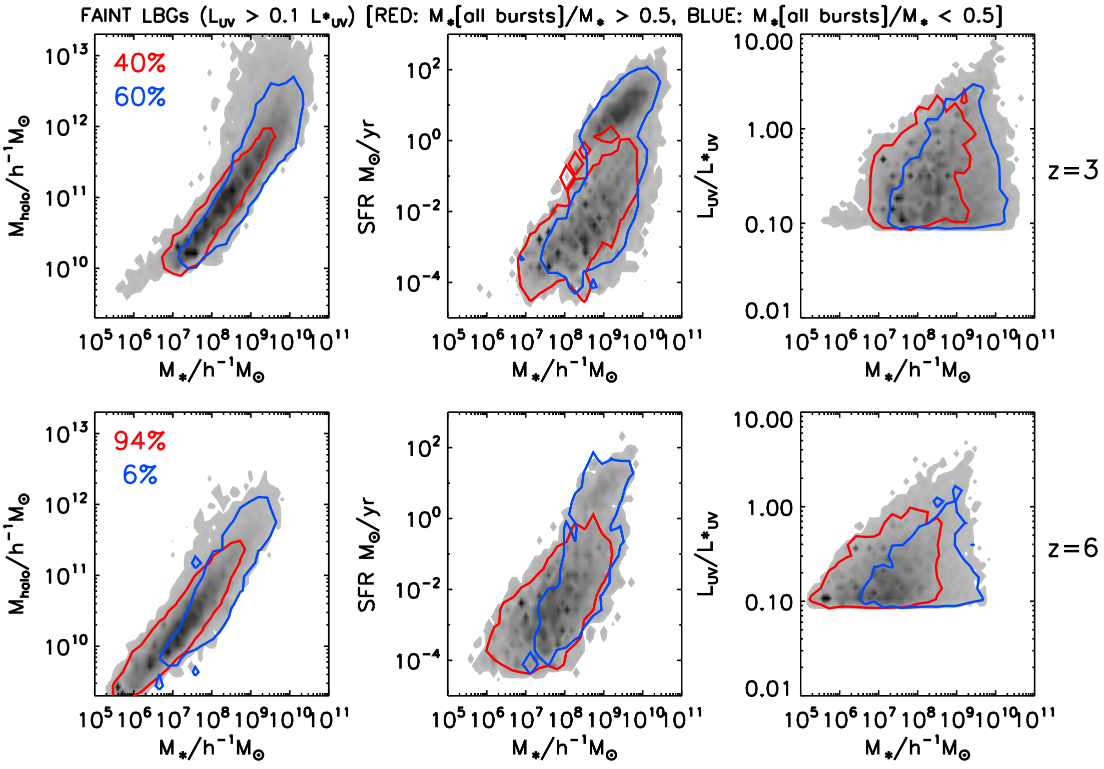

Figure 5.17: Similar to Fig. 5.13 but for faint LBGs. We plot galaxy density contours in red if all the mass produced by bursts is higher than half of the total stellar mass of the galaxy and in blue otherwise.

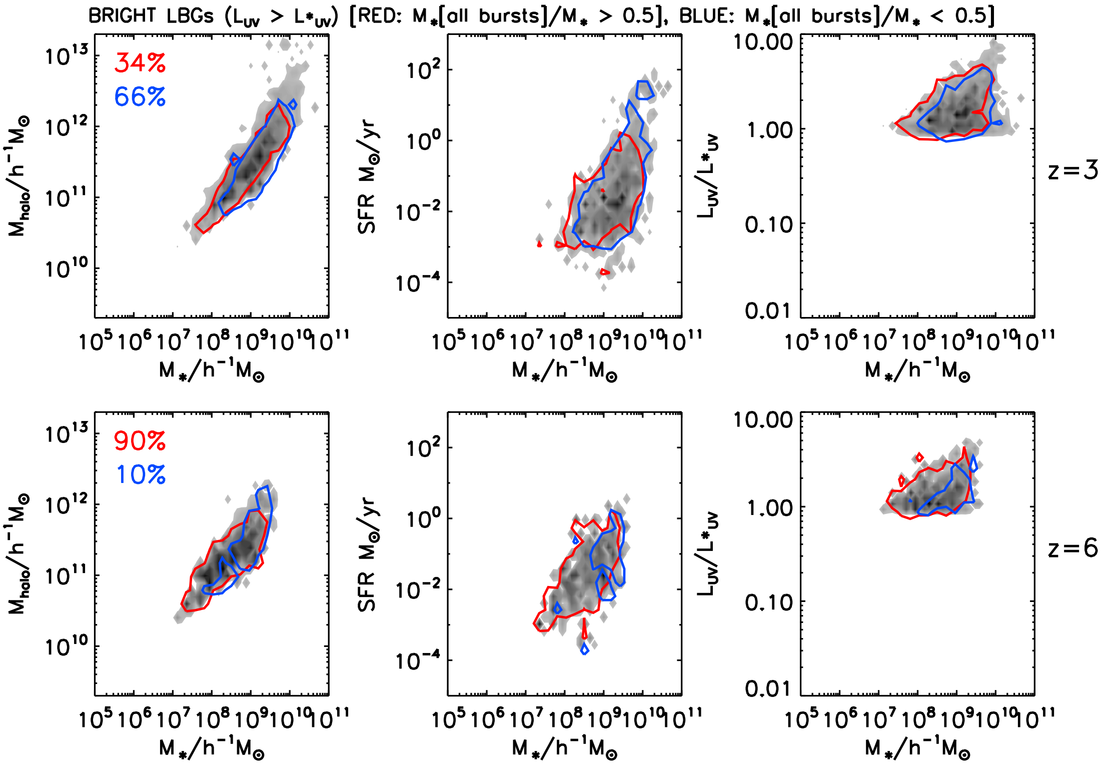

Figure 5.18: Similar to Fig. 5.13 but for bright LBGS. We plot galaxy density contours in red if all the mass produced by bursts is higher than half of the total stellar mass of the galaxy and in blue otherwise.

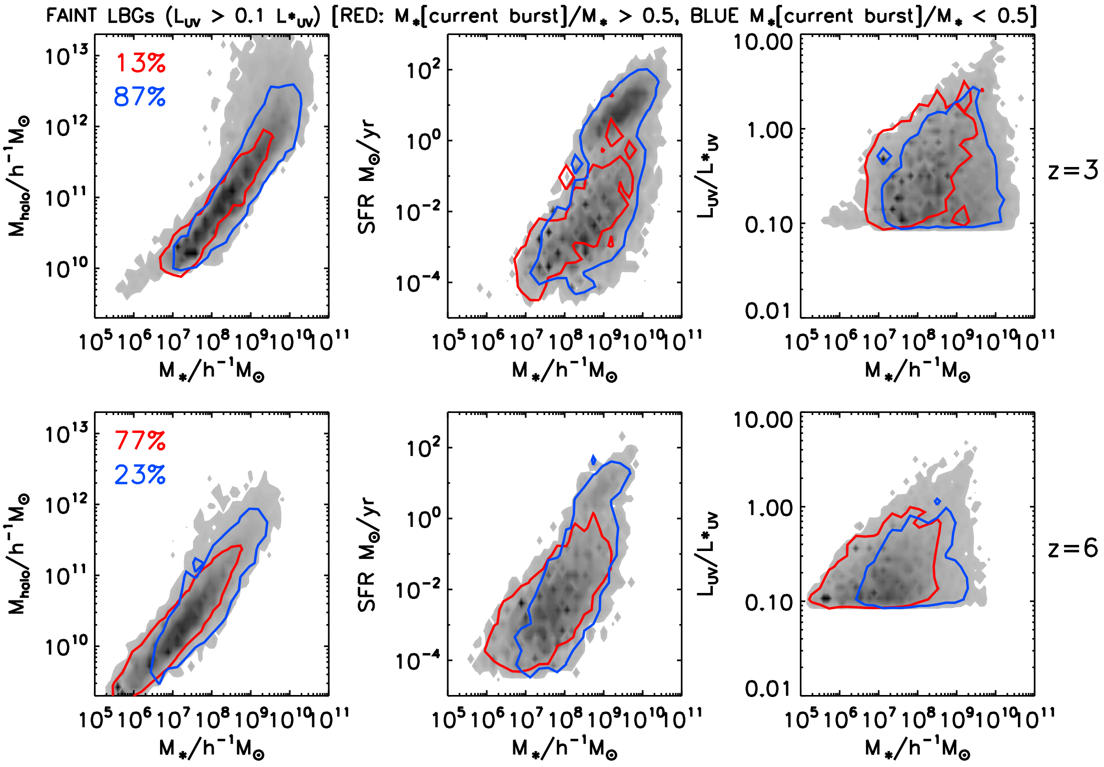

Figure 5.19: Similar to Fig. 5.13 but for faint LBGs. We plot galaxy density contours in red if all the mass produced by the ongoing bursts is higher than half of the total stellar mass of the galaxy and in blue otherwise.

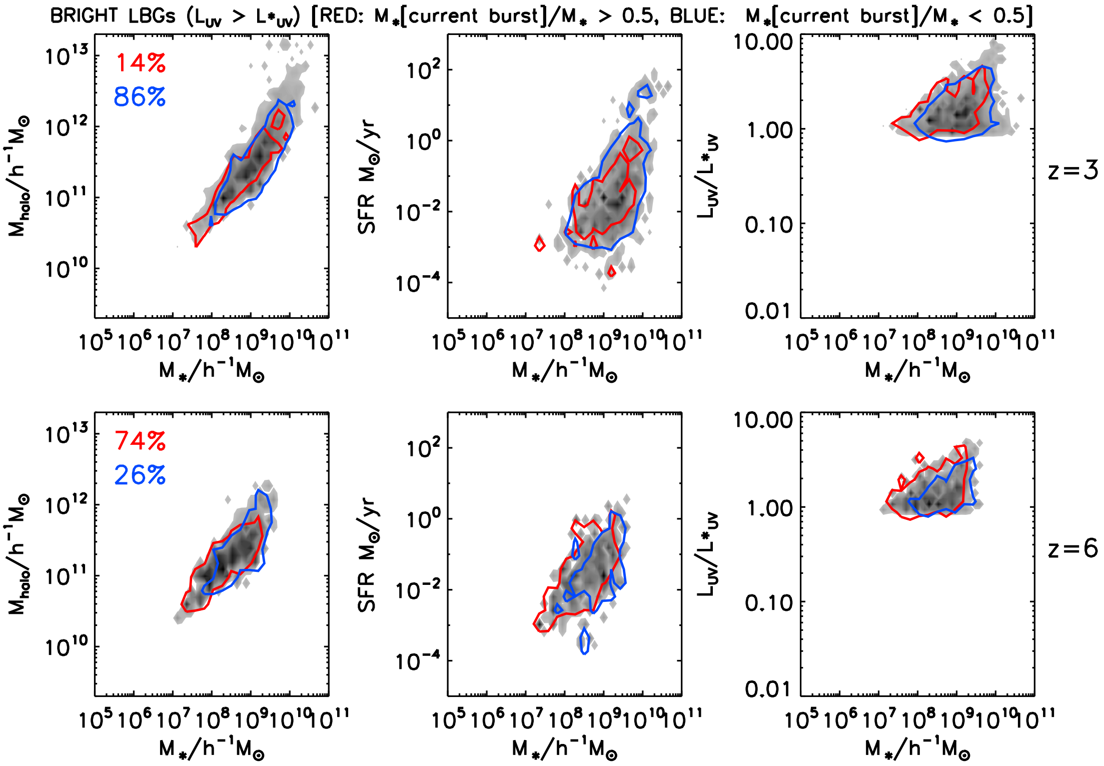

Figure 5.20: Similar to Fig. 5.13 but for bright LBGS. We plot galaxy density contours in red if all the mass produced by the ongoing bursts is higher than half of the total stellar mass of the galaxy and in blue otherwise.

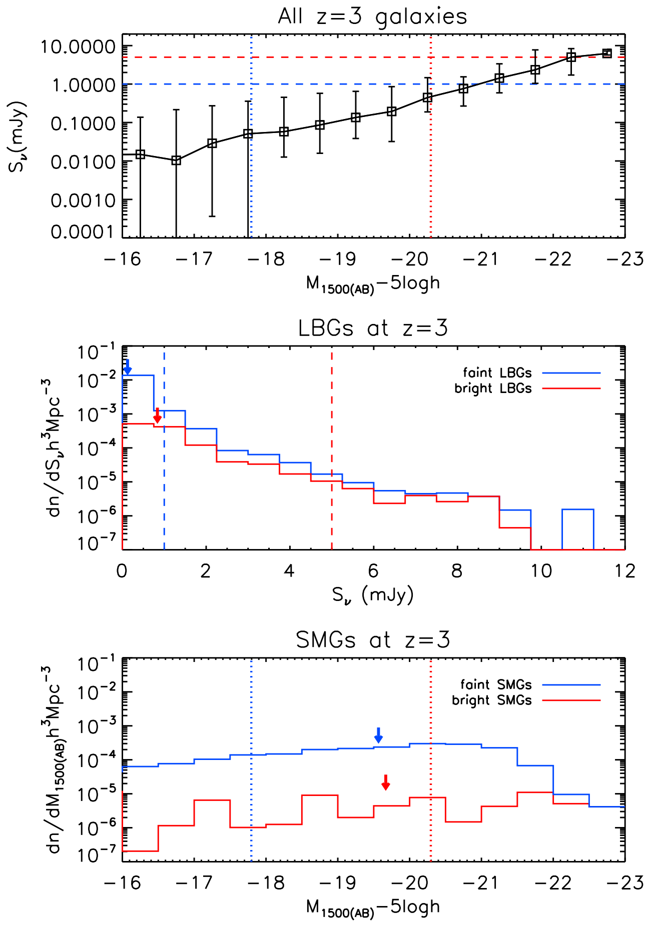

Figure 5.21: *Top panel:* the median 850 μm flux as a function of the UV magnitude for galaxies at z=3. The bars indicate the 10 to 90 percentile range of the distribution in each magnitude bin. The horizontal lines indicate 1 and 5 mJy thresholds, which we use to denote faint and bright SMGs in Gonzalez et al. (2010), and the vertical lines indicate the faint ($0.1L^*_{UV}$) and bright (L^*_{UV}) LBG thresholds. *Middle panel:* the number density of galaxies as a function of 850 μm flux for faint LBGs (blue histogram) and bright LBGs (red histogram) at $z = 3$. *Bottom panel:* the number density of galaxies as a function of UV magnitude for faint SMGs ($S_{850} > 1$ mJy, blue histogram) and bright SMGs ($S_{850} >$ 5 mJy, red histogram) at $z = 3$. In the middle and bottom panels, the arrows indicate the median value of the SMG flux and LBG luminosity, respectively, for each sample.

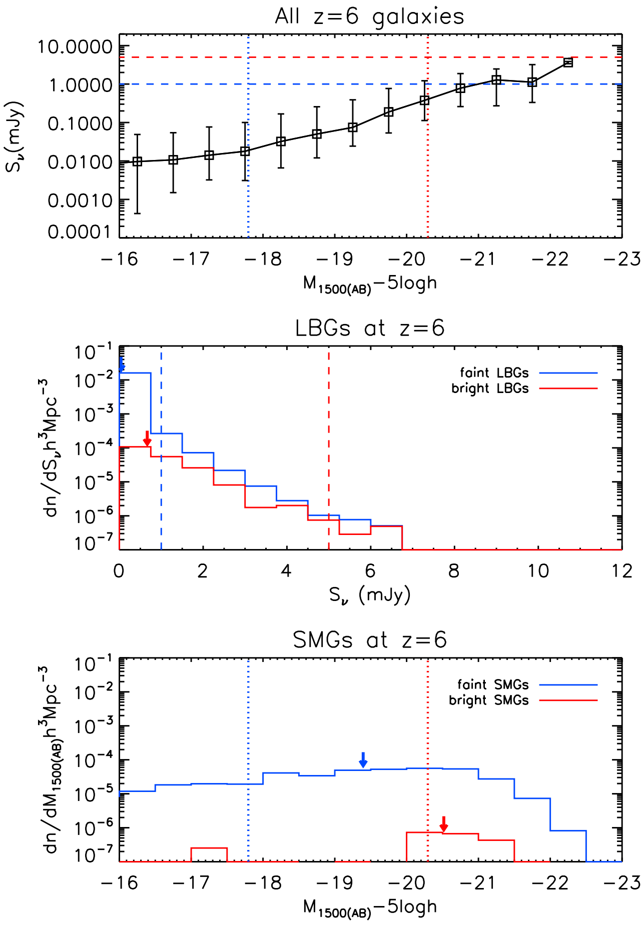

Figure 5.22: *Top panel:* the median 850 μm flux as a function of the UV magnitude for galaxies at z=6. The bars indicate the 10 to 90 percentile range of the distribution in each magnitude bin. The horizontal lines indicate 1 and 5 mJy thresholds, which we use to denote faint and bright SMGs in Gonzalez et al. (2010), and the vertical lines indicate the faint ($0.1L^*_{UV}$) and bright (L^*_{UV}) LBG thresholds. *Middle panel:* the number density of galaxies as a function of 850 μm flux for faint LBGs (blue histogram) and bright LBGs (red histogram) . *Bottom panel:* the number density of galaxies as a function of UV magnitude for faint SMGs ($S_{850} > 1$ mJy, blue histogram) and bright SMGs ($S_{850} > 5$ mJy, red histogram). In the middle and bottom panels, the arrows indicate the median value of the SMG flux and LBG luminosity, respectively, for each sample.

function of their 850μm flux, with separate curves for faint and bright LBGs at $z = 3$ and $z = 6$, respectively. At both redshifts, the median fluxes at 850μm are predicted to be fainter than the faint SMG criteria adopted here (1 mJy). The median flux is a little bit larger for bright LBGs.

In the bottom panels of Figs. 5.21 and 5.22, we show the predicted number density of galaxies as a function of UV magnitude, distinguishing between faint and bright SMGs found at $z = 3$ and $z = 6$ respectively. At $z = 3$, the median UV magnitude is similar for faint and bright SMGs ($\approx 0.5L^*$). At $z = 6$ the median UV magnitude is predicted to be a little bit fainter for the faint SMGs than it is at $z = 3$. The median UV magnitude for the bright SMGs at $z = 6$ is predicted to be brighter than L^* (but again we note that the model predicts very few SMGs at z=6).

5.7 Summary and Discussions

The Baugh et al. version of the `GALFORM` model matches the luminosity function of Lyman-break galaxies at redshifts $z = 3$ and $z = 6$. We have used the characteristic observed UV luminosity at $z = 3$ to define model galaxies to be faint and bright LBGs. The model predicts that faint LBGs at $z = 6$ have a median stellar mass of $M = 1.6 \times 10^7 h^{-1} M_\odot$ and are typically bulge dominated systems (80% of the population has $B/T > 0.5$). At $z = 3$, faint LBGs are 15 times more massive than the ones identified at $z = 6$, and they have a mix of morphological types (52% have $B/T > 0.5$).

Bright LBGs at $z = 6$ have a median stellar mass of $M = 2.5 \times 10^8 h^{-1} M_\odot$ and they again have a range of morphological types (51% have $B/T > 0.5$). Bright LBGs at $z = 6$ are 15 times more massive than faint LBGs at the same redshift. At $z = 3$, bright LBGs are 5 times more massive than $z = 6$ bright LBGs, and they are preferentially bulge dominated systems (60% have $B/T > 0.5$). Bright LBGs at $z = 3$ are 5 times more massive than faint LBGs at the same redshift.

Faint LBGs at $z = 3$ and $z = 6$ have different stellar masses and different mixes of morphological types, but, interestingly, they evolve into similar present-day galaxies that live in similar halos. Their $z = 0$ descendants are predicted to have the same median stellar mass ($M = 8 \times 10^9 h^{-1} M_\odot$), a similar mix of morphological types (63% of their descendants are predicted to be disk-dominated galaxies), and they are hosted by halos with similar median mass ($M = 6 - 10 \times 10^{12} h^{-1} M_\odot$).

The descendants of bright LBGs at $z = 3$ are predicted to have a median stellar mass

($M = 4 \times 10^{10} h^{-1} M_{\odot}$) similar to the Milky Way mass, while the descendants of bright LBGs at $z = 6$ are predicted to have a larger median stellar mass ($M = 10^{11} h^{-1} M_{\odot}$).

When we compute the fraction of present-day galaxies that are predicted to have LBG progenitors, we find that one in every 2 Milky Way mass galaxy has at least one faint LBG progenitor at $z = 3$ or $z = 6$. The median stellar mass of the $z = 0$ descendants of bright LBGs at $z = 3$ is a Milky Way mass galaxy and the $z = 0$ descendants of bright LBGs at $z = 6$ have larger masses. The model predicts that only one in every 16 and one in every 50 Milky Way mass galaxy is predicted to have a bright LBG progenitor at $z = 3$ and $z = 6$ respectively.

By investigating the star formation in the LBGs identified in the model, we find that most faint LBGs and almost all bright LBGs are produced by bursts of star formation. The `GALFORM` model uses a top-heavy IMF in this mode of star formation. This IMF produces a larger fraction of high-mass stars compared to the Kennicutt IMF used in the quiescent star formation mode. The increase in UV radiation generated by the top-heavy IMF makes it easier for a galaxy to increase its UV luminosity and become a LBG in the model after undergoing a merger.

As a consequence of the different IMFs used, we find fewer LBGs where the quiescent mode of star formation rate dominates, compared to the ones where the bursts dominate. Since the Kennicutt IMF in quiescent star formation is less efficient in producing LBGs, these galaxies show a higher total star formation rate, which is needed to exceed the UV luminosity threshold to be identified as LBGs in the model. Since the model predicts a tight relation between star formation rate and stellar mass for LBGs, LBGs produced by quiescent star formation typically show a larger stellar mass.

With respect to the contribution to the stellar mass of LBGs from the different IMF modes, we find that most of the LBGs at $z = 6$ (94% for faint LBGs and 90% for bright LBGs) have built their mass through bursts of star formation after merging with other galaxies. For LBGs at $z = 3$, quiescent star formation becomes more important, and quiescent star formation contributes more to the stellar mass of the galaxy (60% for faint LBGs and 66% for bright LBGs)

Finally we examined the overlap between LBGs and SMGs, extending the comparison carried out by Almeida et al. (2010) at $z = 2$, to $z = 3$ and $z = 6$, which probes the tail of the redshift distribution of bright SMGs. Only 2% of bright LBGs at $z = 3$ are predicted to also be bright SMGs, which explains the difficulty in detecting 850 μm flux form SMGs (e.g Adelberger and Steidel, 2000).

Chapter 6

Conclusions

The subjects covered in this thesis can be grouped into two areas. The main results are discussed below along with possible directions for future work.

6.1 Physical Processes Behind the Properties of Present-Day Galaxies

The unprecedented size and uniform selection of the Sloan Digital Sky Survey (SDSS) makes it an invaluable resource for testing galaxy formation models. For the first time it is possible to obtain reliable colours, morphology and size distributions. To take advantage of this, in Chapter 3 we performed a careful comparison of the `GALFORM` model predictions and SDSS observational data in a consistent way. `GALFORM` models the luminosity, colour and size of the disk and bulge components of a galaxy, and so we can compute quantities which can be compared directly with SDSS observations, such as the Petrosian magnitude, the radius containing 50 per cent of the Petrosian flux (R_{50}), the concentration parameter (c) and the Sérsic index (n). From this, we were able to compare the luminosity function, colours, sizes and morphology distributions of present-day galaxies between the models and the SDSS. As an indicator of the morphology of the galaxies we used the values of concentration index, c, and Sérsic index, n, computed by Blanton et al. (2005b) and the value of the bulge-to-total luminosity ratio (B/T) computed by Benson et al. (2007). The correlations between the different indicators of galaxy morphology show a larger scatter for the $c - B/T$ plane than for the $c - n$ plane.

We tested the predictions of two published versions of the `GALFORM` model: the Baugh et al. (2005) model, which assumes a top-heavy initial mass function (IMF) in starbursts and superwind feedback, and the Bower et al. (2006) model, which uses AGN feedback and a standard IMF.

The morphology-luminosity relation using the morphology indicators provides a nice illustration of how the way in which we select model galaxies can change the relation obtained for different galaxy properties, and hence the need to be consistent when comparing model predictions with observations.

We find that both models predict a morphology-luminosity relation with the correct trend of morphological type with luminosity, from being almost completely disk-dominated at low luminosity to almost entirely bulge-dominated at high luminosity. The Bower et al model better reproduces the overall shape of the luminosity function and the colour bimodality observed in the SDSS data.

When we compare the size-luminosity relations for both models we find that the Baugh et al. model gives a very good match to the observed relation for disk-dominated galaxies, but the Bower et al. model predicts a flat size-luminosity relation. We find that both models fail to reproduce the sizes of bright early-type galaxies.

We gain more insight to the discrepancies between observational data and the models by investigating the sensitivity of the predictions to physical ingredients such as supernova feedback, disk instabilities and the merging process that leads to the formation of the spheroid. This analysis suggests that disk sizes and colours are sensitive to the treatment of gas cooling and SN feedback, while the problem in reproducing spheroids sizes is probably due to the overly simplified prescription used in the models to calculate the sizes of spheroids formed through galaxy mergers.

In the future I want to study in more detail the remnants of galaxy mergers through the use of numerical simulations to improve the recipe used to treat sizes in semi-analytical models.

Another approach that I want to take to test the predictive power of semi-analytical model is to study the evolution of galaxy scaling relations, such as the Tully-Fisher relation and the galaxy sizes-luminosity relation. Simultaneously matching the zero point of Tully-Fisher relation and the normalisation of the luminosity function remains a problem for galaxy formation models.

6.2 High-Redshift Star-Forming Galaxy Populations

In Chapters 4 and 5 we studied the predictions from the Baugh et al. model for two star forming high-redshift galaxy populations, sub-mm galaxies and Lyman-break galaxies. In the standard picture, due to the high star formation rate inferred in sub-mm galaxies (for a standard initial mass function), the sub-mm phase is expected to contribute significantly to the build up of the stellar mass of a galaxy. We find in the model that the descendants of sub-mm galaxies with $S_\nu(850\ \mu\mathrm{m}) > 5$ mJy are typically massive systems (with a median stellar mass of $\sim 2\times10^{11}h^{-1}M_\odot$) and are preferentially bulge-dominated systems. However, when we compute the contribution of the sub-mm phase to the present-day stellar mass we find that only 0.06% of the stellar density is produced by star formation in the SMG phase at $z > 1$. For Lyman-break galaxies, selected with $L_{UV} > L^*_{UV}$ (where L^*_{UV} is the characteristic luminosity at $z = 3$), we find that the descendants of LBGs have a median stellar mass that ranges from $4 \times 10^{10}h^{-1}M_\odot$ (for descendants of $z = 3$ LBGs) to $10^{11}h^{-1}M_\odot$ (for descendants of $z = 6$ LBGs). We find that the model predicts that one in every 16 and one in every 50 Milky Way mass galaxies have a Lyman-break galaxy progenitor at $z = 3$ and $z = 6$ respectively.

We investigated the overlap between SMGs and LBGs. We found that only 2% of LBGs (selected with $L_{UV} > L^*_{UV}$) are predicted to be also SMGs (with $S_\nu(850\ \mu\text{m}) > 5$ mJy), which indicates an important difference between these galaxy populations. This opens a possibility for future research where I can investigate further the connection between these two populations, their clustering properties together with other high-redshift populations like the Lyman-alpha emitter galaxies. By modifying the Bower et al. (2006) model to match the number of sub-mm galaxies (for example by using a top-heavy IMF) we can explore the relation of the star formation in these populations to the presence of active galactic nuclei (AGN).

Over the next decade, new telescopes, such as the Atacama Large Millimeter/Submillimeter Array (ALMA) and the Herschel telescope (launched in May 2009), together with surveys using improved instruments on current telescopes, such as SCUBA-2 on the JMCT telescope, will allow us to exploit the characteristics of the semi-analytical modelling. First, I can combine the semi-analytic model with N-body simulations to produce mock catalogues for these instruments, and second, once the new observations make possible more reliable statistical comparisons, we can use the semi-analytic model to learn more about the importance of different physical ingredients, and improve them.

The ability of ALMA to provide precise images at an angular resolution of 0.1 arcsec will be ideal to test gas simulations for more detailed modelling of dust emission in individual galaxies. Another approach that I could follow is to explore alternative models for the treatment of asymptotic giant branch (AGB) stars in semi-analytical models. The AGB stars treatment can have an effect in the interpretation of high-z population (e.g. Maraston, 2005; Maraston et al., 2006; Tonini et al., 2009).

Appendix A

Dust model

A.1 Simplified two-component model for dust absorption and emission

In order to calculate the sub-mm luminosities and fluxes of model galaxies, we need a model for calculating the amount of stellar radiation absorbed by dust and for the spectral energy distribution (SED) of the radiation emitted by the dust grains. In our previous papers on the dust emission from galaxies (Granato et al., 2000; Baugh et al., 2005; Lacey et al., 2008), we calculated the dust emission by coupling the `GALFORM` code with the `GRASIL` spectrophotometric code, which incorporates a detailed calculation of radiative transfer through the dust distribution and of the heating and cooling of dust grains of different sizes and compositions at different locations within each galaxy. A drawback of the `GRASIL` code is that it typically takes several minutes of CPU time to compute the SED of a single galaxy. For the present paper, it was necessary to calculate the dust emission for very large numbers of `GALFORM` galaxies, for which the computational cost would have been prohibitive if we had used `GRASIL` directly. We therefore devised a simplified approximate model for dust emission at sub-mm wavelengths, which retains some of the main assumptions of `GRASIL`, but is much faster computationally.

We retain the `GRASIL` assumptions about the geometry of the stars and dust: Stars are in general distributed in two components: a spherical bulge with an $r^{1/4}$-law profile, and a flattened component, either a quiescent disk or a burst component, with an exponential radial and vertical profile. We assume that the young stars and dust are found only in the flattened component. We retain the assumption made in `GRASIL` that the dust and gas are in a two-phase medium consisting of dense molecular clouds and a diffuse intercloud medium. Stars are assumed to form inside the molecular clouds, and then to escape into the diffuse medium on a timescale of a few Myr. The calculation of the emission from the dust then has two parts, calculating the amount of energy absorbed in the molecular cloud and diffuse dust components, and then calculating the wavelength distribution of the energy re-emitted by the dust.

A.1.1 Energy absorbed by dust

The unattenuated SED of a stellar population at time t (measured from the big bang) and with a specified IMF is given by an integral over the star formation and metallicity history:

$$L_\lambda^{\mathrm{unatten}}(t) = \int_0^t l_\lambda(\tau)\Psi(t-\tau, Z)\mathrm{d}\tau\mathrm{d}Z, \tag{A.1}$$

where L_λ is the luminosity per unit wavelength for the composite stellar population, $l_\lambda(\tau, Z)$ is the luminosity per unit wavelength for a simple stellar population (SSP) with the specified IMF of age τ and metallicity Z and unit initial mass, and $\Psi(t, Z)\,\mathrm{d}t\,\mathrm{d}Z$ is the mass of stars formed in the time interval $t, t+\mathrm{d}t$ and metallicity range $Z+\mathrm{d}Z$. The SED including dust attenuation is then

$$L_\lambda^{\mathrm{atten}}(t) = A_\lambda^{(\mathrm{diff})} \int_0^t A_\lambda^{(\mathrm{MC})}(\tau) l_\lambda(\tau, Z)\Psi(t-\tau, Z)\mathrm{d}\tau\mathrm{d}Z, \tag{A.2}$$

where $A_\lambda^{(\mathrm{diff})}$ is the dust attenuation factor at wavelength λ due to the diffuse dust component, and $A_\lambda^{(\mathrm{MC})}(\tau)$ is the mean attenuation due to molecular clouds, which depends on stellar age. The attenuation by diffuse dust is independent of stellar age, since we assume that the spatial distribution of stars after they escape from their parent molecular clouds is independent of stellar age.

A.1.1.1 Dust attenuation by clouds

Following the assumptions made in `GRASIL`, we assume that a fraction f_c of the total gas mass is in molecular clouds, which are modelled as uniform density spheres of gas mass m_c and radius r_c. The effective absorption optical depth for the stars in each cloud is approximated as

$$\tau_{\lambda,\mathrm{eff}} = (1-a_\lambda)^{1/2}\tau_{\lambda,\mathrm{ext}} \tag{A.3}$$

(e.g. Silva et al., 1998), where a_λ is the albedo, and $\tau_{\lambda,\mathrm{ext}}$ is the extinction optical depth from the centre of a cloud to its edge. The extinction optical depth is calculated from the column density of gas through a cloud and its metallicity (taken equal to the mean ISM metallicity Z_g), assuming the same extinction curve shape as in `GRASIL` (which reproduces that in the local ISM), with a dust-to-gas ratio proportional to Z_g and equal to the local ISM value for solar metallicity $Z_\odot = 0.02$. The dust attenuation factor for light from stars in a single cloud is then $e^{-\tau_{\lambda,\mathrm{eff}}}$, while the mean attenuation for all stars of age τ due to clouds is given by

$$A_\lambda^{(\mathrm{MC})}(\tau) = \eta(\tau)e^{-\tau_{\lambda,\mathrm{eff}}} + (1-\eta(\tau)), \tag{A.4}$$

where $\eta(\tau)$ is defined as the fraction of stars of age τ which are still in the clouds where they formed. For this fraction, we adopt the same dependence as assumed in `GRASIL`,

$$\eta(\tau) = \begin{cases} 1 & \tau < t_{\mathrm{esc}} \\ 2 - t/t_{\mathrm{esc}} & t_{\mathrm{esc}} < \tau < 2t_{\mathrm{esc}} \\ 0 & \tau > 2t_{\mathrm{esc}} \end{cases} \tag{A.5}$$

so that stars begin to escape a time t_{esc} after they form, and have all escaped after time $2t_{\mathrm{esc}}$.

The dust-attenuated SED can therefore be rewritten as

$$L_\lambda^{\mathrm{atten}}(t) = A_\lambda^{(\mathrm{diff})}\langle\, A_\lambda^{(\mathrm{MC})}(\tau)\rangle\, L_\lambda^{\mathrm{unatten}}(t) \tag{A.6}$$

where $A_\lambda^{(\mathrm{MC})}(\tau)\rangle$ is the dust attenuation by clouds averaged over all stellar ages, given by

$$\langle A_\lambda^{(\mathrm{MC})}(\tau)\rangle = 1 - \langle\eta(\tau)\rangle_\lambda(1 - e^{-\tau_{\lambda,\mathrm{eff}}}) \tag{A.7}$$

and $\langle\eta(\tau)\rangle_\lambda$ is the fraction of starlight at wavelength λ emitted by stars inside molecular clouds. This is in turn given by a luminosity-weighted average

$$\langle\eta(\tau)\rangle_\lambda = \frac{\int_0^t \eta(\tau) l_\lambda(\tau, Z)\Psi(t-\tau, Z)\mathrm{d}\tau\mathrm{d}Z}{\int_0^t l_\lambda(\tau, Z)\Psi(t-\tau, Z)\mathrm{d}\tau\mathrm{d}Z} \tag{A.8}$$

In principle, in order to calculate $\langle\eta(\tau)\rangle_\lambda$ we need to know the entire star formation and chemical enrichment history for a galaxy, specified by $\Psi(\tau, Z)$. However, we now make a number of simplifying approximations. The absorption of starlight by dust in clouds is important mostly for the UV light, which is emitted mainly by young stars, which have metallicities close to the current ISM value Z_g. We can therefore approximate the integral in eqn.(A.8) as

$$\langle\eta(\tau)\rangle_\lambda \approx \frac{\int_0^T \eta(\tau) l_\lambda(\tau, Z_g)\psi(t-\tau)\mathrm{d}\tau}{\int_0^T l_\lambda(\tau, Z_g)\psi(t-\tau)\mathrm{d}\tau} \tag{A.9}$$

where $\psi(t)$ is now the total SFR at time t, integrated over all stellar metallicities, and T is a fixed upper cutoff in the integral over stellar age. We adopt $T = 10\mathrm{Gyr}$, but our results are not sensitive to this value.

We treat the evaluation of eqn.(A.9) separately for star formation in disks and in bursts. For disks, the SFR typically varies on a timescale long compared to the lifetimes of the stars responsible for most of the UV radiation which dominates the dust heating, so we approximate the recent SFR as constant, $\psi^{\rm disk}(t-\tau) \approx \psi^{\rm disk}(t)$, leading to

$$\langle \eta(\tau) \rangle_{\lambda}^{\rm disk} \approx \frac{\int_0^T \eta(\tau) l_{\lambda}^{\rm disk}(\tau, Z_g) {\rm d}\tau}{\int_0^T l_{\lambda}^{\rm disk}(\tau, Z_g) {\rm d}\tau}, \tag{A.10}$$

where the SSPs $l_{\lambda}^{\rm disk}(\tau, Z_g)$ use the IMF for quiescent star formation. In the case of a burst starting at time t_b, with e-folding timescale τ_* the SFR varies as

$$\psi^{\rm burst}(t) = \begin{cases} 0 & t < t_b \\ \psi_0^{\rm burst} \exp(-(t-t_b)/\tau_*) & t > t_b \end{cases} \tag{A.11}$$

so that eqn.(A.9) can be rewritten as

$$\langle \eta(\tau) \rangle_{\lambda}^{\rm burst} \approx \frac{\int_0^{\tau_b} \eta(\tau) l_{\lambda}^{\rm burst}(\tau, Z_g) e^{\tau/\tau_*} {\rm d}\tau}{\int_0^{\tau_b} l_{\lambda}^{\rm burst}(\tau, Z_{\rm g})) e^{\tau/\tau_*} {\rm d}\tau} \tag{A.12}$$

where the SSPs $l_{\lambda}^{\rm burst}(\tau, Z_g)$ use the IMF for bursts, and we define $\tau_b = t - t_b$ as the age at which the burst started. In practice, we tabulate both functions $\langle \eta(\tau) \rangle_{\lambda}^{\rm disk}$ and $\langle \eta(\tau) \rangle_{\lambda}^{\rm burst}$ as functions of Z_g and (Z_g, τ_*, τ_b) respectively.

Finally, we calculate the luminosity absorbed by dust in molecular clouds as

$$L_{\rm abs}^{MC} = \int_0^{\infty} (1 - \langle A_{\lambda}^{\rm (MC)} \rangle) L_{\lambda}^{\rm unatten} {\rm d}\lambda \tag{A.13}$$

The parameters we use for the molecular clouds are identical to those which we use in `GRASIL`. For the current model, they are: $f_{\rm c} = 0.25$, $m_{\rm c} = 10^6 M_{\odot}$, $r_{\rm c} = 16{\rm pc}$, $t_{\rm esc} = 1{\rm Myr}$ for both disks and bursts (Baugh et al., 2005). (In fact, $m_{\rm c}$ and $r_{\rm c}$ only enter in the combination $m_{\rm c}/r_{\rm c}^2$, which determines the optical depth of the molecular clouds). We note that the `GRASIL` code does not make any of the above approximations, but instead does an exact radiative transfer calculation for the escape of starlight from molecular clouds.

A.1.1.2 Dust attenuation by diffuse medium

We calculate the attenuation of starlight by dust in the diffuse medium using the tabulated radiative transfer models of Ferrara et al. (1999), as described in Cole et al. (2000). Ferrara et al. calculated dust attenuation factors using a Monte Carlo radiative transfer code, including both absorption and scattering, for galaxies containing stars in both a disk and bulge, with the dust smoothly distributed in a disk, and tabulated the results as functions of wavelength, disk inclination angle, central ($r = 0$) dust optical depth, and ratio of disk to bulge scalelengths. We use their models for a Milky Way extinction curve, equal scaleheights for dust and gas, and ratio of vertical to radial disk scalelengths equal to 0.1. We compute the central optical depth for our model galaxies from the mass and metallicity of the gas and the radial scalelength of the disk, assuming that the dust-to-gas ratio is proportional to the gas metallicity, and then interpolate in the Ferrara et al. tables to get the total attenuation as a function of wavelength. The only difference from Cole et al. (2000) is that in the present case the diffuse medium contains only a fraction $1 - f_{\rm c}$ of the total gas mass.

The luminosity absorbed by dust in the diffuse medium is then calculated as

$$L_{\rm abs}^{\rm diff} = \int_0^\infty (1 - A_\lambda^{\rm (diff)})\langle A_\lambda^{\rm (MC)}\rangle L_\lambda^{\rm unatten} {\rm d}\lambda \tag{A.14}$$

A.1.2 SED of dust emission

The dust is assumed to be in thermal equilibrium, so the total luminosity emitted by dust is equal to the luminosity absorbed from starlight. To calculate the wavelength distribution of the dust emission, we approximate the dust temperature as being constant within each of the dust components, i.e. for each galaxy, we have a single temperature for the dust in molecular clouds, and a single (but different) temperature for dust in the diffuse medium. This is a major simplification compared to what is done in `GRASIL`, where the dust temperature varies with location in the galaxy according to the strength of the stellar radiation field, and also depending on the size and composition of each dust grain. (`GRASIL` assumes a distribution of grain sizes, and also two compositions, carbonaceous and silicate, and in addition includes Polycyclic Aromatic Hydrocarbon (PAH) molecules.) Furthermore, `GRASIL` includes the effects of temperature fluctuations in small grains and PAH molecules, unlike our simplified model. For a medium in thermal equilibrium at temperature T, the emissivity ϵ_λ (defined as the luminosity emitted per unit wavelength per unit mass) can be written as (e.g. Rybicki and Lightman, 1979)

$$\epsilon_\lambda = 4\pi\kappa_{\rm d}(\lambda)B_\lambda(T_{\rm d}) \tag{A.15}$$

where $\kappa_{\rm d}(\lambda)$ is the absorption opacity (absorption cross-section per unit mass), and $B_\lambda(T_{\rm d})$ is the Planck blackbody function $B_\lambda(T_{\rm d}) = (2hc^2/\lambda^5)/(\exp(hc/\lambda kT_{\rm d}) - 1)$. Since we assume throughout that the dust-to-gas ratio is proportional to the gas metallicity, it is convenient to define the opacity relative to the total mass of metals in the gas (whether in dust grains or not). Assuming that the galaxy is optically thin at the wavelengths at which the dust emits, we can then write the luminosity per unit wavelength emitted by dust as

$$L_{\lambda}^{dust} = 4\pi\kappa_{\rm d}(\lambda)B_{\lambda}(T_{\rm d})Z_{\rm gas}M_{\rm gas}. \tag{A.16}$$

This equation must be applied separately to the dust in the molecular clouds and in the diffuse medium, since they have different temperatures. (In contrast, in `GRASIL`, the calculation of dust emission from clouds includes optical depth effects.) We calculate the dust temperatures for the clouds and diffuse medium by equating the luminosity of dust emission (integrated over all wavelengths) to the luminosity absorbed from starlight.

In order to calculate eqn.(A.16), we need to know the dust opacity $\kappa_{\rm d}$ as a function of wavelength. We assume the same values as for the dust model used in `GRASIL`, but since the dust emission is at long wavelengths, we approximate this by a power-law when we calculate the emission. We find that in the `GRASIL` dust model for the local ISM (with metallicity $Z = 0.02$), the absorption opacity per unit mass of metals at $\lambda > 30\mu$m can be approximated as $\kappa_{\rm d} = 140{\rm cm}^2{\rm g}^{-1}(\lambda/30\mu{\rm m})^{-2}$. However, (Silva et al., 1998) found that for the ultraluminous starburst galaxy Arp 220, the observed sub-mm SED was reproduced better by `GRASIL` if the dust emissivity at very long wavelengths was modified by introducing a break to a $\lambda^{-1.6}$ power-law at $\lambda > 100\mu$m, and the same modification was adopted by Baugh et al. (2005) when modelling SMGs using `GRASIL`. We therefore describe the dust emissivity in our model by a broken power-law:

$$\kappa_{\rm d}(\lambda) = \begin{cases} \kappa_1 \left(\frac{\lambda}{\lambda_1}\right)^{-2} & \lambda < \lambda_{\rm b} \\ \kappa_1 \left(\frac{\lambda_{\rm b}}{\lambda_1}\right)^{-2} \left(\frac{\lambda}{\lambda_{\rm b}}\right)^{-\beta_b} & \lambda > \lambda_{\rm b} \end{cases} \tag{A.17}$$

where $\kappa_1 = 140{\rm cm}^2{\rm g}^{-1}$ at the reference wavelength of $\lambda_1 = 30\mu$m, and the power-law breaks to a slope β_b longwards of wavelength $\lambda_{\rm b}$. We adopt $\lambda_{\rm b} = 100\mu$m and $\beta_b = 1.6$ in bursts, and $\lambda_{\rm b} = \infty$ (i.e. an unbroken power-law) in quiescent disks.

A.1.3 Comparison between two-temperature dust model and `GRASIL`

We test the accuracy and range of validity of our simplified two-temperature model for dust emission by comparing with galaxy IR SEDs calculated using the full `GRASIL` model. The comparison sample was run using halo merger trees from the Millennium N-body simulation, which has slightly different cosmological parameters from those used in the main part of this paper. However, this does not affect the validity of our SED comparison, since we compare IR luminosities and luminosity functions computed from exactly the same set of model galaxies using the two methods (two-temperature model vs `GRASIL`). The comparison sample includes both quiescent and bursting galaxies. For completeness, and to assist in future work, we include the entire mid-IR to sub-mm wavelength range in our comparison. The wavelengths we use are 24, 70, 100, 250, 450 and 850 μm, measured in the galaxy rest-frame in all cases. In the case of `GRASIL`, the luminosities L_ν were computed through the following broad-band filters: *Spitzer* at 24 μm, *Herschel* at 70, 100 and 250 μm, and *SCUBA* at 450 and 850 μm. For the two-temperature model, we instead computed simple monochromatic luminosities.

We first make a galaxy-by-galaxy comparison[1] between the luminosities calculated using the two methods. This is shown for $z = 0$ in Fig. A.1 and for $z = 2$ in Fig. A.2. The greyscale density in these plots represents the galaxy number density. The diagonal line in each panel corresponds to perfect agreement between the two methods. We see that at long wavelengths ($\lambda_{\rm rest} \gtrsim 100\mu$m) there is very good agreement between the two methods, with little scatter and only slight systematic deviations from the line of equality. Moving down in wavelength, the differences start to become significant at $\lambda_{\rm rest} = 70\mu$m, with systematic deviations at low luminosities, and increased scatter. At 24μm, the two-temperature model breaks down catastrophically, predicting luminosities many orders of magnitude lower than the `GRASIL` values. This breakdown is to be expected, since the mid-IR emission is dominated by the small fraction of dust grains having much warmer temperatures than the average for the galaxy. These warm dust temperatures can be caused by the grains being close to luminous young stars in molecular clouds, or by very small grains and PAH molecules undergoing large temperature fluctuations. In addition, much of the PAH emission is in narrow bands. The `GRASIL` model includes all of these effects, but our simple two-temperature model does not. (The two-temperature model does allow the molecular clouds to have to higher a dust temperature than the diffuse medium, but it imposes a uniform temperature within the clouds, which does not allow for the fact that regions of a cloud closer to young stars get more strongly heated. The two-temperature model does not include PAH molecules.)

We next compare the galaxy luminosity functions between the two methods for the same set of rest-frame wavelengths and the same redshifts, $z = 0$ in Fig. A.3 and $z = 2$ in Fig. A.4. We see that at the longer wavelengths ($\lambda_{\rm rest} \gtrsim 100\mu$m), the agreement is generally very good between the two methods, although at rest-frame wavelengths of 450 and 850μm there seem to be some systematic deviations at the highest luminosities. On the other hand, at a rest-frame wavelength of 24μm, the two-temperature model fails

---

[1] The comparison plots were generated for this appendix by Cesario Almeida. They will be included in Lacey et al. (2010, in preparation).

completely, underestimating the galaxy number density by factors $\sim 10 - 100$. For the present paper, we are primarily interested in emission at an *observed* wavelength of 850μm from SMGs at typical redshifts $z \sim 2$, which corresponds to a *rest-frame* wavelength $\sim 300\mu$m. At these wavelengths, the luminosity function predicted by our simple two-temperature model is seen to be in excellent agreement with the full `GRASIL` calculation.

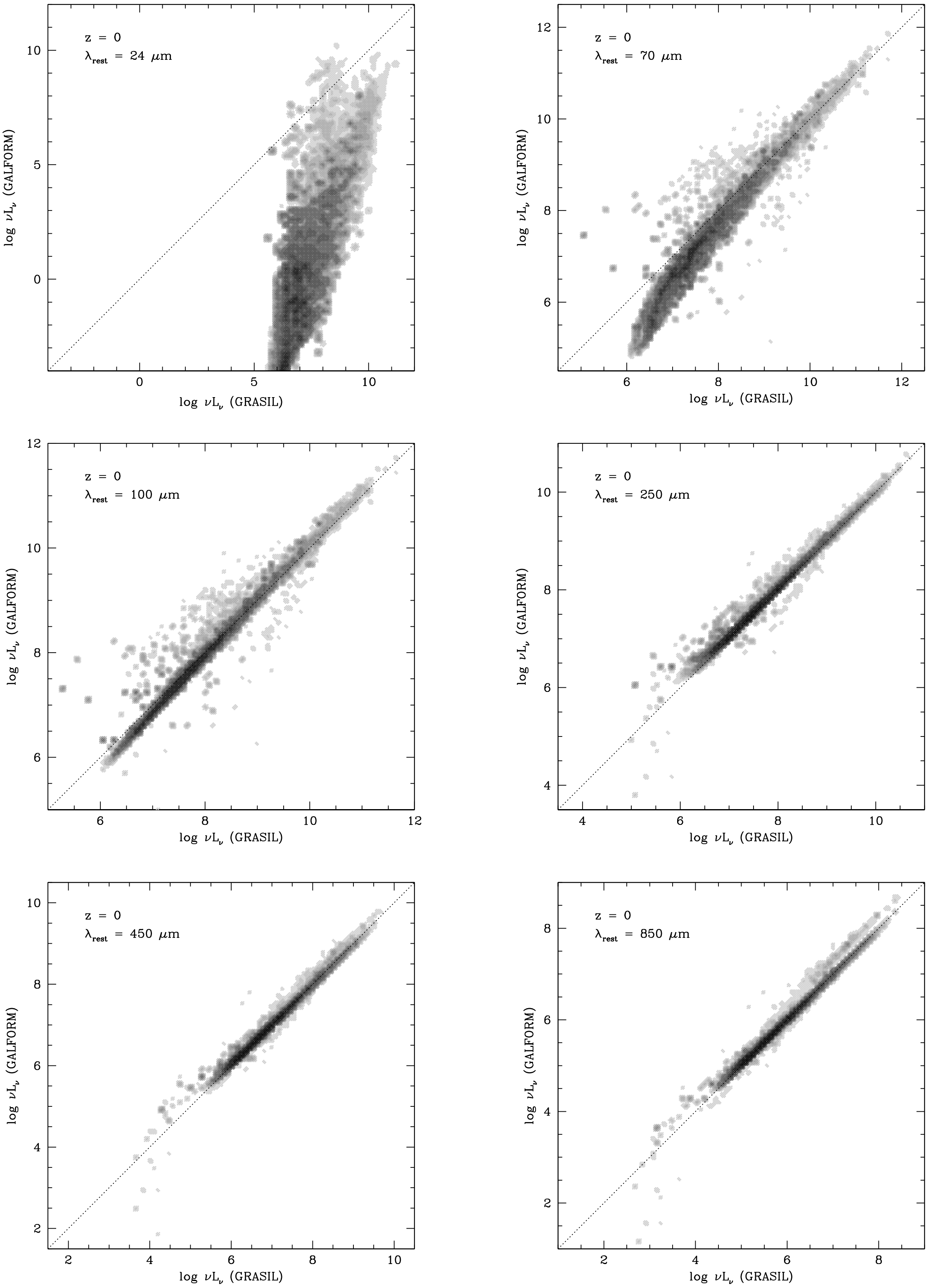

Figure A.1: Galaxy-by-galaxy comparison of IR luminosities between the two-temperature dust emission model (labelled `GALFORM`) and `GRASIL` for $z = 0$. The greyscale indicates the galaxy number density. Comparisons are shown for the following rest-frame wavelengths: (a) 24 μm; (b) 70 μm; (c) 100 μm; (d) 250 μm; (e) 450 μm; (f) 850 μm.

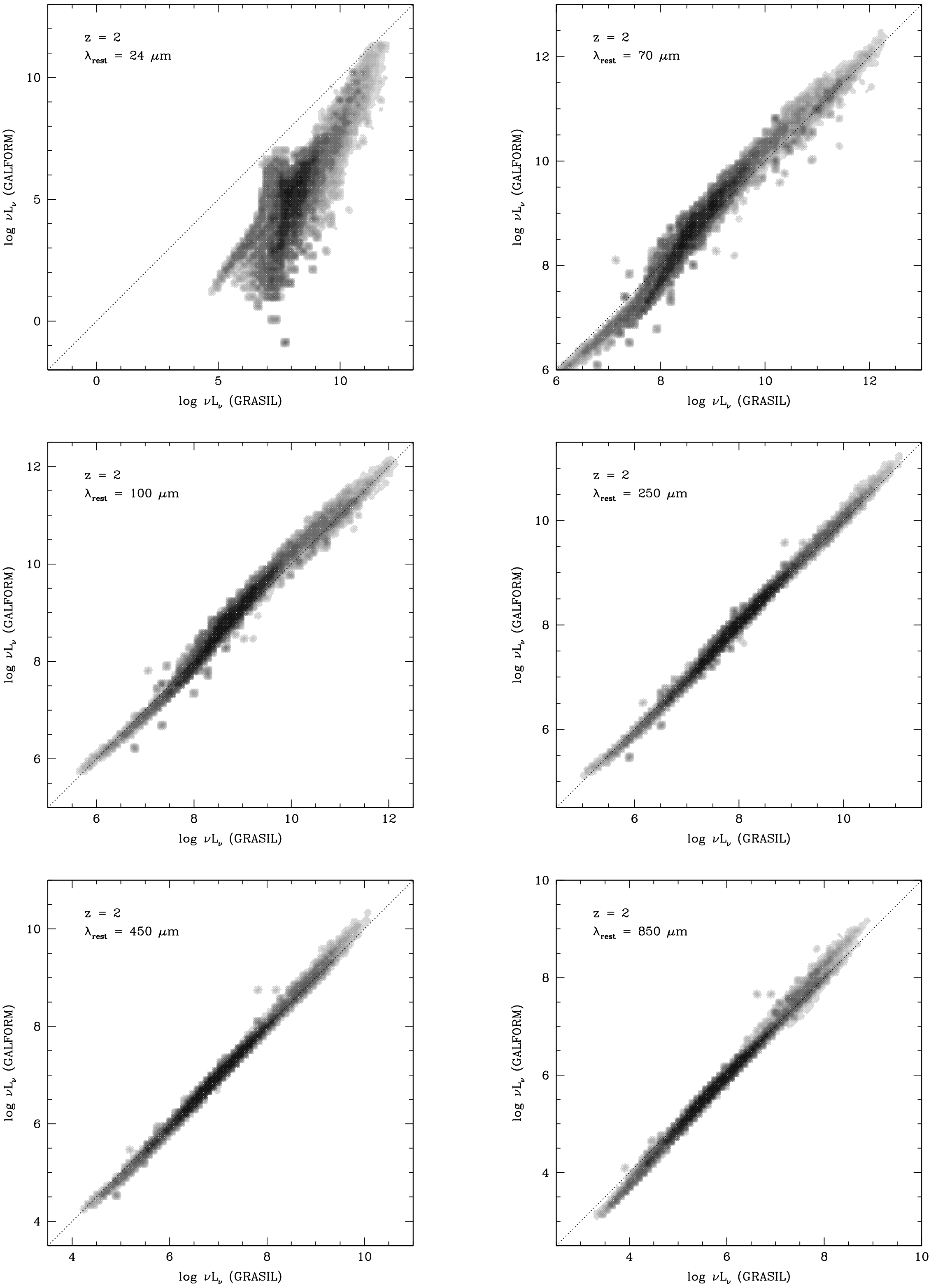

Figure A.2: Galaxy-by-galaxy comparison of IR luminosities between the two-temperature dust emission model (labelled `GALFORM`) and `GRASIL` for $z = 2$. The greyscale indicates the galaxy number density. Comparisons are shown for the following rest-frame wavelengths: (a) 24 μm; (b) 70 μm; (c) 100 μm; (d) 250 μm; (e) 450 μm; (f) 850 μm.

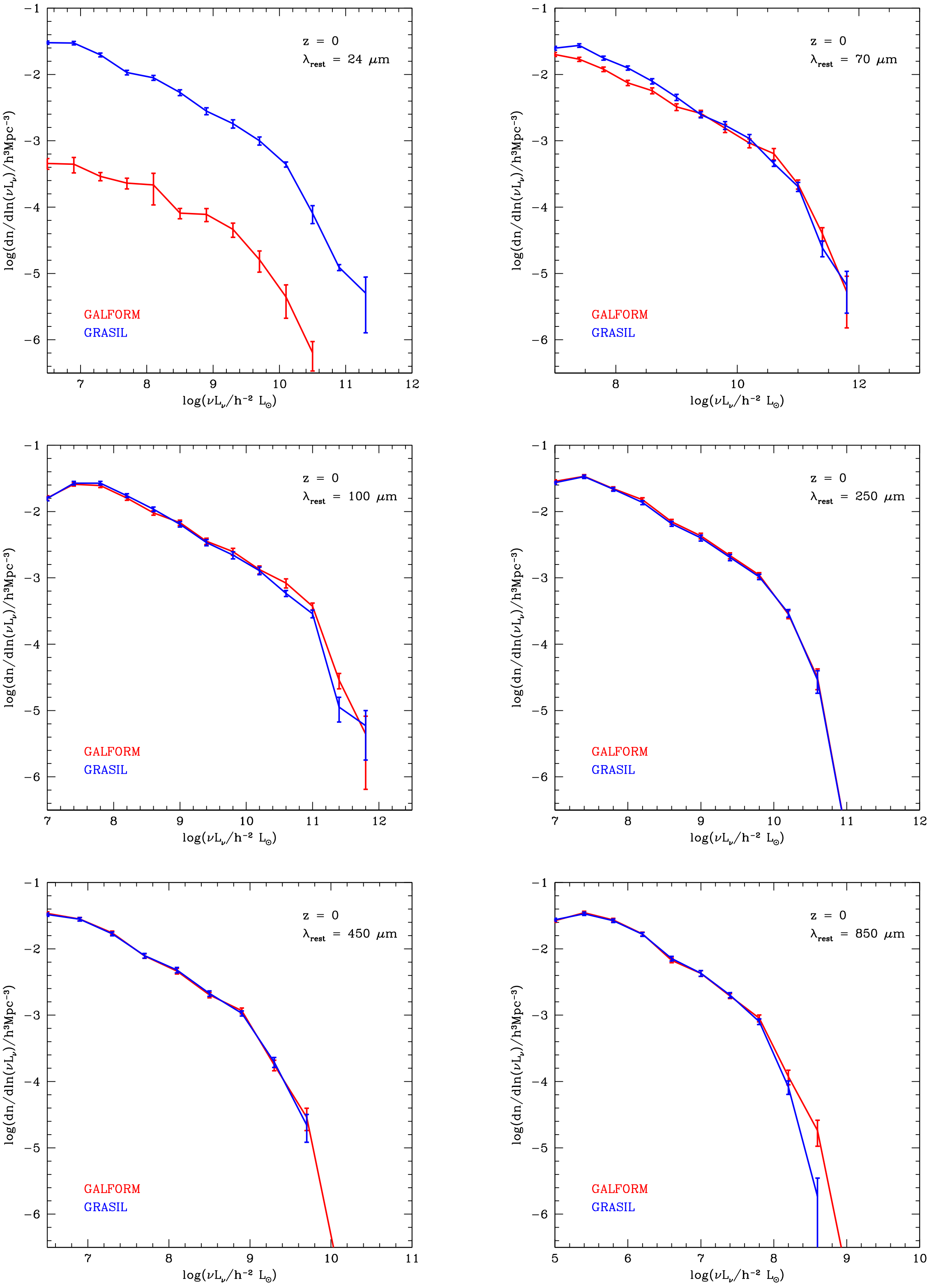

Figure A.3: Comparison of galaxy IR luminosity functions between the two-temperature dust emission model (red curves, labelled `GALFORM`) and `GRASIL` (blue curves) for $z = 0$. Comparisons are shown for the following rest-frame wavelengths: (a) 24 μm; (b) 70 μm; (c) 100 μm; (d) 250 μm; (e) 450 μm; (f) 850 μm. The error bars indicate the model uncertainties due to the finite number of objects in the model galaxy sample.

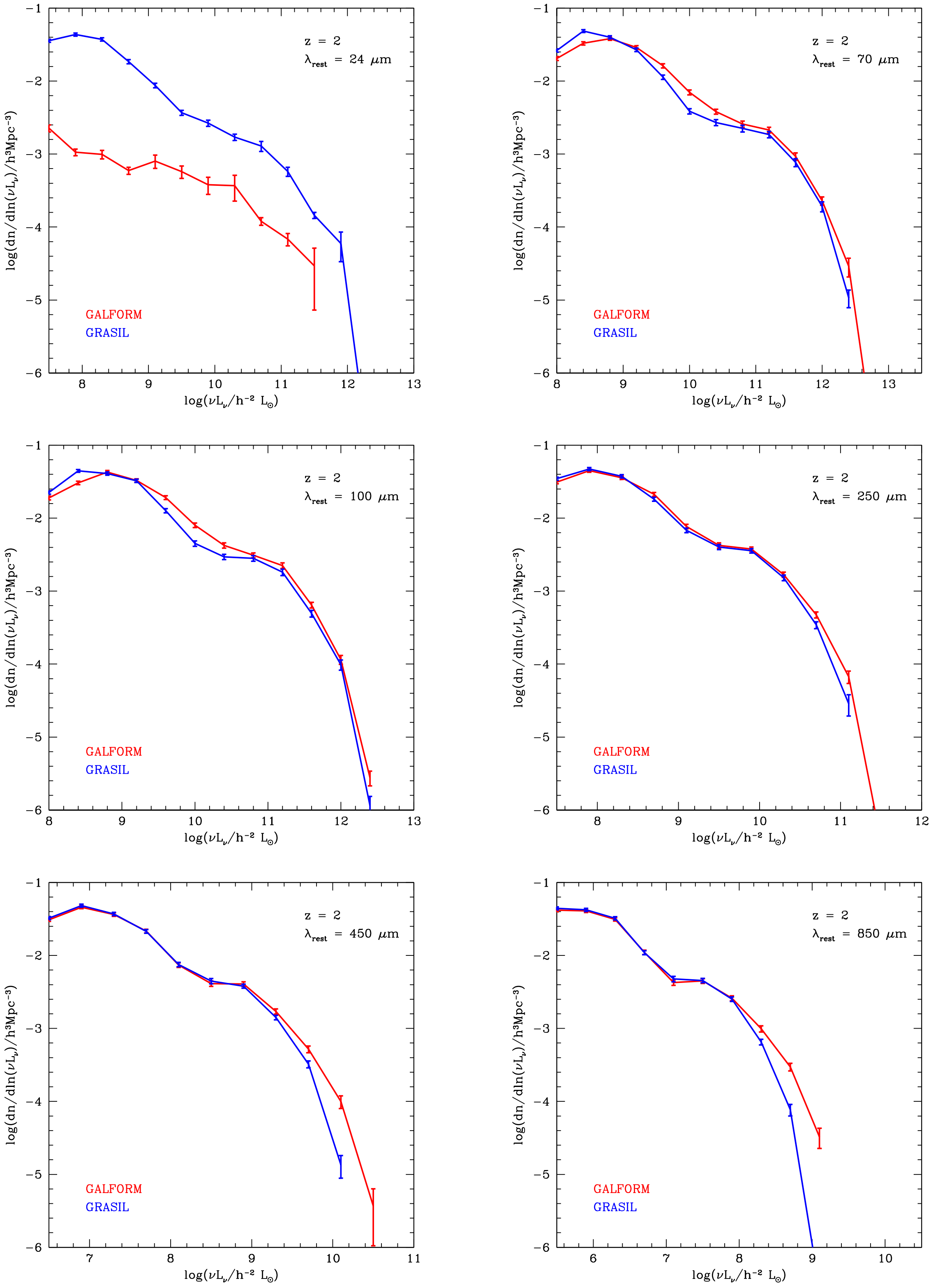

Figure A.4: Comparison of galaxy IR luminosity functions between the two-temperature dust emission model (red curves, labelled `GALFORM`) and `GRASIL` (blue curves) for $z = 2$. Comparisons are shown for the following rest-frame wavelengths: (a) 24 μm; (b) 70 μm; (c) 100 μm; (d) 250 μm; (e) 450 μm; (f) 850 μm.

Appendix B

Change in the SDSS photometric properties and comparison between different indicators of galaxy morphology

B.1 Changes in the photometry of SDSS galaxies from DR1 to DR4

The photometric and spectroscopic pipelines for processing SDSS data have been refined on subsequent data releases, particularly between DR1 and DR2. In DR2, all the SDSS data was re-analyzed to apply improvements to the processing of images (magnitude modelling, image deblending) and spectra (extraction of radial velocities, spectrophotometry). It is instructive to test whether any of the photometric properties used in this paper to constrain the models have changed appreciably between data releases. Uncertainty in the extraction of properties from observational data puts a limit on how well we can expect the models to reproduce the observational results. In this appendix, we compare galaxy sizes, Petrosian magnitudes and Sérsic index values between DR1 and DR4.

To perform the comparison between measurements in different data releases, we need to be sure that we are looking at the same galaxy in each version of the catalogue. This is not a trivial exercise, since revisions to the algorithm used to deblend close or merged images mean that a single object in DR1 could appear as multiple objects in DR4. The match is made by requiring that a DR4 galaxy should be closer than $1.2''$ to a DR1 galaxy on the sky (which is equivalent to 3 SDSS pixels, each of $0.396''$). This is close to the

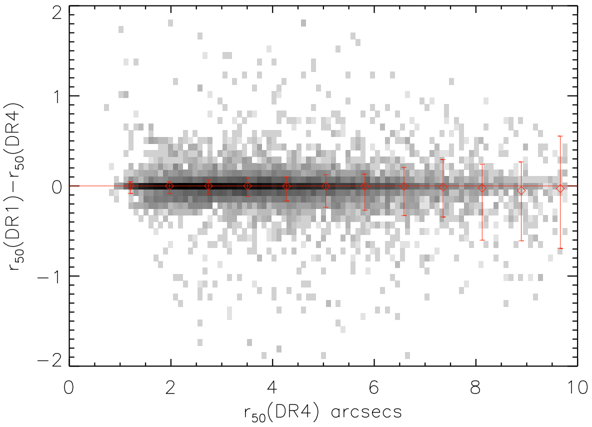

Figure B.1: The difference in angular radius (in arcsec) enclosing 50% of the Petrosian magnitude, r_{50}, between the same galaxies identified in DR1 and DR4. The shading reflects the logarithm of the density of galaxies. The points show the median difference in size and the bars show the 10-90 percentile range of this distribution.

smallest angular size found for galaxies used in the comparison. With this criteria, we were able to find DR4 counterparts for 95% of the galaxies from DR1.

We first look at the difference in the value of angular radius enclosing 50% of the Petrosian light, which is plotted in Fig. B.1 for galaxies with $z < 0.05$. Here we plot the logarithm of the number density of galaxies in greyscale to expand the dynamic range of the shading. The points with error bars show the median difference in size between the two data releases, with the bars showing the 10-90 percentile range of the distribution. Although there is scatter in the sizes between data releases, there is no evidence for any systematic differences.

Next we repeat this comparison for the Petrosian magnitude, which is shown in Fig. B.2 for galaxies with $z < 0.05$. In this case there is a small systematic effect, with the median shift being -0.04 mag between DR1 and DR4 i.e. a galaxy is typically brighter in DR1 and it appears in DR4.

Finally we compare the Sérsic index between DR1 and DR4. For DR1, we use the Sérsic index calculated by Blanton et al. (2003). The analysis presented by these authors corresponds to a larger area than DR1, but relies on a pre-DR1 version of the photometric analysis software. In a subsequent publication, (Blanton et al., 2005b), the algorithm used to compute the Sérsic index was updated in order to account for a bias in the results.

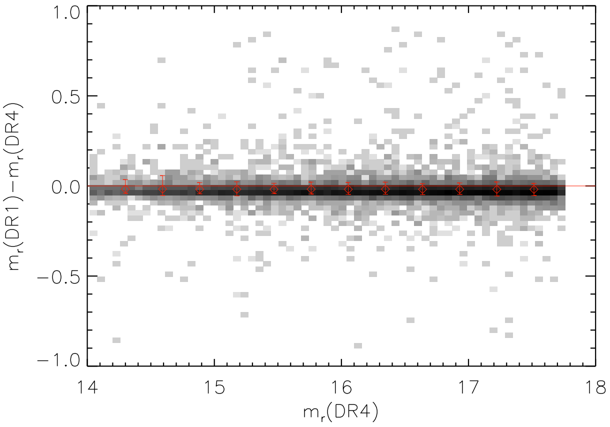

Figure B.2: The difference in the Petrosian magnitude recorded in DR1 and DR4 for a matched sample of galaxies. The shading and symbols have the same meaning as in Fig. B.1.

(Blanton et al., 2005b) demonstrated this effect by feeding a pure bulge with $n = 4$ into the algorithm. With the original method, a Sérsic index of $n = 2.7$ was recovered. Using the improved algorithm, the result was increased to $n = 3.5$, a much smaller bias. The comparison between the Sérsic index in DR1 and DR4 is plotted in Fig. B.3.The DR4 Sérsic index is generally larger than in DR1, particularly for $n > 1$. The revised algorithm sometimes fails to find a suitable value for n, in which case $n = 6$ was assigned. This comparison shows the difficulty in extracting the value of the Sérsic index for galaxies, and gives an indication of how closely we should expect the models to agree with the observational results.

B.2 The correlation between Sérsic index and bulge to total luminosity ratio.

In Section 3, we compared different indicators of galaxy morphology, the concentration, Sérsic index and bulge-to-total luminosity ratio using the output of `GALFORM`. We found considerable scatter between these quantities, particularly in the Sérsic index - bulge-to-total ratio plane. This is driven by the ratio of the disk and bulge scale-lengths; galaxies with a given ratio of scale-lengths occupy a particular locus in the plane.

We can now repeat this comparison for SDSS galaxies. Benson et al. (2007) calculated the disk and bulge radii (r_d and r_b) and bulge-to-total luminosity ratio, B/T, for a sample of galaxies from the SDSS EDR. In Fig. B.4 we plot the raw uncorrected values of B/T

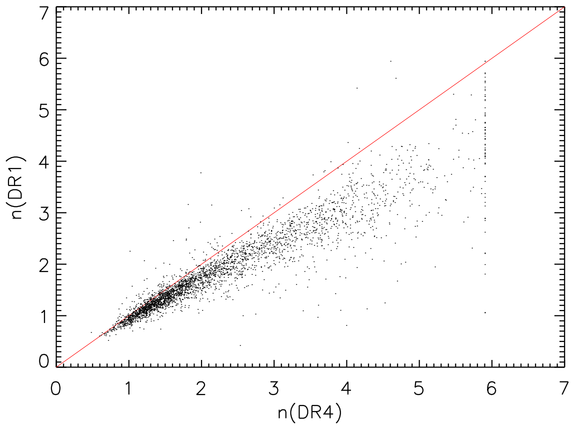

Figure B.3: The Sérsic index in DR1 plotted against that measured for the same galaxy in DR4. The shading and symbols have the same meaning as in Fig. B.1.

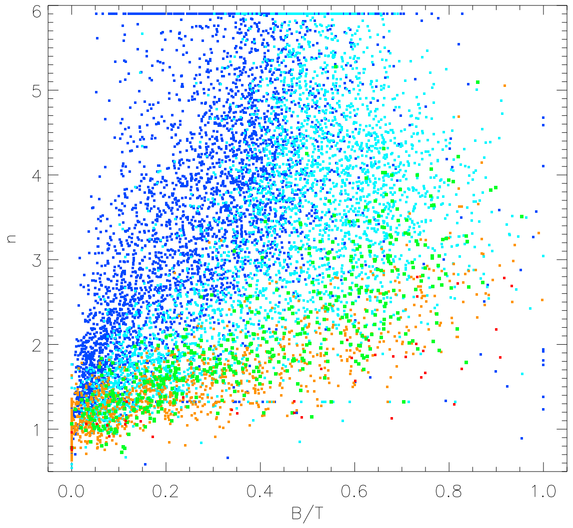

Figure B.4: The Sérsic index extracted from the NYU-VAGC plotted against the bulge-to-total luminosity ratio (B/T) as determined by Benson et al. (2007). The colour coding reflects the ratio of the disk and bulge radii, which blue indicating a ratio of $r_{\mathrm{d}}/r_{\mathrm{b}} = 4$ and red indicating $r_{\mathrm{d}}/r_{\mathrm{b}} = 0.25$, as in Fig. 3.

found by Benson et al. (2007) against the Sérsic index n for these galaxies given by the NYU-VAGC used in this paper. The galaxies are colour-coded in the same way as for the `GALFORM` sample plotted in Fig. 3.3; the largest ratio of disk to bulge radii is shown by blue points and the smallest ratio by red points. This plot looks qualitatively similar to the one obtained in Section 3 using `GALFORM` output, but with much more scatter. As found by Benson et al., there is a deficit of galaxies with high B/T.

Bibliography

K. L. Adelberger and C. C. Steidel. ApJ, 544:218–241, November 2000.

J. K. Adelman-McCarthy, M. A. Agüeros, S. S. Allam, C. Allende Prieto, K. S. J. Anderson, S. F. Anderson, J. Annis, N. A. Bahcall, C. A. L. Bailer-Jones, I. K. Baldry, J. C. Barentine, B. A. Bassett, A. C. Becker, T. C. Beers, E. F. Bell, A. A. Berlind, M. Bernardi, M. R. Blanton, J. J. Bochanski, W. N. Boroski, J. Brinchmann, J. Brinkmann, R. J. Brunner, T. Budavári, S. Carliles, M. A. Carr, F. J. Castander, D. Cinabro, R. J. Cool, K. R. Covey, I. Csabai, C. E. Cunha, J. R. A. Davenport, B. Dilday, M. Doi, D. J. Eisenstein, M. L. Evans, X. Fan, D. P. Finkbeiner, S. D. Friedman, J. A. Frieman, M. Fukugita, B. T. Gänsicke, E. Gates, B. Gillespie, K. Glazebrook, J. Gray, E. K. Grebel, J. E. Gunn, V. K. Gurbani, P. B. Hall, P. Harding, M. Harvanek, S. L. Hawley, J. Hayes, T. M. Heckman, J. S. Hendry, R. B. Hindsley, C. M. Hirata, C. J. Hogan, and D. W. Hogg, et al. ApJS, 175:297–313, April 2008.

C. Almeida, C. M. Baugh, and C. G. Lacey. MNRAS, 376:1711–1726, April 2007.

C. Almeida, C. M. Baugh, and C. G. Lacey, and C. S. Frenk, and G. L. Granato, and L. Silva, and A. Bressan. MNRAS, 402:544-564, April 2010.

I. K. Baldry, K. Glazebrook, J. Brinkmann, Ž. Ivezić, R. H. Lupton, R. C. Nichol, and A. S. Szalay. ApJ, 600:681–694, January 2004.

C. M. Baugh. *Reports on Progress in Physics*, 69:3101–3156, December 2006.

C. M. Baugh, S. Cole, and C. S. Frenk. MNRAS, 283:1361, December 1996.

C. M. Baugh, S. Cole, C. S. Frenk, and C. G. Lacey. ApJ, 498:504, May 1998.

C. M. Baugh, A. J. Benson, S. Cole, C. S. Frenk, and C. G. Lacey. MNRAS, 305:L21, May 1999.

C. M. Baugh, C. G. Lacey, C. S. Frenk, G. L. Granato, L. Silva, A. Bressan, A. J. Benson, and S. Cole. MNRAS, 356:1191–1200, January 2005.

C. L. Bennett, A. J. Banday, K. M. Gorski, G. Hinshaw, P. Jackson, P. Keegstra, A. Kogut, G. F. Smoot, D. T. Wilkinson, and E. L. Wright. ApJ, 464:L1, June 1996.

A. J. Benson, R. G. Bower, C. S. Frenk, C. G. Lacey, C. M. Baugh, and S. Cole. ApJ, 599:38–49, December 2003.

A. J. Benson, D. Džanović, C. S. Frenk, and R. Sharples. MNRAS, 379:841–866, August 2007.

M. A. Bershady, A. Jangren, and C. J. Conselice. AJ, 119:2645–2663, June 2000.

J. Binney. ApJ, 215:483, July 1977.

J. Binney and S. Tremaine. *Galactic Dynamics: Second Edition*. Princeton University Press, 2008.

A. W. Blain, I. Smail, R. J. Ivison, J.-P. Kneib, and D. T. Frayer. Phys. Rep., 369: 111–176, October 2002.

M. R. Blanton, D. W. Hogg, N. A. Bahcall, I. K. Baldry, J. Brinkmann, I. Csabai, D. Eisenstein, M. Fukugita, J. E. Gunn, Ž. Ivezić, D. Q. Lamb, R. H. Lupton, J. Loveday, J. A. Munn, R. C. Nichol, S. Okamura, D. J. Schlegel, K. Shimasaku, M. A. Strauss, M. S. Vogeley, and D. H. Weinberg. ApJ, 594:186–207, September 2003.

M. R. Blanton, R. H. Lupton, D. J. Schlegel, M. A. Strauss, J. Brinkmann, M. Fukugita, and J. Loveday. ApJ, 631:208–230, September 2005a.

M. R. Blanton, D. J. Schlegel, M. A. Strauss, J. Brinkmann, D. Finkbeiner, M. Fukugita, J. E. Gunn, D. W. Hogg, Ž. Ivezić, G. R. Knapp, R. H. Lupton, J. A. Munn, D. P. Schneider, M. Tegmark, and I. Zehavi. AJ, 129:2562–2578, June 2005b.

J. R. Bond, S. Cole, G. Efstathiou, and N. Kaiser. ApJ, 379:440–460, October 1991.

R. J. Bouwens, G. D. Illingworth, M. Franx, and H. Ford. ApJ, 670:928–958, December 2007.

R. G. Bower. MNRAS, 248:332–352, January 1991.

R. G. Bower, A. J. Benson, R. Malbon, J. C. Helly, C. S. Frenk, C. M. Baugh, S. Cole, and C. G. Lacey. MNRAS, 370:645–655, August 2006.

G. Bruzual A. and S. Charlot. ApJ, 405:538–553, March 1993.

Y.-C. Cai, R. E. Angulo, C. M. Baugh, S. Cole, C. S. Frenk, and A. Jenkins. MNRAS, 395:1185–1203, May 2009.

A. Cattaneo, A. Dekel, J. Devriendt, B. Guiderdoni, and J. Blaizot. MNRAS, 370:1651–1665, August 2006.

S. Chandrasekhar. ApJ, 97:255–+, March 1943.

S. C. Chapman, I. Smail, R. Windhorst, T. Muxlow, and R. J. Ivison. ApJ, 611:732–738, August 2004.

S. C. Chapman, A. W. Blain, I. Smail, and R. J. Ivison. ApJ, 622:772–796, April 2005.

S. Cole. ApJ, 367:45, January 1991.

S. Cole and C. Lacey. MNRAS, 281:716–+, July 1996.

S. Cole, A. Aragon-Salamanca, C. S. Frenk, J. F. Navarro, and S. E. Zepf. MNRAS, 271: 781–+, December 1994.

S. Cole, C. G. Lacey, C. M. Baugh, and C. S. Frenk. MNRAS, 319:168–204, November 2000.

M. Colless, B. A. Peterson, C. Jackson, J. A. Peacock, S. Cole, P. Norberg, I. K. Baldry, C. M. Baugh, J. Bland-Hawthorn, T. Bridges, R. Cannon, C. Collins, W. Couch, N. Cross, G. Dalton, R. De Propris, S. P. Driver, G. Efstathiou, R. S. Ellis, C. S. Frenk, K. Glazebrook, O. Lahav, I. Lewis, S. Lumsden, S. Maddox, D. Madgwick, W. Sutherland, and K. Taylor. *ArXiv Astrophysics e-prints*, June 2003.

R. A. Crain, T. Theuns, C. Dalla Vecchia, V. R. Eke, C. S. Frenk, A. Jenkins, S. T. Kay, J. A. Peacock, F. R. Pearce, J. Schaye, V. Springel, P. A. Thomas, S. D. M. White, and R. P. C. Wiersma. MNRAS, pages 1262–+, September 2009.

R. A. C. Croft, T. Di Matteo, V. Springel, and L. Hernquist. *ArXiv e-prints*, March 2008.

D. J. Croton, V. Springel, S. D. M. White, G. De Lucia, C. S. Frenk, L. Gao, A. Jenkins, G. Kauffmann, J. F. Navarro, and N. Yoshida. MNRAS, 367:864–864, April 2006.

M. Davis, G. Efstathiou, C. S. Frenk, and S. D. M. White. ApJ, 292:371, May 1985.

V. R. Eke, S. Cole, and C. S. Frenk. MNRAS, 282:263–280, September 1996.

V. R. Eke, J. F. Navarro, and C. S. Frenk. ApJ, 503:569–+, August 1998.

S. M. Faber and J. S. Gallagher. ARA&A, 17:135, 1979.

M. A. Fardal, N. Katz, D. H. Weinberg, and R. Davé. MNRAS, 379:985–1002, August 2007.

A. Ferrara, S. Bianchi, A. Cimatti, and C. Giovanardi. ApJS, 123:437–445, August 1999.

A. S. Font, R. G. Bower, I. G. McCarthy, A. J. Benson, C. S. Frenk, J. C. Helly, C. G. Lacey, C. M. Baugh, and S. Cole. MNRAS, 389:1619–1629, October 2008.

F. Fontanot, P. Monaco, L. Silva, and A. Grazian. MNRAS, 382:903–914, December 2007.

C. S. Frenk, A. E. Evrard, S. D. M. White, and F. J. Summers. ApJ, 472:460–+, December 1996.

C. S. Frenk, S. D. M. White, P. Bode, J. R. Bond, G. L. Bryan, R. Cen, H. M. P. Couchman, A. E. Evrard, N. Gnedin, A. Jenkins, A. M. Khokhlov, A. Klypin, J. F. Navarro, M. L. Norman, J. P. Ostriker, J. M. Owen, F. R. Pearce, U.-L. Pen, M. Steinmetz, P. A. Thomas, J. V. Villumsen, J. W. Wadsley, M. S. Warren, G. Xu, and G. Yepes. ApJ, 525:554–582, November 1999.

M. Giavalisco. ARA&A, 40:579–641, 2002.

R. A. Gingold and J. J. Monaghan. MNRAS, 181:375, November 1977.

F. Governato, C. M. Baugh, C. S. Frenk, S. Cole, C. G. Lacey, T. Quinn, and J. Stadel. Nature, 392:359–361, March 1998.

F. Governato, L. Mayer, J. Wadsley, J. P. Gardner, B. Willman, E. Hayashi, T. Quinn, J. Stadel, and G. Lake. ApJ, 607:688–696, June 2004.

F. Governato, B. Willman, L. Mayer, A. Brooks, G. Stinson, O. Valenzuela, J. Wadsley, and T. Quinn. MNRAS, 374:1479–1494, February 2007.

G. L. Granato, C. G. Lacey, L. Silva, A. Bressan, C. M. Baugh, S. Cole, and C. S. Frenk. ApJ, 542:710–730, October 2000.

A. H. Guth. Phys. Rev. D, 23:347, January 1981.

G. Harker, S. Cole, J. Helly, C. Frenk, and A. Jenkins. MNRAS, 367:1039–1049, April 2006.

T. M. Heckman, L. Armus, and G. K. Miley. ApJS, 74:833–868, December 1990.

J. C. Helly, S. Cole, C. S. Frenk, C. M. Baugh, A. Benson, and C. Lacey. MNRAS, 338: 903–912, February 2003.

G. Hinshaw, J. L. Weiland, R. S. Hill, N. Odegard, D. Larson, C. L. Bennett, J. Dunkley, B. Gold, M. R. Greason, N. Jarosik, E. Komatsu, M. R. Nolta, L. Page, D. N. Spergel, E. Wollack, M. Halpern, A. Kogut, M. Limon, S. S. Meyer, G. S. Tucker, and E. L. Wright. ApJS, 180:225–245, February 2009.

D. W. Hogg, M. R. Blanton, J. Brinchmann, D. J. Eisenstein, D. J. Schlegel, J. E. Gunn, T. A. McKay, H.-W. Rix, N. A. Bahcall, J. Brinkmann, and A. Meiksin. ApJ, 601: L29–L32, January 2004.

E. Hubble. *Proceedings of the National Academy of Science*, 15:168–173, March 1929.

D. H. Hughes, S. Serjeant, J. Dunlop, M. Rowan-Robinson, A. Blain, R. G. Mann, R. Ivison, J. Peacock, A. Efstathiou, W. Gear, S. Oliver, A. Lawrence, M. Longair, P. Goldschmidt, and T. Jenness. Nature, 394:241–247, July 1998.

N. Katz, L. Hernquist, and D. H. Weinberg. ApJ, 399:L109–L112, November 1992.

N. Katz, D. H. Weinberg, and L. Hernquist. ApJS, 105:19–+, July 1996.

G. Kauffmann. MNRAS, 281:475, July 1996.

G. Kauffmann and S. Charlot. MNRAS, 297:L23, June 1998.

G. Kauffmann and M. Haehnelt. MNRAS, 311:576, January 2000.

G. Kauffmann, S. D. M. White, and B. Guiderdoni. MNRAS, 264:201, September 1993.

G. Kauffmann, A. Nusser, and M. Steinmetz. MNRAS, 286:795, April 1997.

G. Kauffmann, J. M. Colberg, A. Diaferio, and S. D. M. White. MNRAS, 307:529, August 1999a.

G. Kauffmann, J. M. Colberg, A. Diaferio, and S. D. M. White. MNRAS, 303:188, February 1999b.

A. Kaviani, M. G. Haehnelt, and G. Kauffmann. MNRAS, 340:739–746, April 2003.

R. C. Kennicutt, Jr. ApJ, 272:54–67, September 1983.

E. Komatsu, J. Dunkley, M. R. Nolta, C. L. Bennett, B. Gold, G. Hinshaw, N. Jarosik, D. Larson, M. Limon, L. Page, D. N. Spergel, M. Halpern, R. S. Hill, A. Kogut, S. S. Meyer, G. S. Tucker, J. L. Weiland, E. Wollack, and E. L. Wright. ApJS, 180:330–376, February 2009.

C. Lacey and S. Cole. MNRAS, 262:627–649, June 1993.

C. Lacey and J. Silk. ApJ, 381:14, November 1991.

C. G. Lacey, C. M. Baugh, C. S. Frenk, L. Silva, G. L. Granato, and A. Bressan. MNRAS, 385:1155–1178, April 2008.

C. G. Lacey, et al., 2010, in preparation.

C. D. P. Lagos, S. A. Cora, and N. D. Padilla. MNRAS, 388:587–602, August 2008.

M. Le Delliou, C. Lacey, C. M. Baugh, B. Guiderdoni, R. Bacon, H. Courtois, T. Sousbie, and S. L. Morris. MNRAS, 357:L11–L15, February 2005.

M. Le Delliou, C. G. Lacey, C. M. Baugh, and S. L. Morris. MNRAS, 365:712–726, January 2006.

L. B. Lucy. AJ, 82:1013, December 1977.

R. K. Malbon, C. M. Baugh, C. S. Frenk, and C. G. Lacey. MNRAS, 382:1394–1414, December 2007.

C. Maraston. MNRAS, 362:799–825, September 2005.

C. Maraston, E. Daddi, A. Renzini, A. Cimatti, M. Dickinson, C. Papovich, A. Pasquali, and N. Pirzkal. ApJ, 652:85–96, November 2006.

J. C. Mather, E. S. Cheng, D. A. Cottingham, R. E. Eplee, D. J. Fixsen, T. Hewagama, R. B. Isaacman, K. A. Jensen, S. S. Meyer, P. D. Noerdlinger, S. M. Read, L. P. Rosen, R. A. Shafer, E. L. Wright, C. L. Bennett, N. W. Boggess, M. G. Hauser, T. Kelsall, S. H. Moseley, R. F. Silverberg, G. F. Smoot, R. Weiss, and D. T. Wilkinson. ApJ, 420:439, January 1994.

P. Monaco, F. Fontanot, and G. Taffoni. MNRAS, 375:1189–1219, March 2007.

K. Nagamine, R. Cen, L. Hernquist, J. P. Ostriker, and V. Springel. ApJ, 610:45–50, July 2004.

J. F. Navarro and M. Steinmetz. ApJ, 478:13–+, March 1997.

J. F. Navarro, C. S. Frenk, and S. D. M. White. MNRAS, 275:720–740, August 1995.

J. F. Navarro, C. S. Frenk, and S. D. M. White. ApJ, 490:493–+, December 1997.

P. Norberg, S. Cole, C. M. Baugh, C. S. Frenk, I. Baldry, J. Bland-Hawthorn, T. Bridges, R. Cannon, M. Colless, C. Collins, W. Couch, N. J. G. Cross, G. Dalton, R. De Propris, S. P. Driver, G. Efstathiou, R. S. Ellis, K. Glazebrook, C. Jackson, O. Lahav, I. Lewis, S. Lumsden, S. Maddox, D. Madgwick, J. A. Peacock, B. A. Peterson, W. Sutherland, and K. Taylor. MNRAS, 336:907–931, November 2002.

T. Okamoto, V. R. Eke, C. S. Frenk, and A. Jenkins. MNRAS, 363:1299–1314, November 2005.

A. Orsi, C. G. Lacey, C. M. Baugh, and L. Infante. MNRAS, 391:1589–1604, December 2008.

H. Parkinson, S. Cole, and J. Helly. MNRAS, 383:557–564, January 2008.

F. R. Pearce, A. Jenkins, C. S. Frenk, J. M. Colberg, S. D. M. White, P. A. Thomas, H. M. P. Couchman, J. A. Peacock, G. Efstathiou, and The Virgo Consortium. ApJ, 521:L99–L102, August 1999.

W. J. Percival, W. Sutherland, J. A. Peacock, C. M. Baugh, J. Bland-Hawthorn, T. Bridges, R. Cannon, S. Cole, M. Colless, C. Collins, W. Couch, G. Dalton, R. De Propris, S. P. Driver, G. Efstathiou, R. S. Ellis, C. S. Frenk, K. Glazebrook, C. Jackson, O. Lahav, I. Lewis, S. Lumsden, S. Maddox, S. Moody, P. Norberg, B. A. Peterson, and K. Taylor. MNRAS, 337:1068–1080, December 2002.

J. R. Peterson, S. M. Kahn, F. B. S. Paerels, J. S. Kaastra, T. Tamura, J. A. M. Bleeker, C. Ferrigno, and J. G. Jernigan. ApJ, 590:207–224, June 2003.

M. Pettini, A. E. Shapley, C. C. Steidel, J.-G. Cuby, M. Dickinson, A. F. M. Moorwood, K. L. Adelberger, and M. Giavalisco. ApJ, 554:981–1000, June 2001.

W. H. Press and P. Schechter. ApJ, 187:425–438, February 1974.

J.-L. Puget, A. Abergel, J.-P. Bernard, F. Boulanger, W. B. Burton, F.-X. Desert, and D. Hartmann. A&A, 308:L5+, April 1996.

M. J. Rees and J. P. Ostriker. MNRAS, 179:541, June 1977.

G. B. Rybicki and A. P. Lightman. *Radiative processes in astrophysics.* 1979.

A. G. Sánchez, C. M. Baugh, W. J. Percival, J. A. Peacock, N. D. Padilla, S. Cole, C. S. Frenk, and P. Norberg. MNRAS, 366:189–207, February 2006.

A. G. Sánchez, M. Crocce, A. Cabre, C. M. Baugh, and E. Gaztanaga. *ArXiv e-prints*, January 2009.

C. Scannapieco, P. B. Tissera, S. D. M. White, and V. Springel. MNRAS, 371:1125–1139, September 2006.

J. Schaye, C. Dalla Vecchia, C. M. Booth, R. P. C. Wiersma, T. Theuns, M. R. Haas, S. Bertone, A. R. Duffy, I. G. McCarthy, and F. van de Voort. *ArXiv e-prints*, September 2009.

S. Shen, H. J. Mo, S. D. M. White, M. R. Blanton, G. Kauffmann, W. Voges, J. Brinkmann, and I. Csabai. MNRAS, 343:978–994, August 2003.

J. Silk. ApJ, 211:638, February 1977.

L. Silva, G. L. Granato, A. Bressan, and L. Danese. ApJ, 509:103–117, December 1998.

I. Smail, R. J. Ivison, and A. W. Blain. ApJ, 490:L5+, November 1997.

S. Smith. ApJ, 83:23, January 1936.

R. S. Somerville and J. R. Primack. MNRAS, 310:1087, December 1999.

R. S. Somerville, J. R. Primack, and S. M. Faber. MNRAS, 320:504–528, February 2001.

V. Springel, S. D. M. White, A. Jenkins, C. S. Frenk, N. Yoshida, L. Gao, J. Navarro, R. Thacker, D. Croton, J. Helly, J. A. Peacock, S. Cole, P. Thomas, H. Couchman, A. Evrard, J. Colberg, and F. Pearce. Nature, 435:629–636, June 2005.

V. Springel, C. S. Frenk, and S. D. M. White. Nature, 440:1137–1144, April 2006.

V. Springel, J. Wang, M. Vogelsberger, A. Ludlow, A. Jenkins, A. Helmi, J. F. Navarro, C. S. Frenk, and S. D. M. White. MNRAS, 391:1685–1711, December 2008.

C. C. Steidel and D. Hamilton. AJ, 104:941–949, September 1992.

C. C. Steidel, M. Giavalisco, M. Pettini, M. Dickinson, and K. L. Adelberger. ApJ, 462: L17+, May 1996.

C. C. Steidel, K. L. Adelberger, M. Giavalisco, M. Dickinson, and M. Pettini. ApJ, 519: 1–17, July 1999a.

C. C. Steidel, K. L. Adelberger, M. Giavalisco, M. Dickinson, and M. Pettini. ApJ, 519: 1–17, July 1999b.

C. C. Steidel, K. L. Adelberger, A. E. Shapley, M. Pettini, M. Dickinson, and M. Giavalisco. ApJ, 592:728–754, August 2003.

I. Strateva, Ž. Ivezić, G. R. Knapp, V. K. Narayanan, M. A. Strauss, J. E. Gunn, R. H. Lupton, D. Schlegel, N. A. Bahcall, J. Brinkmann, R. J. Brunner, T. Budavári, I. Csabai, F. J. Castander, M. Doi, M. Fukugita, Z. Győry, M. Hamabe, G. Hennessy, T. Ichikawa, P. Z. Kunszt, D. Q. Lamb, T. A. McKay, S. Okamura, J. Racusin, M. Sekiguchi, D. P. Schneider, K. Shimasaku, and D. York. AJ, 122:1861–1874, October 2001.

A. M. Swinbank, C. G. Lacey, I. Smail, C. M. Baugh, C. S. Frenk, A. W. Blain, S. C. Chapman, K. E. K. Coppin, R. J. Ivison, J. E. Gonzalez, and L. J. Hainline. MNRAS, 391:420–434, November 2008.

C. Tonini, C. Maraston, D. Thomas, J. Devriendt, and J. Silk. *ArXiv e-prints*, September 2009.

G. Tormen. MNRAS, 290:411, September 1997.

P. G. van Dokkum. ApJ, 674:29–50, February 2008.

S. D. M. White and C. S. Frenk. ApJ, 379:52, September 1991.

S. D. M. White and M. J. Rees. MNRAS, 183:341, May 1978.

R. J. Wilman, J. Gerssen, R. G. Bower, S. L. Morris, R. Bacon, P. T. de Zeeuw, and R. L. Davies. Nature, 436:227–229, July 2005.

F. Zwicky. *Helvetica Phys. Acta*, 6:110, 1933.